CHALMERS
UNIVERSITY OF TECHNOLOGY

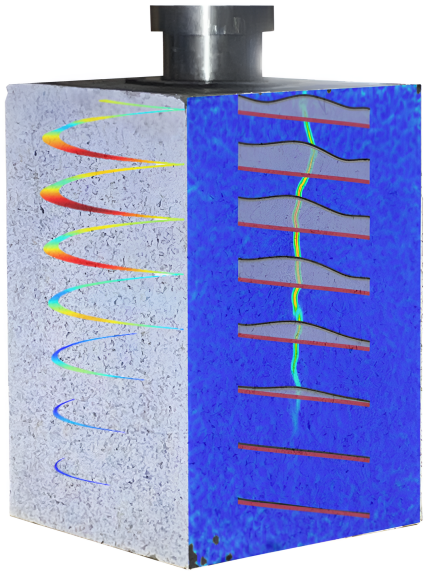

Fibre-reinforced post-tensioned anchorage zone

An experimental comparison of reinforcement configurations

Master's thesis in Master Program Structural Engineering and Building Technology

Ludwig Bengtsson, Anton Nordek

DEPARTMENT OF ARCHITECTURE AND CIVIL ENGINEERING

CHALMERS UNIVERSITY OF TECHNOLOGY
Gothenburg, Sweden 2024
www.chalmers.se

Master's thesis 2024

Fibre-reinforced post-tensioned anchorage zone

An experimental comparison of reinforcement configurations

LUDWIG BENGTSSON
ANTON NORDEK

CHALMERS
UNIVERSITY OF TECHNOLOGY

Department of Architecture and Civil Engineering
Division of Structural Engineering
Concrete structures
Chalmers University of Technology
Gothenburg, Sweden 2024

Fibre-reinforced post-tensioned anchorage zone
An experimental comparison of reinforcement configurations
LUDWIG BENGTSSON
ANTON NORDEK

Supervisor and examiner: Senior Lecturer Carlos Gil Berrocal, Department of Architecture and Civil Engineering
Supervisor: Associate Professor Ignasi Fernandez, Department of Architecture and Civil Engineering
Supervisor: Associate Professor Rasmus Rempling, Department of Architecture and Civil Engineering
Supervisor: Bridge Department Manager Daniel Ekström, WSP Sverige AB

Master's Thesis 2024
Department of Architecture and Civil Engineering
Division of Structural Engineering
Concrete structures
Chalmers University of Technology
SE-412 96 Gothenburg
Telephone +46 31 772 1000

Cover: Strain distributions of Specimen 5 obtained via Digital Image Correlation and Distributed Optic Fiber Sensing during load testing.

Gothenburg, Sweden 2024

Fibre-reinforced post-tension anchoring zone
An experimental comparison of reinforcement configurations
Ludwig Bengtsson
Anton Nordek
Department of Architecture and Civil Engineering
Chalmers University of Technology

Abstract

Prestressed concrete enables the design and construction of long-span, slender, and economical concrete structures. In post-tensioned concrete structures, the anchorage zones are critical details, which normally end up both heavily reinforced and labour-intensive while following the manufacturer's European Technical Assessment (ETA) approval for additional reinforcement and applicable design procedures. The upcoming Eurocode will permit the design of these regions using steel fibre reinforced concrete (SFRC). This master's thesis presents an experimental comparison of three different post-tensioned anchorage zones: a conventionally designed anchorage zone made of reinforced concrete and ETA-approved helical bursting, an SFRC anchorage zone equipped with ETA-approved helical bursting reinforcement, and an SFRC anchorage zone.

The anchorage zones are designed according to the applicable Eurocode, upcoming Eurocode and course literature. The final design of the specimens, representing anchorage zones, was validated by a non-linear finite element analysis in the softward Diana 10.8 to ensure the desirable structural response. Two specimens of each anchorage design were constructed and equipped with 3D-printed plastic spirals to support the distributed optical fiber sensors (DOFS). The specimens were tested experimentally by subjecting them to centric compressive loading. The configurations were evaluated and compared by analysing the data obtained from the DOFS, Digital Image Correlation (DIC), and load-deformation response.

The comparison between DOFS measurements and DIC has shown that the proposed fiber optics arrangement enabled the assessment of the specimens' structural response with high accuracy. According to the results, the plain SFRC configuration exhibits the largest strains and crack widths of the three configurations. Incorporating helical bursting reinforcement in SFRC significantly improved the structural response by decreasing the measured strains and crack widths. The reference configurations exhibited the lowest strains and smallest crack width while maintaining the highest consistency in the structural response.

The findings in this master's thesis will likely provide further knowledge and enhance the contemporary design for post-tensioned anchorage zones.

Keywords: Post-tensioned concrete, Anchorage zone, Steel fibre reinforced concrete, Distributed optical fiber sensing, Digital Image Correlation, DIC, Crack monitoring

Acknowledgements

This master's thesis was conducted from January to June 2024 at the Department of Architecture and Civil Engineering, Chalmers University of Technology. It accounts for 30 credits and serves as the final project for the master's program in Structural Engineering and Building Technology. The thesis was done as a cooperation between Chalmers, WSP and NCC.

We would like to express our gratitude to our examiner, Carlos Gil Berrocal, and our supervisors, Ignasi Fernandez, Rasmus Rempling, and Daniel Ekström. Their experience in the field of research has provided us with invaluable guidance throughout the project.

The main part of the experimental work was conducted in the laboratories at Chalmers and RISE. We would like to thank Sebastian Almfeldt and Anders Karlsson at the Structures Lab for their support and many hours of assistance during the construction phase of our thesis. Additionally, we would like to thank Mathias Flansbjer and Christian Davidsson at RISE for their assistance during testing.

Finally, we would like to thank the Bridge Department at WSP in Gothenburg for their encouragement and for providing office space during our master's thesis. We would also like to thank our opponent group, Hugo von Kraemer and Theodor Sjölund, for valuable input.

Ludwig Bengtsson, Gothenburg, June 2024
Anton Nordek, Gothenburg, June 2024

List of Acronyms

CMOD	Crack Mouth Opening Displacement
DIC	Digital Image Correlation
DOFS	Distributed Fiber Optical Sensing
ETA	European Technical Assessment
FEA	Finite element analysis
NLFEA	Non-linear finite element analysis
OFDR	Optical Frequency Domain Reflectometry
SHM	Structural Health Monitoring
REV	Revolution
SFRC	Steel fibre reinforced concrete
WSTM	Wedge Splitting Test Method

Nomenclature

Greek lower case symbols

α	Angle
α	Reduction factor
ϵ	Strain
ϵ_c	Concrete strain
ϵ_{ctm}	Average concrete tensile strain
ϵ_{Ft}	Fibre tensile strain
ϵ_{Ftu}	Ultimate fibre tensile strain
ϵ_{uf}	Strain at ultimate fibre strength
λ	Aspect ratio of fibre (length / diameter)
κ_O	Orientation factor
σ	Stress
σ_j	Principal stress
σ_m	Mean stress
σ_{Ed}	Design stress
σ_{Rd}	Resistance stress
σ_c	Compressive stress in the concrete
τ_b	Local bond stress
$\tau_{bu.split.1}$	Peak local bond resistance
τ_{bmax}	Maximum value of bond stress
υ	Poisson's ratio
υ	Effectiveness factor
ϕ	Diameter

Roman lower case letters

a	Distance of force transfer unit
c	Distance concrete prism
d	Diameter
f_c	Compressive concrete strength
f_{ck}	Characteristic compressive cylinder strength of concrete at 28 days
f_{cm}	Mean concrete cylinder compressive strength
f_{ct}	Concrete tensile strength

f_{ctm}	Aveagre concrete tensile strength
$f_{Ft1.ef}$	Design residual tensile strength of fibre reinforced concrete at CMOD 0.5 mm
$f_{Ft3.ef}$	Design residual tensile strength of fibre reinforced concrete at CMOD 2.5 mm
f_{uf}	Ultimate fibre tensile strength
f_{yk}	Characteristic yield strength of reinforcement
f_{R1}	Residual flexural tensile strength of fibre reinforced concrete at CMOD 0.5 mm
f_{R3}	Residual flexural tensile strength of fibre reinforced concrete at CMOD 2.5 mm
l	Length
l_{cs}	Structural length
s	Slip
s_{rm}	Average crack distance
w	Crack opening
w_u	Ultimate crack crack opening

Roman upper case letters

A_s	Cross-sectional area of reinforcement
$A_{s.surf}$	Cross-sectional area of surface reinforcement
C	Strut force
E_c	Modulus of elasticity for concrete
E_f	Modulus of elasticity
F_v	Vertical force
F_{sp}	Splitting force
G_F	Fracture energy
P	Prestressing force
$S_{r,max,cal}$	Maximum crack spacing
T	Tie force
V_f	Volume fraction of fibres

Contents

List of Acronyms ix

Nomenclature xi

List of Figures xvii

List of Tables xxiii

1 Introduction 1
- 1.1 Background . . . 1
- 1.2 Purpose and objectives . . . 1
- 1.3 Scope and Limitations . . . 2
  - 1.3.1 Scope . . . 2
  - 1.3.2 Limitations . . . 2
  - 1.3.3 Method . . . 2

2 Theory 5
- 2.1 Prestressing . . . 5
- 2.2 Dimensioning of anchorage zone in reinforced concrete . . . 6
  - 2.2.1 Strut and tie method . . . 9
- 2.3 Concrete material model . . . 11
  - 2.3.1 Non-linear behaviour of concrete . . . 11
  - 2.3.2 Uniaxial tension . . . 12
  - 2.3.3 Uniaxial compression . . . 13
  - 2.3.4 Multiaxial concrete behaviour . . . 15
- 2.4 Steel fibre reinforced concrete . . . 16
  - 2.4.1 Steel fibres . . . 17
  - 2.4.2 Compressive behaviour . . . 17
  - 2.4.3 Tensile behaviour . . . 18
- 2.5 Concrete and reinforcement interaction . . . 19
- 2.6 Non-linear finite element analysis . . . 21
  - 2.6.1 Smeared crack approach . . . 21
  - 2.6.2 Discrete crack approach . . . 21
  - 2.6.3 Weakened element technique . . . 22
  - 2.6.4 Reinforcement interaction . . . 22
- 2.7 Optical fiber sensors . . . 23
  - 2.7.1 Application of DOFS . . . 23

2.8 Digital image correlation 24

3 Design and construction of specimens 27
3.1 Design conditions 27
3.1.1 Material 27
3.1.2 Anchorage system 28
3.1.3 Geometry 28
3.2 Design of transversal reinforcement 28
3.2.1 Strut and tie model 28
3.2.2 Structural verifications 29
3.2.3 Local bond-slip relationship 30
3.3 Design steel fibre reinforced concrete 30
3.4 Numerical simulation 34
3.4.1 General modelling choices 34
3.4.2 Material 35
3.4.3 Crack modelling approach 35
3.4.4 Mesh 36
3.4.5 Analysis 36
3.4.6 Preliminary results and design of specimens 37
3.5 Design of fibre optics arrangement 38
3.5.1 Fibre optic type 38
3.5.2 Design of fiber optics support 39
3.5.3 Attachement of the fiber optics 40
3.5.4 Localisation of the fiber optics 41
3.6 Construction 41
3.6.1 Formwork and mounting of anchorage system 41
3.6.2 Assembly of 3D spirals and mounting of fiber optics 42
3.6.3 Final design 44
3.6.4 Casting of specimens 45
3.6.5 DIC surface preparations 46

4 Experimental testing 47
4.1 Material testing 47
4.1.1 Compressive strength 47
4.1.2 Fracture properties 48
4.2 Concentric load testing 52

5 Results and observations 55
5.1 Load displacement curves 56
5.2 Postprocessing of DOFS measurements for visualisation of strain distribution 58
5.3 DOFS measurements for evaluation of strain development and localisation 59
5.4 Comparison between DOFS measurements and DIC strain field . . . 66
5.5 Crack width evaluation based on DOFS measurements and DIC . . . 71

6 Discussion 77

6.1 Evaluation of assessment method 77
6.2 Evaluation of the different configurations of anchorage zones 78

7 Conclusion **81**
7.1 Further outlook 81

Bibliography **83**

A Strain distribution arranged 3D **I**

B Strain distribution in outer spiral **III**

C Strain distribution in inner spiral **V**

D Strain distribution in outer spiral divided by side **VII**

E Strain distribution in inner spiral divided by side **IX**

F DIC images **XIII**

G Surface strain fields measured with DIC compared with DOFS measured strains **XVII**

H Crack widths **XIX**

I Product sheet XM20 **XXI**

J Dimensioning of reinforced concrete specimen **XXV**

List of Figures

2.1 Visualisation of tensile stresses in an anchorage zone, adapted from (Engström, 2011). 6
2.2 Stress distribution for a centric loaded anchorage zone, adapted from (Breen et al., 1994). 7
2.3 Anchorage zone divided into critical zones, adapted from (Pham et al., 2021). 7
2.4 Anchorage system equipped with embedded ribs and local reinforcement, retrieved from (CCL, 2017). 8
2.5 Compression nodes underneath the anchorage plate, retrieved from (Engström, 2015). 10
2.6 Different stages of the fracture process of uniaxial tensile stress, retrieved from (Plos, 2000). 12
2.7 The stress-displacement relationship in a uniaxial tensile test of concrete (left), and how it is converted into an elastic-strain relation (middle) and a stress-crack opening relation (right). Adapted from (Plos et al., 2021). 13
2.8 The behaviour of a concrete cylinder in uniaxial compression, adapted from (Kotsovos, 2015). 14
2.9 The characteristics of a stress-strain relation for Concrete in a compressive cylinder test, adapted from (Samani & Attard, 2012). 14
2.10 The strength surfaces formed by the compressive (blue) and the tensile meridian (green). Only one of the three tensile meridians is illustrated. Adapted from (Häussler-Combe, 2022). 15
2.11 The biaxial strength of concrete, adapted from (Häussler-Combe, 2022). 16
2.12 The typical stress-strain relationship for normal and high strength concrete and how the fibre dosage affects the post-peak behaviour. Retrieved from (Löfgren, 2005). 18
2.13 Typical stress-strain relationship for plain concrete and SFRC with different aspect ratios under compressive loading, adapted from (Singh, 2017). 18
2.14 The tensile post-peak beaviour of plain concrete and SFRC, retrieved from (Löfgren, 2005). 19
2.15 Relation between slip and bond stresses for pull-out failure and splitting failure for confined and unconfined concrete, respectively, retrieved from (International Federation for Structural Concrete, 2013). 20

2.16 Representation of stresses and tractions on a reinforcement bar subjected to tension, retrieved from (Plos, 2000). 22
2.17 Process of DOFS using Rayleigh scattering based on OFDR, retrieved from Berrocal et al. (2021). 24
2.18 Example of a computer-rendered stochastic surface pattern. 25

3.1 Steel fibre Dramix 4D 65/35 BG, retrieved from (Bekaert, 2023). . . . 27
3.2 Adopted strut and tie model for the reinforced concrete specimens. . 29
3.3 Bond-slip relation describing the interaction of concrete and reinforcement for splitting failure. 30
3.4 Constitutive law for structural analysis of SFRC, adapted from (Kanstad, 2021). 32
3.5 Stress-strain relationship for SFRC obtained using Equations 3.3-3.9. 33
3.6 The three-dimensional model of the configurations consisting of solid elements. 34
3.7 Non-linear material models used in FEA, retrieved from (Ferreira, 2024). 35
3.8 Top view and side view of three different configurations (Reference, SFRC + Helix and SFRC) along with their corresponding structural components. 37
3.9 Load-displacement curve obtained from the FEA. 38
3.10 Dimensions of the plastic quarters in the outer and inner spiral. . . . 40
3.11 Mould side where the anchor system and metallic rods were mounted. 41
3.12 The assembly procedure of the 3D-printed spirals. 42
3.13 Attachment of fibre optics on the anchorage reinforcement and 3D-printed spirals. 43
3.14 Winding of the thread for the fire pinching. 43
3.15 Comparison between model rendering and final design for reference specimen. 44
3.16 Comparison between model rendering and final design for SFRC + Helix specimen. 44
3.17 Comparison between model rendering and final design for SFRC specimen. 45
3.18 Grouting of the uneven bottom surfaces. 45
3.19 Comparison between final stochastic pattern and desired stochastic pattern for DIC monitoring of the surface of the specimens. 46

4.1 Cube test setup. 47
4.2 Wedge split test setup. 48
4.3 Splitting force-CMOD curve for concrete specimens. 49
4.4 Splitting force-CMOD curve for SFRC specimens. 50
4.5 Stress-strain relationship for SFRC obtained from WST. 51
4.6 Concentric load setup and positioning of specimen. 52
4.7 The strain data obtained from the optical fiber from the outer spiral in Specimen 6 at a load of 950 kN. The plot shows the raw data obtained and how it was refined for the analysis. 53

5.1 Arrangement of distributed fiber optics. 55
5.2 Load-displacement curve obtained from the concentric load testing. . 56
5.3 The load-displacement curves obtained from NLFEA and the concentric load testing. 57
5.4 Strain distribution at 950 kN obtained by DOFS located at the inner and outer spiral of Specimen 1 (Reference). 58
5.5 Strain distribution at 950 kN obtained by DOFS located at the inner and outer spiral of Specimen 4 (SFRC + Helix). 59
5.6 Strain distribution at 950 kN obtained by DOFS located at the inner and outer spiral of Specimen 5 (SFRC). 59
5.7 Strain profiles for different load steps obtained by DOFS located at the outer spiral of Specimen 1 (Reference). 60
5.8 Strain profiles for different load steps obtained by DOFS located at the inner spiral of Specimen 1 (Reference). 61
5.9 Strain profiles for different load steps obtained by DOFS located at the outer spiral of Specimen 4 (SFRC + Helix). 62
5.10 Strain profiles for different load steps obtained by DOFS located at the inner spiral of Specimen 4 (SFRC + Helix). 63
5.11 Strain profiles for different load steps obtained by DOFS located at the outer spiral of Specimen 5 (SFRC). 64
5.12 Strain profiles for different load steps obtained by DOFS located at the inner spiral of Specimen 5 (SFRC). 65
5.13 Strain profiles for different load steps obtained by DOFS located at the outer spiral of Specimen 1 (Reference). The bottom plots display the projected strain profiles on each face of the specimen. 67
5.14 Surface strain fields measured with DIC compared with DOFS measured strains at 950 kN for Specimen 1 (Reference). 67
5.15 Strain profiles for different load steps obtained by DOFS located at the outer spiral of Specimen 4 (SFRC + Helix). The bottom plots display the projected strain profiles on each face of the specimen. . . 68
5.16 Surface strain fields measured with DIC compared with DOFS measured strains at 950 kN for Specimen 4 (SFRC + Helix). 68
5.17 Strain profiles for different load steps obtained by DOFS located at the outer spiral of Specimen 5 (SFRC). The bottom plots display the projected strain profiles on each face of the specimen. 69
5.18 Surface strain fields measured with DIC compared with DOFS measured strains at 950 kN for Specimen 5 (SFRC). 70
5.19 Methodology for determining crack widths using DOFS measurements. 71
5.20 Comparison of measured crack widths from DIC and calculated crack widths based on DOFS measurements calculated using Equations 5.1 and 5.2 during loading for Specimen 1 (Reference). 73
5.21 Comparison of measured crack widths from DIC and calculated crack widths based on DOFS measurements calculated using Equations 5.1 and 5.2 during loading for Specimen 4 (SFRC + Helix). 74

5.22 Comparison of measured crack widths from DIC and calculated crack widths based on DOFS measurements calculated using Equations 5.1 and 5.2 during loading for Specimen 5 (SFRC). 75

A.1 Strain distribution at 950 kN obtained by DOFS located at the inner and outer spiral of Specimen 2 (Reference). I
A.2 Strain distribution at 950 kN obtained by DOFS located at the inner and outer spiral of Specimen 3 (SFRC + Helix). I
A.3 Strain distribution at 950 kN obtained by DOFS located at the inner and outer spiral of Specimen 6 (SFRC). II

B.1 Strain profiles for different load steps obtained by DOFS located at the outer spiral of Specimen 2 (Reference). III
B.2 Strain profiles for different load steps obtained by DOFS located at the outer spiral of Specimen 3 (SFRC + Helix). IV
B.3 Strain profiles for different load steps obtained by DOFS located at the outer spiral of Specimen 6 (SFRC). IV

C.1 Strain profiles for different load steps obtained by DOFS located at the inner spiral of Specimen 2 (Reference). V
C.2 Strain profiles for different load steps obtained by DOFS located at the inner spiral of Specimen 3 (SFRC + Helix). VI
C.3 Strain profiles for different load steps obtained by DOFS located at the inner spiral of Specimen 6 (SFRC). VI

D.1 Strain profiles for different load steps obtained by DOFS located at the outer spiral of Specimen 2 (Reference). The bottom plots display the projected strain profiles on each side of the specimen. VII
D.2 Strain profiles for different load steps obtained by DOFS located at the outer spiral of Specimen 3 (SFRC + Helix). The bottom plots display the projected strain profiles on each side of the specimen. . . VIII
D.3 Strain profiles for different load steps obtained by DOFS located at the outer spiral of Specimen 6 (SFRC). The bottom plots display the projected strain profiles on each side of the specimen. VIII

E.1 Strain profiles for different load steps obtained by DOFS located at the inner spiral of Specimen 1 (Reference). The bottom plots display the projected strain profiles on each side of the specimen. IX
E.2 Strain profiles for different load steps obtained by DOFS located at the inner spiral of Specimen 2 (Reference). The bottom plots display the projected strain profiles on each side of the specimen. X
E.3 Strain profiles for different load steps obtained by DOFS located at the inner spiral of Specimen 3 (SFRC + Helix). The bottom plots display the projected strain profiles on each side of the specimen. . . X
E.4 Strain profiles for different load steps obtained by DOFS located at the inner spiral of Specimen 4 (SFRC + Helix). The bottom plots display the projected strain profiles on each side of the specimen. . . XI

E.5 Strain profiles for different load steps obtained by DOFS located at the inner spiral of Specimen 5 (SFRC). The bottom plots display the projected strain profiles on each side of the specimen. XI
E.6 Strain profiles for different load steps obtained by DOFS located at the inner spiral of Specimen 6 (SFRC). The bottom plots display the projected strain profiles on each side of the specimen. XII

F.1 Surface strain fields measured with DIC at 950 kN for Specimen 1 (Reference). XIII
F.2 Surface strain fields measured with DIC at 950 kN for Specimen 2 (Reference). XIII
F.3 Surface strain fields measured with DIC at 950 kN for Specimen 3 (SFRC + Helix). XIV
F.4 Surface strain fields measured with DIC at 950 kN for Specimen 4 (SFRC + Helix). XIV
F.5 Surface strain fields measured with DIC at 950 kN for Specimen 5 (SFRC). XIV
F.6 Surface strain fields measured with DIC at 950 kN for Specimen 6 (SFRC). XV

G.1 Surface strain fields measured with DIC compared with DOFS measured strains at 950 kN for Specimen 2 (Reference). XVII
G.2 Surface strain fields measured with DIC compared with DOFS measured strains at 950 kN for Specimen 3 (SFRC + Helix). XVIII
G.3 Surface strain fields measured with DIC compared with DOFS measured strains at 950 kN for Specimen 6 (SFRC). XVIII

H.1 Comparison of measured crack widths from DIC and calculated crack widths based on DOFS measurements calculated using Equations 5.1 and 5.2 during loading for Specimen 2 (Reference). XIX
H.2 Comparison of measured crack widths from DIC and calculated crack widths based on DOFS measurements calculated using Equations 5.1 and 5.2 during loading for Specimen 3 (SFRC + Helix). XX
H.3 Comparison of measured crack widths from DIC and calculated crack widths based on DOFS measurements calculated using Equations 5.1 and 5.2 during loading for Specimen 6 (SFRC). XX

List of Tables

3.1 Material properties of Dramix 4D 65/35 BG, retrieved from Bekaert, 2023. 31
3.2 Estimated residual strength of the SFRC. 31
3.3 The calculated steel quantity used in the configurations. 37

4.1 Results from cube test for concrete specimens. 48
4.2 Results from cube test for SFRC specimens. 48
4.3 Results from WST for concrete specimens. 50
4.4 Results from WST for SFRC specimens. 50

5.1 The numbering of the specimens and the corresponding configuration. 55
5.2 The Mean Absolute Error for the upper and lower bound calculated crack width to the measured crack widths, calculated according to Equation 5.3. 72
5.3 The loads when the strain exceeds the cracking strain at the inner spiral and outer spiral for the different specimens. 73

1

Introduction

1.1 Background

Prestressed concrete enables the design and construction of long-span, slender and economical concrete structures. Concrete can be prestressed by either pretensioning or post-tensioning methods. In post-tensioned concrete structures, the anchorage zones are critical details, which normally end up both heavily reinforced and labour-intensive while following the manufacturer's European Technical Assessment (ETA) approval for additional reinforcement and normal design procedures for global and local crushing and splitting failures. In the currently applicable version of Eurocode (European Committee for Standardization, 2004), it is only allowed to use regular reinforcement in anchorage zones. However, the upcoming Eurocode will permit the use of steel fibre reinforced concrete (SFRC) in anchorage zones. The incorporation of SFRC is believed to reduce the amount of regular reinforcement required in the anchorage zones, leading to savings in labour hours and improved working conditions during construction.

1.2 Purpose and objectives

The purpose of the thesis is to experimentally compare and evalutate the structural response of a post-tensioned anchorage zone of three different reinforcement configurations:

1. a design following the manufacturer's ETA approval, including additional reinforcement, referred to as the Reference configuration.
2. a design following the manufacturer's ETA approval, excluding additional reinforcement but with fibre reinforcement, referred to as the SFRC + Helix configuration.
3. a design with only fibre reinforcement, referred to as the SFRC configuration.

The following objectives define the purpose:

- Investigate the design procedure for a fibre-reinforced anchorage zone.
- Develop a solution for Distributed Fiber Optical Sensing (DOFS) monitoring to evaluate the structural response of an anchorage zone.
- Analyse and compare the experimental results of the test with different configurations.

1.3 Scope and Limitations

1.3.1 Scope

The scope of the master's thesis is to perform a comparative experimental analysis of the structural response of anchorage zones constructed with concrete of strength class C30/37 and with the steel fibre of type Dramix 4D 65/35 BG with a fibre volume fraction of 0.5%. The experimental testing includes six specimens, two of each reinforcement configuration, with the same geometry.

1.3.2 Limitations

The master's thesis results were limited to six specimens. A square cross-section was chosen to facilitate the design and construction of the anchorage zones. The load cell of the testing machine was limited to 1 MN. As a result, the failure of the designed specimens could not be investigated.

1.3.3 Method

The procedure of the master's thesis was divided into four phases: Initial phase, Design phase, Construction phase and Testing phase. The following chart provides an outline of the presented phases along with their respective activities.

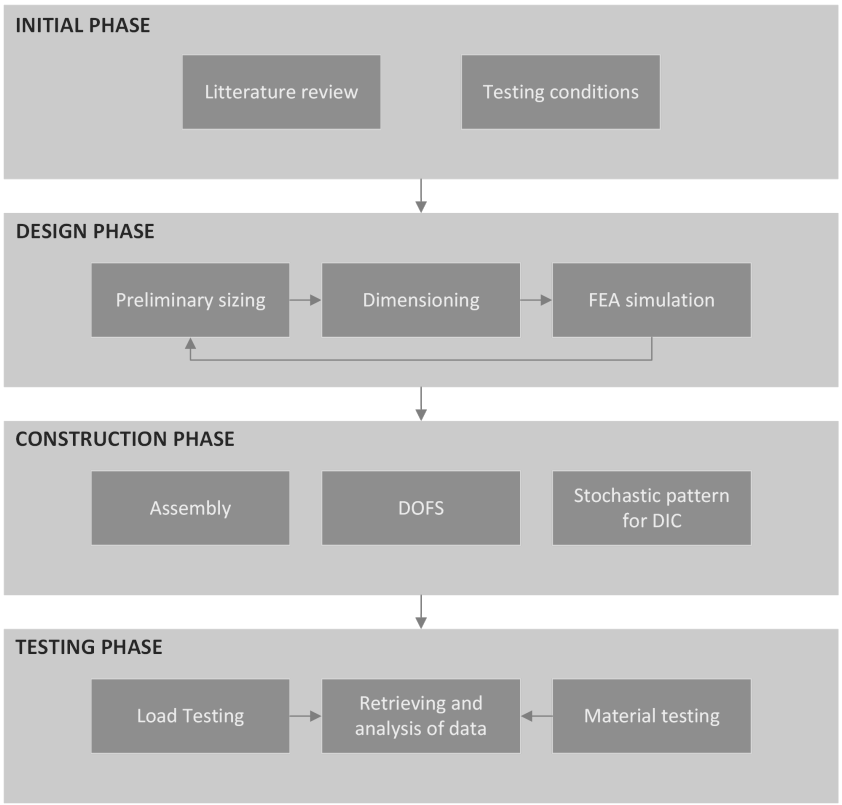

The master's thesis was initiated with a literature review regarding post-tensioning, anchorage zones, concrete and SFRC characteristics, and finite element modelling. The initial phase also included retrieving test limitations, which were used as boundary conditions for the design phase. The design was an iterative process, initiated with preliminary sizing, where the geometry of the specimens was determined. Based on the geometry and boundary conditions, the anchorage zones were dimensioned accordingly. As a final step, the designs were simulated in finite element analyses (FEA) in DIANA FEA to ensure the desirable structural response. The procedure was repeated until satisfactory results were obtained.

When the final design was determined, the construction phase was initiated. The construction phase involved assembly of formwork, mounting of reinforcement and anchorage system, installation of DOFS and casting of specimens. The installation of the DOFS included the design and assembly of the support structure, as well as mounting and calibration. After casting, a design technique was found to obtain the selected stochastic pattern for monitoring the specimens' surfaces using Digital Image Correlation (DIC).

The testing phase, which included load test of the specimens and material testing, was initiated 28 days after casting. The materials were characterised by performing cube tests and wedge splitting tests. The load testing was conducted with a hydraulic compression machine. During load testing, data retrieved from DOFS, DIC and load-deformation response were collected. The load was applied until the test machine's and load cell's maximum load capacity were reached. After testing, the test data was post-processed and analysed using MATLAB and GOM Correlate 2018.

2
Theory

2.1 Prestressing

Concrete is a material that is prone to cracking when subjected to tensile stresses. Tensile stresses can appear in a structural concrete member through various means, such as bending moments, pure tension forces, or highly concentrated compression forces in an anchorage zone of a post-tensioned member. According to Engström (2011), structural concrete members tend to crack under small loads already in the service state. Prestressing can be used to prevent cracks or limit the cracking process in a structural member. By introducing prestressing forces, a structural member undergoes compressive stresses to reduce the tensile stresses, which may arise due to additional loading. Hence, cracks could be totally prevented or limited in terms of crack widths. The prestressing is applied by tensioning of wires, and as a result, compression force is introduced into the member when released (Engström, 2011).

According to Engström (2011), prestressing of a structural member can be done in two different ways, either by post-tensioning or pre-tensioning. The two methods differ regarding how and when the wires are tensioned in the production process. In a post-tensioned structure, the pretension steel wires are tensioned after the concrete has been casted and hardened. In comparison, the wires are tensioned before the concrete casting in a pretensioned structure. The steel wires are put inside ducts in post-tensioned structures, which are grouted after the tension. The tensioned steel wires are anchored to load-transferring units restrained by the concrete. In pre-tensioning, the wires are detensioned after the concrete has hardened and is restrained by bonding interaction to the concrete (Engström, 2011).

2.2 Dimensioning of anchorage zone in reinforced concrete

In a post-tensioned structure, concentrated forces will be transferred into the concrete by anchoring of post-tensioned steel wires to load-transferring units. The zones where highly concentrated forces develop due to prestressing are referred to as discontinuity regions, in which ordinary beam theory does not apply (Engström, 2015). Instead, the stress fields propagating from concentrated forces are investigated, and specific dimensioning methods must be conducted.

Due to the high concentrated compression forces in an anchorage zone, transverse tensile forces develop to reach force equilibrium. As a consequence of the transversal tensile stresses, also referred to as bursting stresses, there is a risk that cracks are formed in these regions (Breen et al., 1994) (Engström, 2015). Transverse reinforcement must therefore be designed for traditional reinforced concrete structures to transfer tensile forces across the cracks (Engström, 2015). In addition, tensile stresses near the surface of the member will develop, which Breen et al. (1994) refer to as spalling stresses. Figure 2.1 presents a visualisation of tensile stresses in an anchorage zone subjected to centric loading.

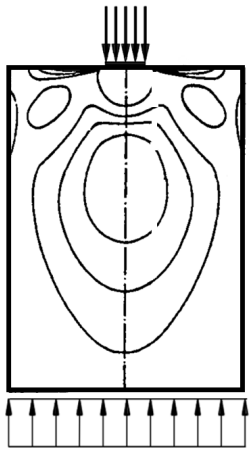

Figure 2.1: Visualisation of tensile stresses in an anchorage zone, adapted from (Engström, 2011).

Further away from the anchorage plate, the compressive stresses gradually distribute evenly while the transversal tensile stresses decrease (Breen et al., 1994). Stress trajectories and developed lateral stresses due to centric loading are visualised in Figure 2.2. Breen et al. (1994) states three critical regions within an anchorage zone, where the first one appears directly behind the anchorage plate, in which high bearing and compression forces are present. The second critical section appears in the anchorage zone some distance away from the point of force introduction, where transverse tensile stresses develop. The last critical section arises at the end surface parallel to the load-transferring plate, in which spalling stresses appear.

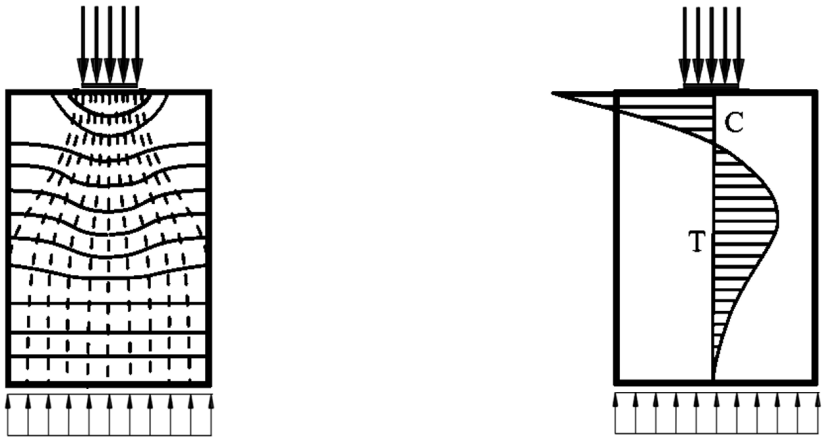

(a) Stresses trajectories **(b)** Lateral stresses

Figure 2.2: Stress distribution for a centric loaded anchorage zone, adapted from (Breen et al., 1994).

Studying Pham et al. (2021), it seems that the same critical zones described by Breen et al. (1994) appears for a square anchorage system equipped with a circular duct. The critical zones identified by Pham et al. (2021) are presented in Figure 2.3. In the critical zones, the concrete undergoes different damage procedures during the centric loading.

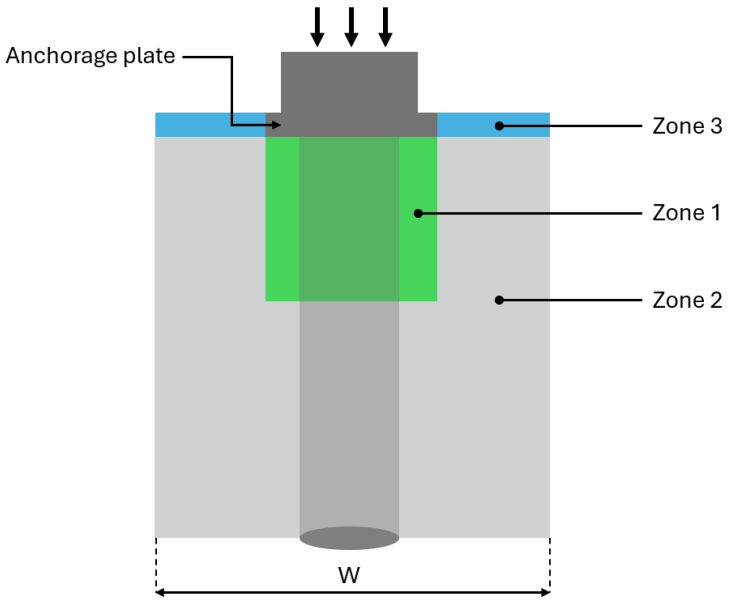

Figure 2.3: Anchorage zone divided into critical zones, adapted from (Pham et al., 2021).

According to the numerical analysis performed by Pham et al. (2021), tensile hoop stresses were developed in Zone 1 directly behind the anchorage plate and localised around the duct with decreasing magnitude towards the corners of the specimen. The maximum tensile hoop stresses were found at the top surface around the duct hole, and the second maximum was found at a distance of $0.28W$ from the top surface. This region is also aligned with the maximum tensile bursting stresses. According to the numerical analysis, the largest vertical compressive stresses were found directly behind the anchorage plate, gradually decreasing further into the specimen. Pham et al. (2021) states that the failure mode of this zone would be crushing of the concrete material. The compressive stresses reached a constant value at the distance $0.82H$ from the anchorage plate along the duct, where the tensile bursting stresses also became zero.

In Zone 3, Pham et al. (2021) also localised high tensile spalling stresses, similarly to Breen et al. (1994). The peak spalling stresses were found along the edge of the anchorage plate. The maximum bursting stresses were located at the interface of Zone 1 and 2, propagating horizontally towards the side surface of the specimen with decreasing magnitude. According to the experimental testing performed by Pham et al. (2021), the tensile bursting stresses caused internal cracks close to the duct that propagated towards the side surface of the specimen. The cracks were oriented vertically at the surface, perpendicular to the orientation of the bursting stress field.

To manage the concentrated compression forces that deviate directly behind the anchorage plate, (Breen et al., 1994) asserts that specialised anchorage devices are commonly used in anchorage zones. These devices facilitate increased strength in these areas by confinement of concrete by incorporating local reinforcement and embedded ribs distributed downwards in the concrete. This approach mitigates local stresses and distributes the concentrated force more effectively. An example of such an anchorage system, equipped with embedded ribs and local reinforcement, is presented in Figure 2.4.

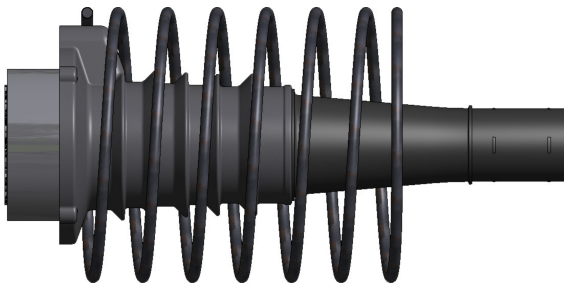

Figure 2.4: Anchorage system equipped with embedded ribs and local reinforcement, retrieved from (CCL, 2017).

2.2.1 Strut and tie method

The strut and tie method can be used to analyse stress fields in regions where ordinary beam theory does not apply, typically in zones with concentrated forces or geometrical discontinuities. The method can be applied for cracked reinforced concrete, mainly in the ultimate limit state and is governed by the theory of plasticity (Engström, 2015). Although Engström (2015) recommends that a strut and tie model should be adopted on a basis similar to a linear elastic stress field of a reinforced member due to the need for plastic redistribution and to achieve certain service state requirements. Too extreme assumptions for the chosen stress field may result in insufficient plastic redistribution. One way to develop a strut and tie model for a structural member is to analyse the stress field pattern, so called The load path method. The strut and tie model is conducted by inserting struts and ties representing the resultant of the compressive or tensile stress fields, respectively. If the strut and tie analysis is executed on the basis on equilibrium conditions with sufficient strength of the materials, a lower bound solution is found. Consequently, for every loading scenario where the stress state does not exceed the yield conditions, it does not exceed the ultimate load of the member.

Apart from the strut and tie model should represent a reasonable stress field and fulfil equilibrium, Engström (2015) states that geometrical application rules need to be adopted in a strut and tie model, which are governed by ensuring sufficient ductility and reasonable service state behaviour. Within the framework of this thesis, the following rules apply:

- Struts under concentrated forces should be spread out with an angle of 30 degrees.
- The angle at which a strut connects a single tie should exceed 45 degrees, and it is recommended to choose 60 degrees.
- Choosing an angle of 45 degrees for struts connecting two perpendicular ties is recommended, and it should not be less than 30 degrees.

In addition to geometrical application rules, nodes need to be structurally verified (Engström, 2015). In the framework of this master thesis, verification of the nodes underneath the anchorage plate is only applicable; see Figure 2.5.

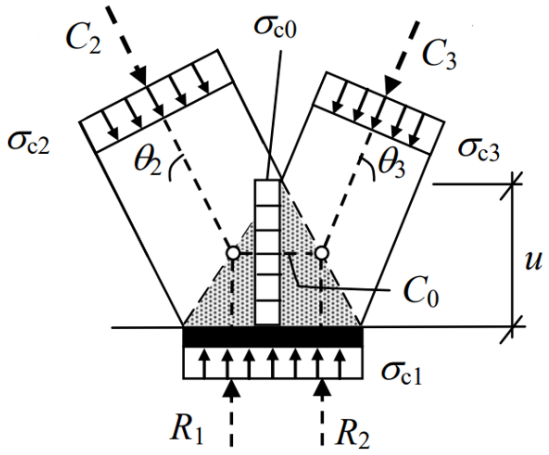

Figure 2.5: Compression nodes underneath the anchorage plate, retrieved from (Engström, 2015).

The nodes underneath the anchoring plate are subjected to a multiaxial stress state and are verified for local crushing according to (European Committee for Standardization, 2004) as the following (Engström, 2011):

$$\sigma_{Ed} < \sigma_{Rd} = \nu \cdot f_{ck}, \tag{2.1}$$

where $\nu = 3$.

Engström (2015) states that the structural capacity of nodes are only governed by σ_{c0} och σ_{c1}. According to (European Committee for Standardization, 2005), an anchorage zone with highly concentrated compression forces should also be structurally verified for highly concentrated forces behind the anchorage plate using a representative concrete prism.

The following geometrical requirements apply to the representative concrete prism:

$$max(\frac{c}{a}, \frac{c'}{a'}) \leq 1.25 \cdot \sqrt{\frac{c \cdot c'}{a \cdot a'}}, \tag{2.2}$$

where a, a' and c, c' are the dimensions of the force transfer unit and the concrete prism, respectively. The structural verification is done accordingly:

$$\frac{P}{c \cdot c'} < 0.6 \cdot f_{ck}, \tag{2.3}$$

where P is the prestressing force.

Additionally, the reinforcement must be dimensioned to verify sufficient structural capacity in the assumed ties. Ties, representing a distributed stress field, should be designed with a distributed reinforcement arrangement around the level of the prescribed tie. Ideally, the reinforcement should be distributed in a region smaller

than the length of the connecting strut. To ensure the sufficient capacity of the tie, the following equation apply(Engström, 2015):

$$A_s \geq \frac{T}{f_{yk}}, \tag{2.4}$$

where T is the force in the tie and A_s is the reinforcement amount.

European Committee for Standardization (2005) prescribes additional minimum surface reinforcement for an anchorage, according to Equation 2.5. The surface reinforcement prevents spalling of concrete near the surface.

$$A_{s.surf} \geq 0.03 \cdot \frac{P}{f_{yk}}, \tag{2.5}$$

where $A_{s.surf}$ is the minimum surface reinforcement amount.

Minimum tensile reinforcement is also specified according to European Committee for Standardization (2005), governed by the following equation:

$$A_s \geq 0.15 \cdot \frac{P}{f_{yk}}. \tag{2.6}$$

European Committee for Standardization (2005) also prescribes that minimum reinforcement should be provided according to the European Technical Assessment (ETA) approved bursting reinforcement for the specific anchorage system.

2.3 Concrete material model

Concrete is a composite material made up of aggregates, cement, and water. It is a heterogeneous material with the characteristics of relatively low tensile strength compared to its compressive strength. The material has non-linear behaviour, and in the following chapters, different material models for the concrete are presented.

2.3.1 Non-linear behaviour of concrete

The non-linear repsonse of the concrete becomes more pronounced as the ultimate state is reached (Kotsovos, 2015). The non-linear response reflects the fracture process under stress, and the cause of the response is the propagation of flaws or micro-cracks within the concrete. Micro-cracks and flaws can exist even before loading due to discontinuities in the cement paste matrix, voids from the casting, and discontinuities in the interfacial transition zone. When stresses and strains are applied to the boundaries of a concrete element, they induce the formation of a strain field within the element The characteristics of this strain field are influenced by the distribution of aggregates and cement paste, the element's geometry, and the distribution of and sizes of flaws within the material. Local strain concentrations develop throughout the material due to the incompatible deformation of the aggregates, cement paste and flaws. It results in strain concentrations, particularly

at flaws, which are considered to be the potential source of load-induced cracking. The spontaneous crack extension propagates if the strain concentrations exceed the strain capacity. The crack propagation is in the direction of the maximum applied compressive stress or orthogonal to the maximum principal tensile stress. Cracking occurs when an excess amount of strain energy needs to be released.

2.3.2 Uniaxial tension

When concrete is subjected to tensile stress, cracking is initiated when the tensile strength is reached (Plos et al., 2021). Once the cracking process starts and forms a fracture zone, stress transfer depends on the opening of the crack. The behaviour of concrete in tension can be determined by conducting a uniaxial tensile test. The crack development during the uniaxial tensile test can be divided into five stages, illustrated from stages a) to e) in Figure 2.6 (Plos, 2000).

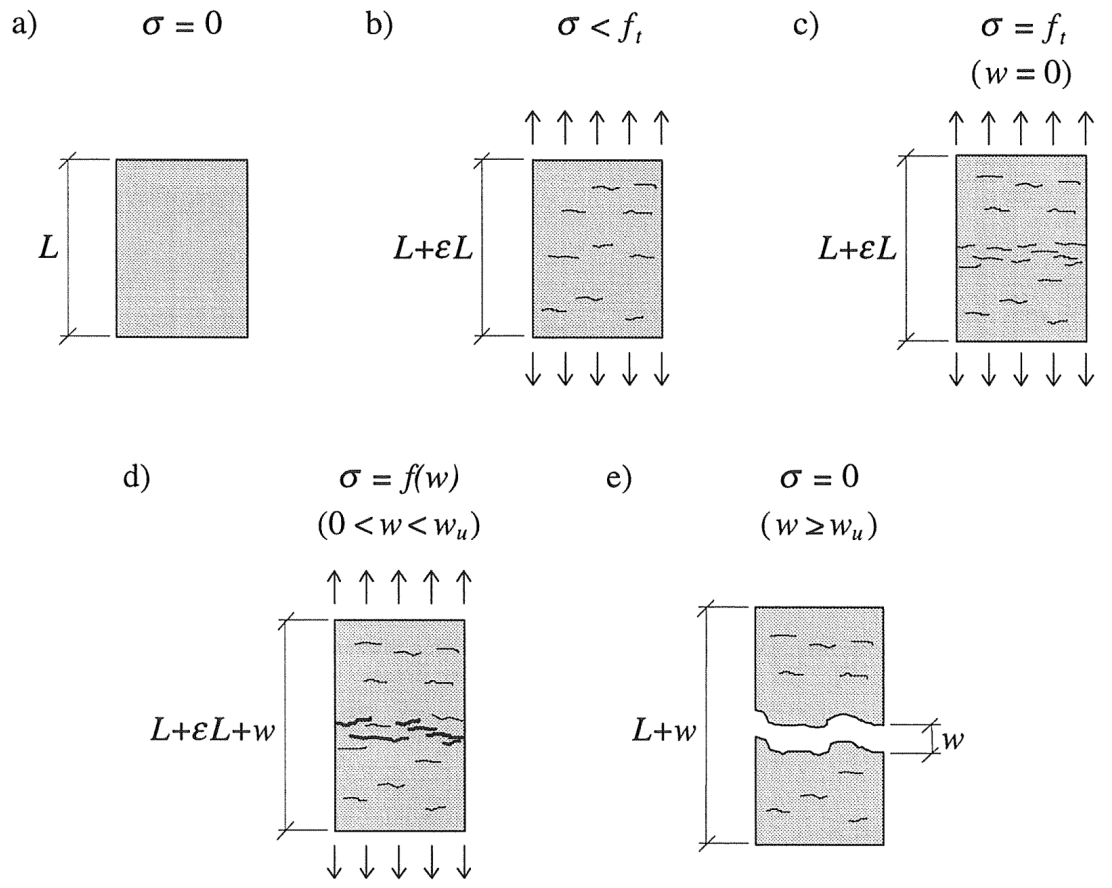

Figure 2.6: Different stages of the fracture process of uniaxial tensile stress, retrieved from (Plos, 2000).

The first stage (a) occurs when no load is applied to the specimen (Plos, 2000). In the second stage (b), tensile stresses in the concrete are below the tensile strength, and micro-cracks begin to form at some locations in the specimen. In the third stage,

stress reaches the tensile strength, causing micro-cracks to localise at the weakest section of the specimen, but no crack opening occurs. After reaching peak stress, shown in Figure 2.7, the specimen enters the fourth stage as crack opening initiates (d). In the fourth stage, the specimen undergoes strain-softening behaviour, and micro-cracks develop into macro-cracks (Hillerborg, 1985). As the material outside the fracture zone unloads, deformations increase as stress decreases. The amount of stresses transferred through the fracture zone depends on the crack opening w (Plos, 2000). In the fifth and final stage (e), the fracture zone is separate, and no stresses are further transferred through the fracture zone.

A stress-displacement relation for concrete, presented in Figure 2.7, can be obtained by conducting a uniaxial tensile test. According to Plos (2000), the stress-displacement results from a uniaxial tensile test cannot be directly translated into a general stress-strain relationship for concrete. Hence, the stress-displacement results are size-dependent. To convert stress-displacement into a general material property, it must be separated into an elastic stress-strain relationship for the material outside the fracture zone and a stress-crack opening relationship, illustrated in Figure 2.7. The area enclosed by the stress-crack opening relation represents the energy absorbed, referred to as fracture energy (G_F) (Hillerborg, 1985).

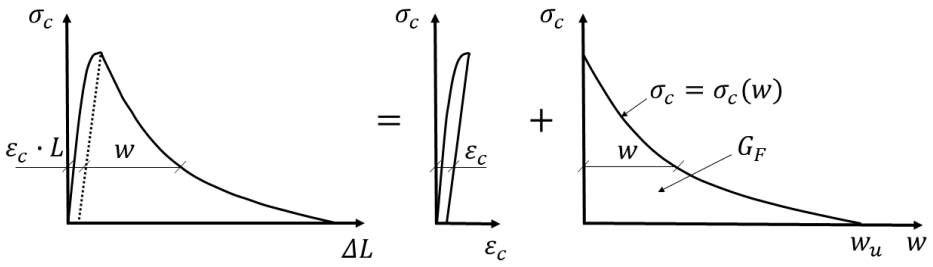

Figure 2.7: The stress-displacement relationship in a uniaxial tensile test of concrete (left), and how it is converted into an elastic-strain relation (middle) and a stress-crack opening relation (right). Adapted from (Plos et al., 2021).

2.3.3 Uniaxial compression

Figure 2.8 illustrates the stages for concrete cylinders subjected to uniaxial compression. In the first stage (a), the initial size of the specimen is depicted, as no loads are applied to the boundaries (Kotsovos, 2015). In the second stage (b), loads are applied to the horizontal boundaries of the specimen, causing lateral expansion without cracking. The expansion occurs due to the deformation of the concrete and the Poisson effect. In the third stage (c), cracks are formed in the central zone, in the loading direction. The lateral expansions at the cracked zone are incompatible with the lateral expansion at the uncracked zones, which induces internal forces. These internal forces restrain and increase the lateral expansion at the central and end zones, respectively. In the fourth stage, at least one of the end zones experiences a tensile principal stress component, resulting in crack propagation towards the end zone.

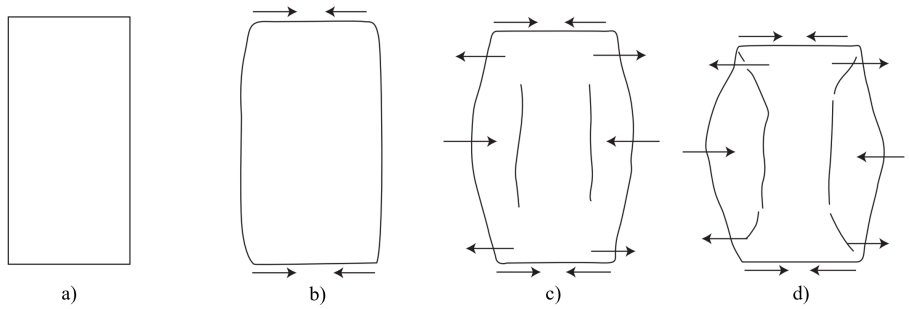

Figure 2.8: The behaviour of a concrete cylinder in uniaxial compression, adapted from (Kotsovos, 2015).

The compressive stress-strain relationship of concrete, as illustrated in Figure 2.9, can be obtained through a cylindrical test. The stress-strain relation in a cylindrical test is size-dependent, meaning that it cannot be regarded as a pure material property.

The compressive fracture energy and post-peak softening behaviour are influenced by the crack development during loading. Macrocracks initiate before the peak stress and localise after the peak stress is reached. At the steeper part of the descending branch of the stress-strain relation, the macrocracks extend towards the specimen's centre. At the flatter part of the descending branch, the macrocracks congeal. In the softening region, concrete within the damaged zone continues to strain while concrete outside the damaged zone unloads elastically. The undamaged zone only exists if the height of the specimen is greater than the damaged zone length.

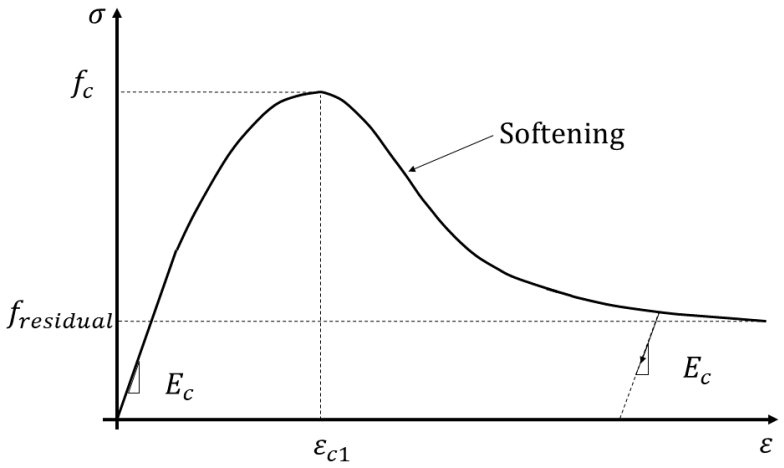

Figure 2.9: The characteristics of a stress-strain relation for Concrete in a compressive cylinder test, adapted from (Samani & Attard, 2012).

According to Markeset and Hillerborg, 1995, the formation of longitudinal cracks is accompanied by energy absorption in a similar manner as a pure tensile crack. A

portion of the fracture is absorbed by the formation of microcracks, and the rest is absorbed when longitudinal cracks open.

2.3.4 Multiaxial concrete behaviour

Multiaxial stress states often occur in strut-and-tie models, slabs, shells, and plates Geel (1998). In those areas, the uniaxial material models reach limits, and it is advantageous to utilise the multiaxial properties of concrete, due to increased load-bearing capacity and allowance for larger deformations. Figure 2.10 presents the strength surfaces of concrete, which can be obtained by performing a triaxial cell test. The figure presents the three compressive meridians and one of the three tensile meridians. It can be observed that the meridians open in the negative octants and the tensile meridian lies below the compressive meridian. Theoretically, there is no upper limit to the strength in triaxial compression.

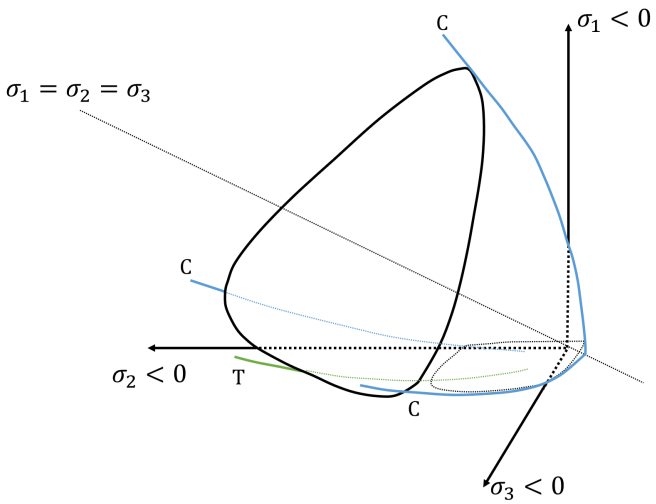

Figure 2.10: The strength surfaces formed by the compressive (blue) and the tensile meridian (green). Only one of the three tensile meridians is illustrated. Adapted from (Häussler-Combe, 2022).

2.3.4.1 Biaxial strength

The biaxial strength of concrete can be obtained from the triaxial strength, shown in Figure 2.10, when one of the principal stresses is zero or in a plane stress state (Häussler-Combe, 2022). Figure 2.11 presents the biaxial strength of concrete illustrated when the principal stress $\sigma_1 = 0$. The graph illustrates how the concrete strength increases or decreases depending on the applied stresses. It can be observed in the figure that the strength of concrete increases when subjected to compressive loading in both directions. The tensile strength remains almost the same as in the uniaxial case when subjected to tensile loading in both directions. However, the compressive and tensile strength both decrease when the concrete is subjected to combined compressive and tensile loading.

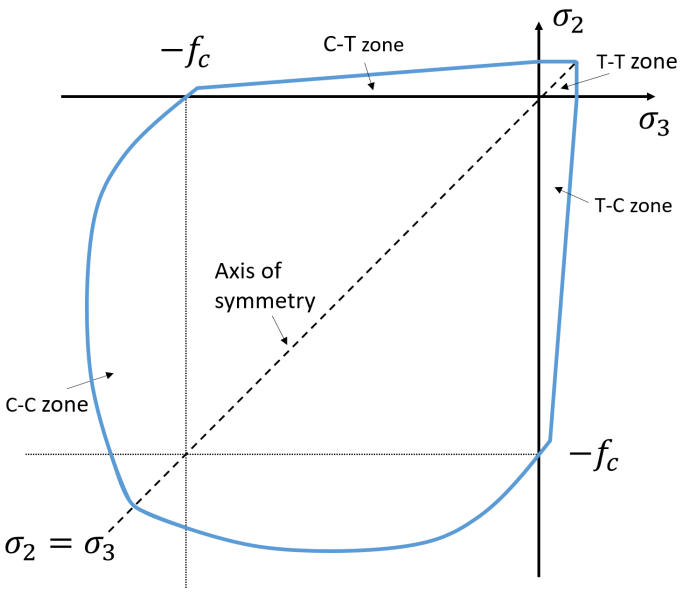

Figure 2.11: The biaxial strength of concrete, adapted from (Häussler-Combe, 2022).

The same observation was also made in the experimental investigation performed by Kupfer et al., 1969. In their study, they tested concrete in different biaxial loading and found that the strength increases in biaxial compressive loading. However, the compressive stress at failure in compressive-tensile loading decreases, and the strength of concrete in biaxial tension is approximately equal to its uniaxial tensile strength.

2.4 Steel fibre reinforced concrete

Concrete is a quasi-brittle material with relatively high compressive strength compared to tensile strength. By adding steel fibre to the concrete mix, the ductility of the concrete can be improved (Singh, 2017). Steel fibres are distributed randomly, occupy space in the interparticle space around coarse aggregates, and become embedded in the mortar mix. Steel fibers transfer tensile stresses, while concrete transfers both tensile and compressive stresses. The addition of steel fibres improves the mechanical properties of the concrete as the fibres can arrest the opening, widening and extension of micro-cracks. However, the fibres do not prevent the formation of microcracks and are not active at stresses when microcracks extend from the interfacial transition zone to the mortar. Consequently, the plain concrete and SFRC first crack occurs at nearly the same stress level.

After the first crack is formed, internal cracking in plain concrete and SFRC occurs in a similar manner (Singh, 2017). The crack extension is delayed between the aggregates since the fibres transfer both internal tensile stresses and tensile stress across existing cracks. The fibres can transfer the tensile stresses due to their high

tensile strength and anchorage in the mortar matrix. The additional capacity of tensile transfer enhances the tensile strain capacity of SFRC compared with plain concrete.

According to Löfgren (2005), the mechanical behaviour of SFRC depends on the volume fraction of fibres, the orientation of the fibres, and the pull-out resistance of the indiviual fibres. The pull-out resistance of the fibre depends on the type of fibre, its mechanical properties, the geometry and the mechanical properties of the fibre-matrix interface, the orientation of the fibres with respect to loading, and the mechanical properties of the matrix. The bonding of the fibre and matrix allows for the transmission of forces.

2.4.1 Steel fibres

According to Löfgren (2005), the mechanical and geometry of the fibre influence the behaviour of the SFRC. Steel fibres can either be made of carbon steel or stainless steel and the tensile strength can vary from 200 to 2600 MPa. Steel fibres are often made of high-strength steel. The steel fibres can be produced from deformed cold-drawn wire, deformed cut sheet, melt extracted, shaved cold-drawn wire, and fibres milled from blocks.

The performance of the steel fibre depends on the aspect ratio, fibre shape and surface deformation, and the surface treatment (Löfgren, 2005). Fibres can attain several cross-sections, and the most common is the circular cross-section. The fibres commonly vary in diameter from 0.2 to 1 mm and length from 10 to 60 mm. Roughening the surface of fibres or adjusting the shape of the fibres can improve the bonding between them and mortar. The shape of fibres can, for example, be straight, bow-shaped, crimped, twisted, or irregular. To increase anchorage, the ends of fibres can be designed as hooks or given shapes like paddles, end knobs, cones, etc.

2.4.2 Compressive behaviour

According to Löfgren (2005), the addition of fibres affects the behaviour of concrete under compression. If the volume fraction is less than 1%, the pre-crack properties is not affected. However, it does affect the post-peak behaviour by increasing the strain at crack localisation and ultimate strain. Figure 2.12 schematically shows how the volume fraction affects the post-peak behaviour of the SFRC, while Figure 2.13 schematically shows how the aspect ratios affect the post-cracking behaviour of concrete. The aspect ratio is the ratio of length to diameter of the steel fibre, and a higher aspect ratio improves the post-peak behaviour of the SFRC.

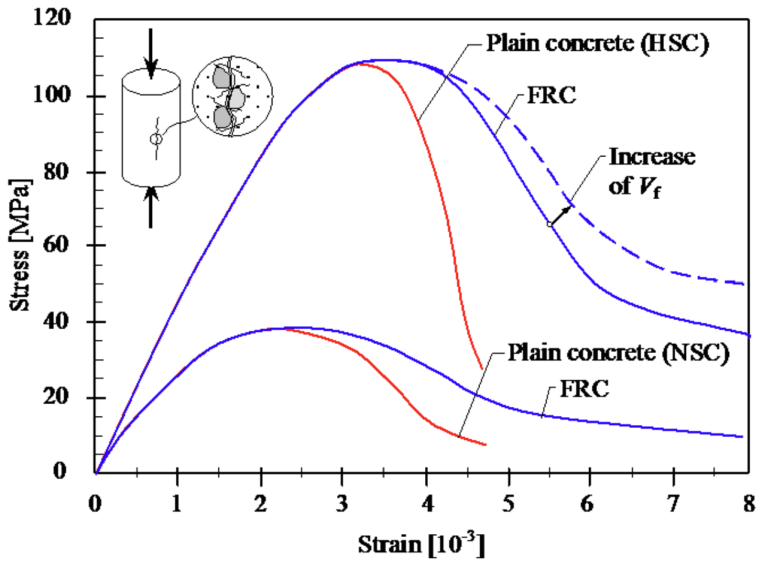

Figure 2.12: The typical stress-strain relationship for normal and high strength concrete and how the fibre dosage affects the post-peak behaviour. Retrieved from (Löfgren, 2005).

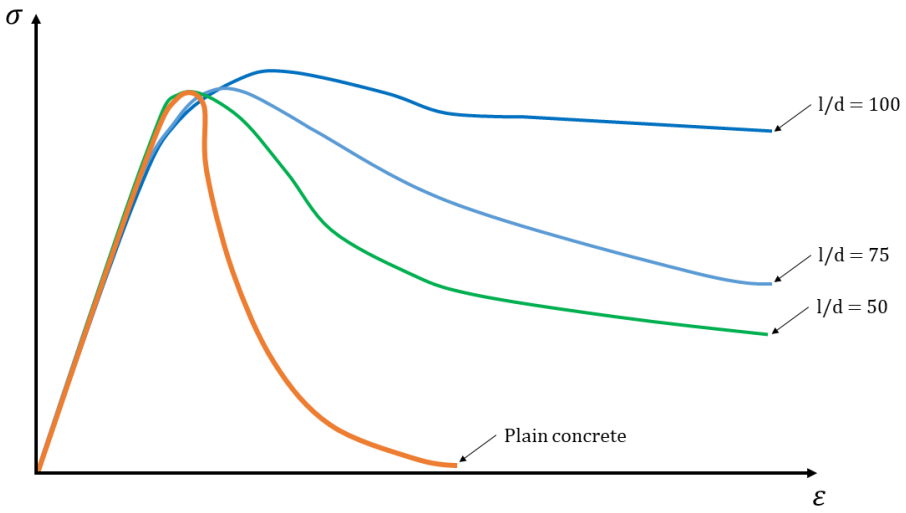

Figure 2.13: Typical stress-strain relationship for plain concrete and SFRC with different aspect ratios under compressive loading, adapted from (Singh, 2017).

2.4.3 Tensile behaviour

In tensile loading, adding steel fibers improves post-peak behavior, either by strain-softening or strain-hardening (Löfgren, 2005). The difference in the tensile post-peak behaviour of plain concrete and SFRC is schematically presented in Figure 2.14. If the volume fraction is low to moderate, the post-peak behaviour can be considered strain-softening. As discussed earlier in chapter 2.4, the fibres do not significantly affect the tensile strength and modulus of elasticity of the concrete before reaching the peak stress. However, the fibres affect the tensile fracture behaviour, the

fracture energy, and, therefore, the stress-strain relationship. The stress-crack and stress-strain relationship of SFRC must be determined through experimental testing such as the bending notch beam, uniaxial tensile test, wedge-split tests, etc.

Figure 2.14 presents the stress-strain relations for plain concrete and SFRC. The localisation of a single crack occurs at the peak-stress when $\sigma = \sigma_t$. The post-peak behaviour of SFRC is either strain-softening or strain-hardening, depending on whether the stress decreases or increases. After the localisation, the fibres are activated and transfer tensile forces across the crack (Singh, 2017). In case of strain hardening, new cracks continue to form, and the already-formed cracks grow and widen with increasing load. Fibres start to pull out after the peak stress is reached, leading to failure.

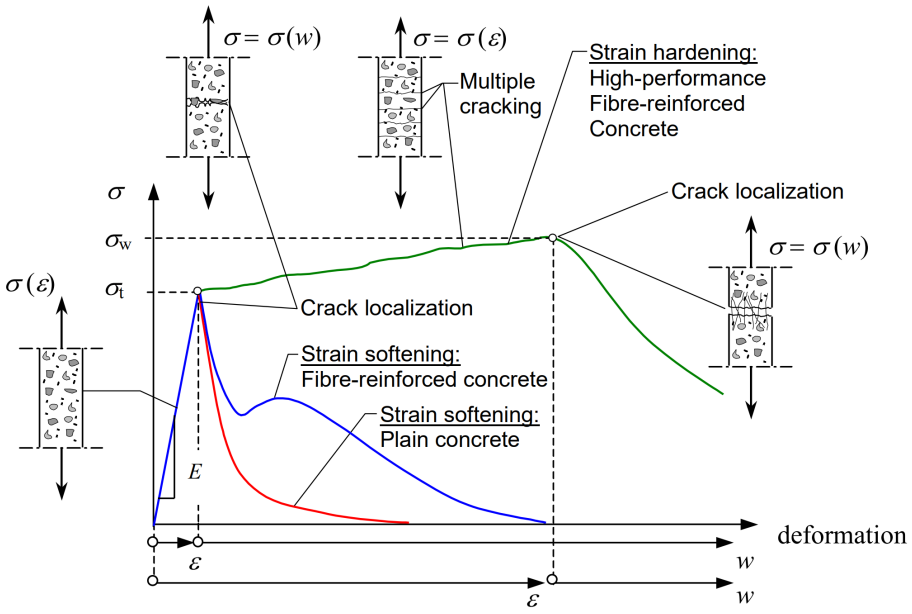

Figure 2.14: The tensile post-peak beaviour of plain concrete and SFRC, retrieved from (Löfgren, 2005).

2.5 Concrete and reinforcement interaction

The main concern when studying the interaction of concrete and reinforcement is how the stresses are transferred between the two materials. When there is a relative displacement between the concrete and reinforcement steel, bond stresses are generated (International Federation for Structural Concrete, 2013). Relative displacement often occurs in regions where tensile stresses are present, such as cracked regions. In those regions, the tensile stresses are transferred by the reinforcement across the cracks. In between the cracks, the tensioned concrete surrounding the reinforcement lowers the steel stress by the bonding interaction (Al-Emrani et al., 2011). This is called the tension-stiffening effect and is most pronounced immediately after crack formations.

There are two main approaches to describing the interaction between embedded reinforcement and concrete. One approach is to assume full interaction between the embedded reinforcement and concrete, whereas the other introduces a bond-slip relation between the concrete and embedded reinforcement. By assuming full interaction, the concrete closest to the reinforcement and the reinforcement will always have the same strain. When considering bond-slip, the bonding interaction is dependent on the reinforcement slip. Several models to describe the bond-slip relation of reinforced concrete exist. International Federation for Structural Concrete (2013) provides relations that described the local bond vs local slip for ribbed reinforcement bars, which satisfies the classification of high bond. The relations concern either pull-out or splitting failure, presented in Figure 2.15, where the last mentioned is divided into confined (Stirrups) or unconfined concrete. The splitting failure of unconfined concrete results from a sudden drop in bonding interaction with no residual stress. In comparison, the splitting of confined concrete results in residual stresses, represented by the plateau in Figure 2.15. During this plateau, advanced shearing and crushing of the concrete occur. A concrete member can be considered confined if there is a large concrete cover, dense transverse reinforcement or transverse compression.

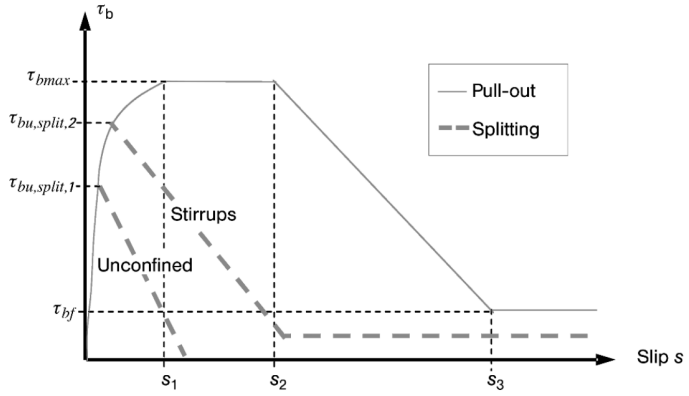

Figure 2.15: Relation between slip and bond stresses for pull-out failure and splitting failure for confined and unconfined concrete, respectively, retrieved from (International Federation for Structural Concrete, 2013).

The peak local bond resistance, $\tau_{bu.split.1}$, for good bonding conditions is determined as following:

$$\tau_{bu.split.1} = 7.0 \cdot (\frac{f_{cm}}{25})^{0.25} \tag{2.7}$$

s_1 is the corresponding slip value to $\tau_{bu.split.1}$ on the reference curve which is described as:

$$\tau_b = \tau_{bmax} \cdot (\frac{s}{s_1})^{\alpha} \quad \text{for} \quad 0 < s < s_1, \tag{2.8}$$

where $\alpha = 0.4$ and $\tau_{bmax} = \tau_{bu.split.1}$ for unconfined concrete.

2.6 Non-linear finite element analysis

Various material models, interaction models, and crack approaches can be used in non-linear finite element analysis (NLFEA). Commonly used crack approaches in NLFEA are the smeared crack approach and the discrete crack approach, which are explained in the following sub-chapters. Additionally, a crack localisation technique of the smeared approach, referred to as the weakened element technique, is explained.

2.6.1 Smeared crack approach

In the smeared crack approach, the crack discontinuity is smeared out over a continuum element using stress-strain relations. According to Plos (2000), the initial isotropic stress-strain relation is replaced by an orthotropic stress relation when a crack initiates. In the smeared crack approach, the crack localisation does not need to be known beforehand, and it can only detect regions where cracking is distributed. The localisation of individual cracks is not possible, but the crack orientation can be obtained from the model.

Cracking is assumed to be initiated when the principal tensile stresses exceed the tensile strength of the concrete. When cracking starts, orthotropy is introduced, and the axes of the orthotropy are fixed with respect to the crack orientations. After the initiation of cracks, the rotation of principal stress directions can cause cracks in concrete, which do not necessarily form orthogonal (Plos, 2000). If the cracks are fixed, and the incremental shear stiffness is positive, large shear stresses can be built up due to the rotation of principal stresses after crack initiation (Plos, 2000). However, new cracks can only form if the principal stress exceeds the tensile strength and the direction of the crack is fixed. This can be avoided by using a rotating crack, which allows the crack direction to co-rotate with the principal stress direction.

When modelling the smeared crack approach, the crack width is transformed into equivalent crack strains, which are smeared over a distributed zone. The distributed zone is defined as the crack bandwidth, denoted as h, depending on how the NLFEA is modelled.

2.6.2 Discrete crack approach

In the discrete crack approach, the crack is treated as a geometrical discontinuity by modelling a specific element where the crack is expected. According to Plos (2000), those elements can be modelled with either non-linear spring elements or interface elements. The interface element should be pre-defined at the location where crack formation will occur. The concrete should be modelled with continuity elements with non-linear material properties between the interface. Cracking is assumed to be initiated when the stresses normal to the plane exceed the tensile strength of concrete.

2.6.3 Weakened element technique

The weakened element technique is a method where finite elements that coincide with known cracks are assigned weakened material properties (Blomfors et al., 2020). The purpose of assigning weakened materials is to induce crack localisation at a predefined and expected location in the NLFEA. The weakened element technique utilises the smeared crack approach; therefore, a crack bandwidth must be specified.

2.6.4 Reinforcement interaction

Mainly, there are two approaches to model the stress-transferring between reinforcement and concrete process, either by assuming full interaction or introducing a bond-slip relation, which are further explained chapter **??**. Depending on the studied structural phenomenon, either approach can be advantageous.Plos et al. (2021) states that more localised crack patterns can be obtained if bond slip is included in the analysis, although it requires more input data than assuming full interaction between the materials. Modelling bond-slip is possible by inserting an interface material between concrete and reinforcement containing constitutive relations that describe the relation between stresses in the concrete and local deformations around the reinforcement bar (Plos, 2000). Figure 5.19a, obtained from Plos (2000), graphically describes the stress situation for a bar subjected to tension, where both shear stresses and normal stresses are developed. Figure 5.19b presents this stress situation's corresponding traction stresses and components on its mean contact surface.

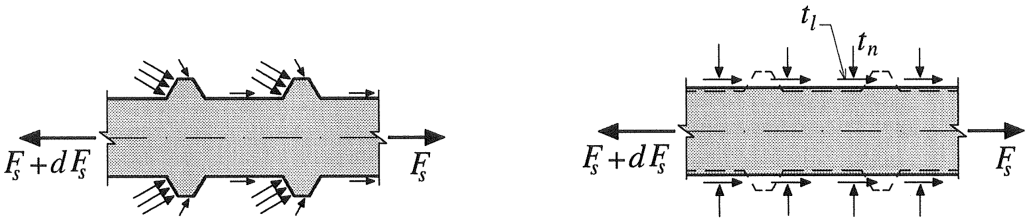

(a) Stresses on a reinforcement bar subjected to tension.

(b) Tractions acting on the mean contact surface.

Figure 2.16: Representation of stresses and tractions on a reinforcement bar subjected to tension, retrieved from (Plos, 2000).

2.7 Optical fiber sensors

The use of optical fiber sensors has shown promising results in evaluating the condition of civil engineering structures (Barrias et al., 2016)(Berrocal et al., 2021). Over the years, there has been a growing interest in using Distributed Optical Fiber Sensing (DOFS) for Structural Health Monitoring (SHM) of structural components. The traditional method of visually inspecting buildings, bridges and other engineering infrastructure has certain drawbacks in achieving consistent quality of assessment because different inspectors have varying levels of knowledge (Barrias et al., 2016). Berrocal et al. (2021) states that providing an adequate SHM for structures can be crucial for economic savings and effectiveness in terms of well-executed maintenance actions.

The application of discrete sensors (Fibre Bragg Grating and Fabry-Perot sensors) to measure strain and temperature in structural components constitutes a major part of the use of optical sensors (Fernandez et al., 2023). Discrete sensors can only measure strain in specific points along a fiber sensor. Consequently, uncertainties associated with monitoring the detailed behaviour of structural components, such as detecting cracks in reinforced concrete, may be present (Fernandez et al., 2023) (Glišić et al., 2013). Each discrete fibre also needs a connecting cable to a reading unit, which complicates the procedure when a large number of measurement points is desirable along a structural component. A distributed sensor, on the other hand, consists of one cable that is sensitive along the entire length and enables measurements based on its spatial resolution, the length between discrete points of which the measured parameter is averaged. Therefore, the distributed sensor technique enables the monitoring of larger regions without a large number of complex connection devices, making it less difficult and more economically beneficial (Glišić et al., 2013).

2.7.1 Application of DOFS

In the field of distributed sensors, three main techniques are available: Brillouin scattering, Raman scattering and Rayleigh scattering. All of these techniques involve studying changes in the backscattering light along a fiber, which in turn can be used to detect changes in temperature or strain along a fiber. Each technique are applicable for different fields as they differ regarding the properties of the scattering light. Changes in temperature mainly induce Raman scattering, whereas Brillouin and Rayleigh scattering technique can be applicable for measuring both strain and/or temperature changes (Fernandez et al., 2023) (Glišić et al., 2013). The main difference between Brilloiun and Rayleigh scattering principle is the spatial resolution and available measuring distances, where the latter is applicable for ranges up to 100 m and provides a spatial resolution of less than a millimetre. Brillouin scattering technique spans ranges up to 300 km, but the spatial resolution can not be less than 10 cm (Fernandez et al., 2023).

The principle of using Rayleigh scattering to obtain information about a structural component, such as detecting cracks in reinforced concrete, is based on Optical Frequency Domain Reflectometry (OFDR). The technique is based on initially storing the reference state of the scattering light along a certain fiber embedded or attached to a structural component. The reference state is later compared to the optical changes induced by external structural or thermal loading and by post-processing of the results, enabling output of temperature and/or strain changes along a fiber (Berrocal et al., 2021). A visualisation of the process is presented in Figure 2.17.

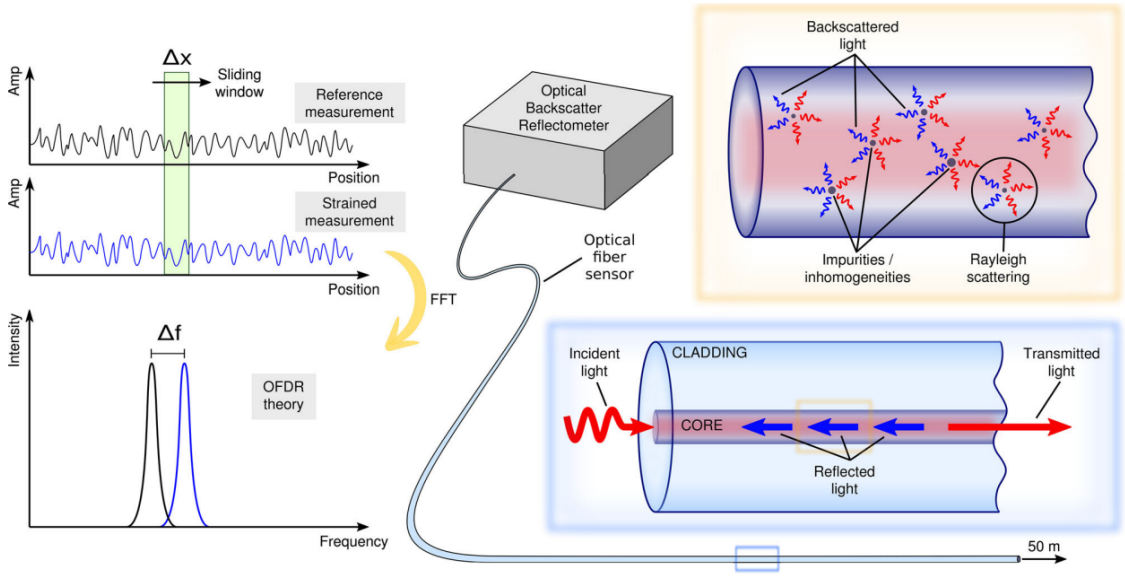

Figure 2.17: Process of DOFS using Rayleigh scattering based on OFDR, retrieved from Berrocal et al. (2021).

2.8 Digital image correlation

Digital image correlation (DIC) is a non-contact optical method for localising and measuring deformations and/or strains on the surface of a structural object (Omondi et al., 2016). The method has been used for various purposes within the civil engineering field, e.g., crack detection in reinforced beams, analysis of multiple-growing cracks in reinforced concrete slabs, and multi-axial fatigue testing of polymer materials (Gencturk et al., 2014).

Similarly to the principle for optical fiber, the DIC method is based on initially storing information through a reference picture of the studied object. Simultaneously as a load increment is applied to the structure, additional pictures are taken, and the induced strains and/or deformation are compared to the picture of the reference case. Through numerical post-processing of the information, the DIC system can provide the real-time structural behaviour of the studied structural component (Gencturk et al., 2014) (Omondi et al., 2016).

In order to properly execute a DIC, the studied object needs to be equipped with a stochastic surface pattern similar to the presented pattern in Figure 2.18. The stochastic pattern enables the localisation of pixels in the pictures, which are grouped into overlapping facets. The displacements and strains of the structure are then obtained by analysis of the deformed facets that distribute the studied surface (Gencturk et al., 2014). The appearance of the stochastic pattern has a great influence on the results provided by DIC and is related to the resolution of the black spots and their contrast level to the background. However, Gencturk et al. (2014) states the process of achieving acceptable results must be based on practical experience.

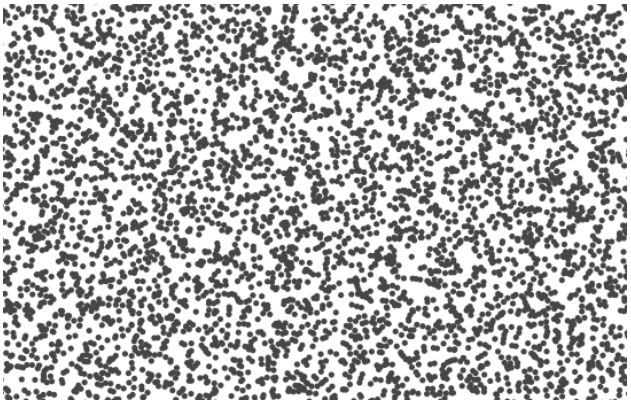

Figure 2.18: Example of a computer-rendered stochastic surface pattern.

3

Design and construction of specimens

The following chapter presents the working procedure for the final design of the specimens. It is initiated with design conditions, which define the framework of the design process. The chapter also presents the design procedure and choices for the reinforced concrete and fibre-reinforced concrete specimens, followed by NLFEA of the different configurations. Thereafter, the different steps of the construction process are explained, such as the monitoring scheme, assembly procedure and surface preparations.

3.1 Design conditions

3.1.1 Material

In European Committee for Standardization (2004) the recommended minimum concrete class for typical exposure classes of a bridge is C35/45, concerning the durability aspects of a bridge. However, a lower concrete class was chosen in order to early cracking due to limitations in the testing facilities. The concrete class for the reinforced concrete and SFRC was chosen to C30/37. The steel fibres used in the SFRC were Dramix 4D 65/35 BG, shown in Figure 3.1.

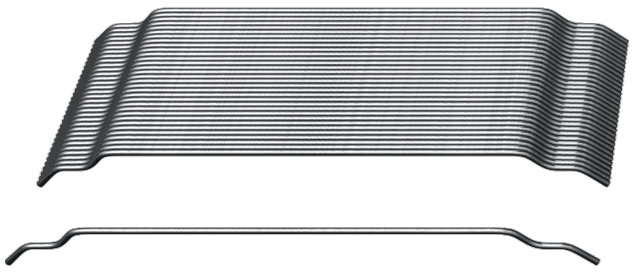

Figure 3.1: Steel fibre Dramix 4D 65/35 BG, retrieved from (Bekaert, 2023).

3.1.2 Anchorage system

The chosen anchorage system is a circular system in the XM-series provided by the company CCL. The circular system was chosen to achieve a symmetric load spreading in the concrete specimens. It was also desirable to have a system with relatively low capacity to have margins to the maximum load capacity of the test rig. The available anchorage system with the lowest capacity in the XM-series was XM20, designed for a characteristic tendon force of 1116 kN. The product sheet of the anchorage system XM20 is presented in Appendix I.

3.1.3 Geometry

A literature review was conducted to find a suitable initial geometry of specimens by reviewing other studies that had investigated the failure of anchorage zones. In the study by Lee and Kim (2019), an experimental investigation was conducted to improve the bursting force equation force anchoring systems. The maximum load in the experiment was approximately 750 kN and the specimen had the geometry 250x250x600 mm (width, depth, height). The maximum test rig used in this master's thesis was of the same magnitude and, therefore, was reasonable. However, since the XM20 anchorage was larger, it was necessary to increase the cross-section slightly. It was desirable to save material and to facilitate the construction and testing process. A certain height for investigating the entire discontinuity region was needed. Thus, the height-to-width ratio was chosen to 1.5, to ensure having a full discontinuity region. Based on this, several linear elastic finite element analyses were conducted to find a suitable geometry with the desired stress distributions. The linear elastic analyses showed that the suitable dimensions of the specimen would be 300x300x450 mm (width, depth, height).

3.2 Design of transversal reinforcement

The reinforced concrete configuration was designed for the allowed characteristic tendon force for the chosen anchorage system XM20 provided by the company CCL. The design is based on the strut and tie method described in chapter 2.2.1 with design recommendations and structural verifications according to European Committee for Standardization (2004) and Engström (2015).

3.2.1 Strut and tie model

To represent the resulting force flow in the specimen due to centric loading, a 3D strut and tie model was developed for the specimen. To properly execute the design procedure, it was assumed that no ducts were inserted in the specimen. Additionally, the circular load transfer unit was assumed to be transferred to an equivalent squared shape with the same area. The concentrated forces acting on the tendon head were assumed to act in the quarters of the equivalent squared-shaped load transfer plate, i.e. no concerns regarding potential load spreading due to the ribs on the anchorage system were made. The concentrated forces were assumed to deviate

with an angle of 30 degrees and were limited by the centre of gravity in each quarter of the specimen. In the intersection between the deviation of the forces and the centre of each quarter, the forces were tied back, and the flow was assumed to be vertically straight downwards. The strut and tie model was first conducted for a diagonal section, which facilitated that the deviating struts had the right angle. An illustration of the designed strut and tie model is presented in Figure 3.2.

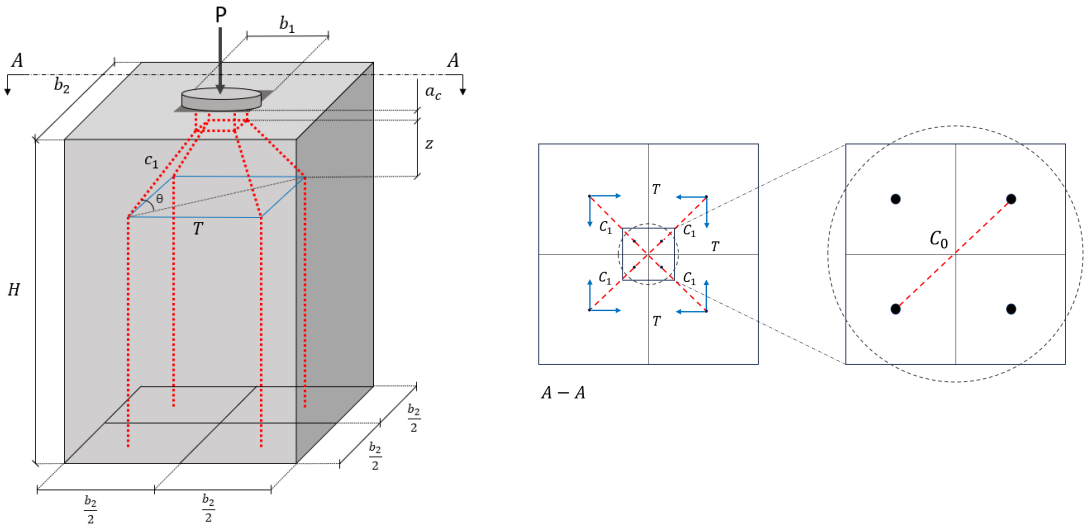

Figure 3.2: Adopted strut and tie model for the reinforced concrete specimens.

3.2.2 Structural verifications

Based on the adopted strut and tie model established from the characteristic tendon force, the resulting tie forces were evaluated to 114 kN, see Appendix J. The capacity, governed by Equation 2.4, was attained by inserting three 10 mm diameter stirrups with a centre-to-centre distance of 50 mm, see Appendix J. The stirrups were arranged with their centre of gravity in the prescribed tie, which was determined to 90 mm from the top surface. The reinforcement amount was sufficient according to the minimum reinforcement prescribed in European Committee for Standardization (2005). According to European Committee for Standardization (2005), additional surface reinforcement should be designed to avoid the spalling of concrete at the surface parallel to the load-transferring plate. The amount of surface reinforcement is governed by Equation 2.5, which was attained by inserting one 8 mm diameter stirrup, see Appendix J.

The nodes underneath the load-transferring plate were verified according to Equation 2.1. The compressive forces were also verified according the prescription in Engström (2015), described in Chapter 2.2.1. The equivalent prism behind the anchoring plate was assumed to be equal size to the specimen, which was geometrically verified according to Equation 2.2. The compression forces within the prism were structurally verified according to Equation 2.3.

3.2.3 Local bond-slip relationship

The local bond-slip relation in Chapter 2.5 was adopted to model the bond interaction of the concrete and reinforcement in the NLFEA. It was assumed that no pull-out failure would occur for the studied specimens. It was also assumed that the specimens were unconfined, due to the small concrete cover and absence of transversal compression and reinforcement. As unconfined concrete does not include a constant bond resistance for which advanced shearing and splitting of concrete occurs, s1 = s2 in Figure 2.15. The slip corresponding to a stress free interaction between concrete and reinforcement is determined as $s_3 = 1.2 \cdot s_1$. Based on this, along with α set to 0.4, the bond relation could be determined using Equations 2.7 -2.8. The resulting bond-slip relation is presented in Figure 3.3.

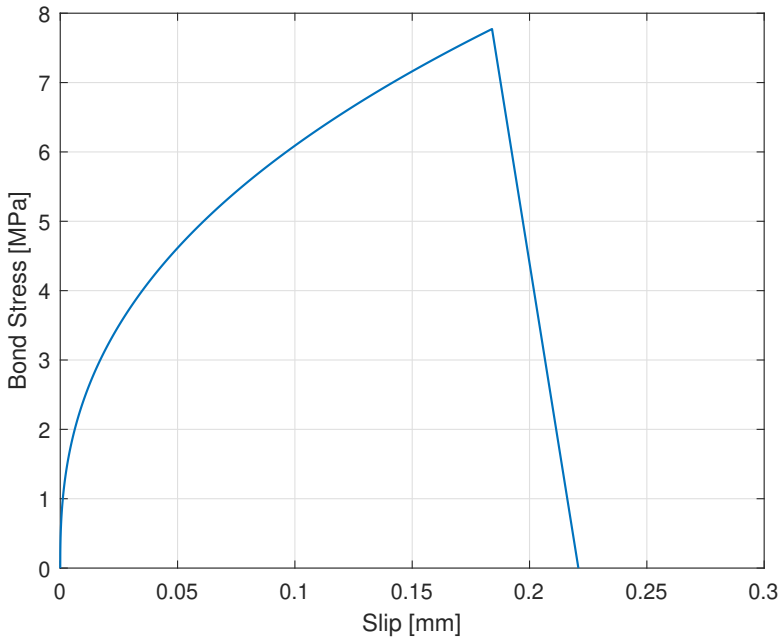

Figure 3.3: Bond-slip relation describing the interaction of concrete and reinforcement for splitting failure.

3.3 Design steel fibre reinforced concrete

The properties of the steel fibre reinforced concrete depend on several parameters such as the volume fraction of fibres, material properties of the fibre, the bond between fibre and concrete, and the mechanical properties of the matrix. Galeote et al. (2022) conducted a statistical analysis on a database of residual strengths of SFRC and proposed performance equations. The analysis resulted in several relations describing the residuals strength depending on different parameters of the SFRC. Galeote et al. (2022) proposed equations describing how different fibre parameters correlate with the residual strength. Two of these relations for residual strength and multiple hooked fibres are presented in Equations 3.1 and 3.2:

$$\frac{f_{R1}}{(f_{cm})^{0.5}} = 0.097 \cdot V_f \lambda f_{uf} E_f^{0.5} \tag{3.1}$$

$$\frac{f_{R3}}{(f_{cm})^{0.5}} = 0.102 \cdot V_f \lambda f_{uf} E_f^{0.5} \tag{3.2}$$

where f_{cm} is the average compressive strength of the concrete, V_f is the volume fraction, λ is the aspect ratio, f_{uf} is the ultimate tensile strength of the fibres, and E_f is the modulus of elasticity for the fibres.

The relations in Equations 3.1 and 3.2 were used to estimate the residual strength of the SFRC to be able to perform a NLFEA before the experimental testing of the SFRC was performed. In the experiment, the fibres Dramix 4D 65/35 BG were be used, and the fibre properties are presented in Table 3.1.

Table 3.1: Material properties of Dramix 4D 65/35 BG, retrieved from Bekaert, 2023.

Dimension	Symbol	Value
Youngs's modulus	E_f	210 GPa
Tensile strength	f_{uf}	1 850 MPa
Strain at ultimate strength	ϵ_{uf}	0.8%
Length	l	35 mm
Diameter	d	0.55 mm
Aspect ratio	$\lambda = l/d$	65

In practice, a volume fraction of 0.5% is often used to ensure proper workability of the concrete and to provide enough fibre to influence the behaviour of the composite material. Therefore, the volume fraction was chosen to be 0.5% in the thesis to illustrate a realistic scenario of what is achievable in the construction industry. By incorporating the properties of the fibres, the concrete class and the volume fraction, it was possible to estimate the residual strengths of the SFRC. The estimations were derived from Equations 3.1 and 3.2, and Table 3.2 presents the resulting estimated residual strengths of the SFRC.

Table 3.2: Estimated residual strength of the SFRC.

Dimension	Symbol	Value
Characteristic flexural strength at CMOD 0.5 mm	f_{R1}	3.71 MPa
Characteristic flexural strength at CMOD 2.5 mm	f_{R3}	3.90 MPa
Analytical formula	f_{R1}/f_{R3}	0.95

According to Kanstad (2021), the post-cracking strength of an SFRC is classified based on the residual strength and the f_{R1}/f_{R3}-ratio. The f_{R1}/f_{R3}-ratio, which indicates ductility, is represented by a letter from a to e, depending on the ratio. Based on the estimated residual strengths and the ratio presented in Table 3.2, the theoretical class of the SFRC matrix was 4c.

Kanstad (2021) describes a constitutive law of SFRC which may be utilised in the design. The constitute law is a tensile stress-strain relation of SFRC, and it is presented in Figure 3.4. The stress-strain can be derived by employing Equations 3.3 through 3.9.

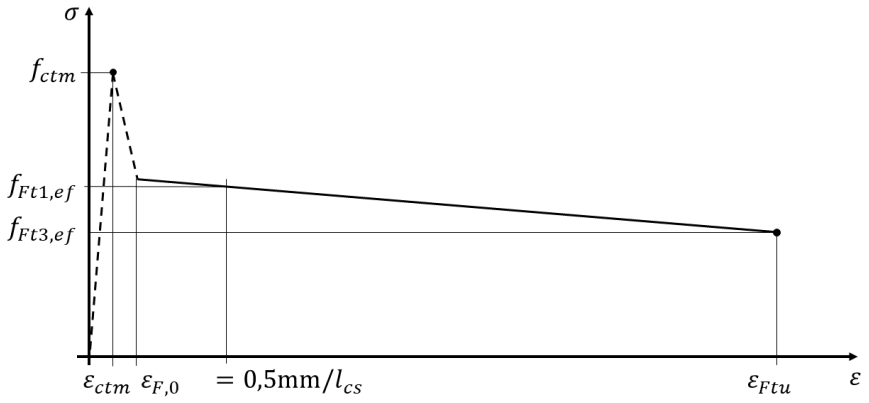

Figure 3.4: Constitutive law for structural analysis of SFRC, adapted from (Kanstad, 2021).

$$f_{Ft1,ef} = \kappa_O \cdot 0.37 f_{R1} \tag{3.3}$$

$$f_{Ft3,ef} = \kappa_O \cdot (0.57 f_{R3} - 0.26 f_{R1}) \tag{3.4}$$

$$l_{cs} = min\,(h, s_{rm}) \tag{3.5}$$

$$\epsilon_{Ftu} = w_u/l_{cs} \leq 2.5\text{mm}/l_{cs} \leq \epsilon_{Ftud} \tag{3.6}$$

$$s_{rm} = 0.75 \cdot S_{r,max,cal} \tag{3.7}$$

$$\epsilon_{ctm} = f_{ctm}/E_{cm} \tag{3.8}$$

$$\epsilon_{F,0} = 2 \cdot \epsilon_{ctm} \tag{3.9}$$

In Equations 3.3 and 3.4, κ_O represents the orientation factor that adjusts the residual strengths based on the fibre orientations (Kanstad, 2021). Since the anchorage zone is considered a discontinuity region, the orientation factor was set to $\kappa_O = 0.5$, as recommended for ties in strut and tie models.

The stress-strain law for softening materials depends on identifying the crack width and structural characteristic length (International Federation for Structural Concrete, 2013). The structural characteristic length, denoted as l_{cs}, is a variable used

to transform the crack width (w) into the corresponding stress-strain relationship. In Equation 3.5, the structural length is defined as the minimum of the average crack distance (s_{rm}) and the depth to the neutral axis (h). Since these parameters were unknown, the structural length was assumed to be $l_{cs} = 125$ mm, which is a recommended simplification by Kanstad (2021).

In Equation 3.6, the ultimate tensile strain (ϵ_{Ftu}) of the stress-strain relationship is defined. Since the ultimate crack width was unknown in the design phase, the ultimate tensile strain was set to $\epsilon_{Ftu} = 0.02$, as recommended. By utilising Equations 3.3-3.9, the stress-strain relationship of SFRC was defined and is presented in Figure 3.5. The stress-strain relationship shown in Figure 3.5 was employed in the NLFEA in the design phase.

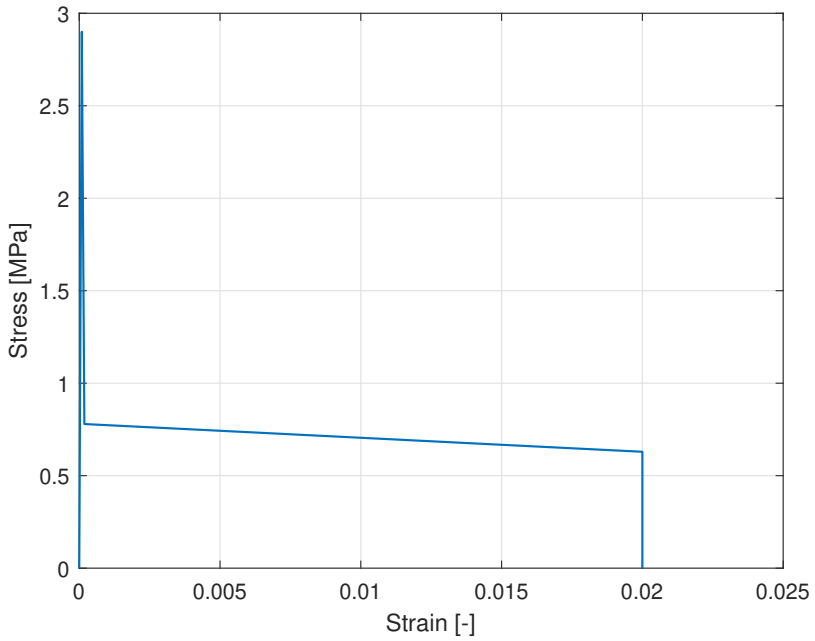

Figure 3.5: Stress-strain relationship for SFRC obtained using Equations 3.3-3.9.

3.4 Numerical simulation

To simulate the structural response of the different configurations, an NLFEA was conducted using the commercial software Diana 10.8 developed by DIANA FEA. The NLFEA was conducted to validate dimensions, material, and behaviour under compressive loading. The employed modelling approaches are described in the following sections.

3.4.1 General modelling choices

The configurations were modelled as cuboids with a width and depth of 0.3 m and a height of 0.45 m. The post-tensioning system was modelled as an empty cone, and the duct was modelled as an empty cylinder matching the dimensions of the XM20 post-pensioning system, which are presented in Appendix I. The applied force was assumed to act as a pressure load on the tendon head, transferring the force to the concrete specimen through an embedded cylindrical load transfer plate. A strip of 0.035 m of concrete around the cylindrical load transfer plate was modelled as an elastic material, which was done to prevent an unlikely failure mode. If the concrete cylinder was modelled with non-linear material, cracks localised around the load-transferring plate, causing the model to diverge at an unreasonably low load level. The specimen was modelled using two element sizes: 0.02 m for the tendon head, load transferring plate, elastic concrete cylinder, and strip of weakened elements; and 0.04 m for the rest of the specimen. The overview of the specimen modelled with the solids in Figure 3.6a is depicted along with the specimen with the elements and mesh in Figure 3.6b.

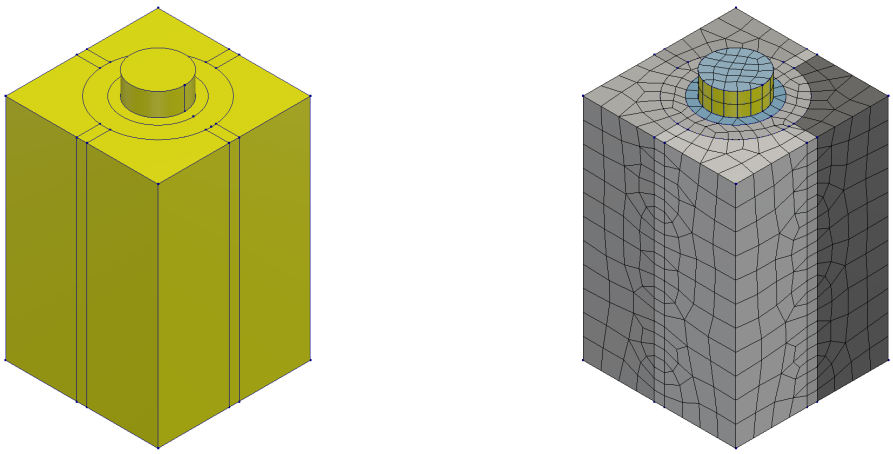

(a) Three-dimensional model showing the geometry.

(b) Three-dimensional model showing the element mesh.

Figure 3.6: The three-dimensional model of the configurations consisting of solid elements.

3.4.2 Material

Plain concrete and SFRC materials were modelled as non-linear materials, with material models describing their non-linear behaviour in compression and tension. Both plain concrete and SFRC utilize the ideal compression curve in compression, presented in Figure 3.7a. The Hordijk curve presented in Figure 3.7b was used to describe the tensile behaviour of plain concrete, while the tensile behaviour of SFRC was modelled by implementing the constitutive law presented in Figure 3.5. The reinforcement was modelled with von Mises plasticity without hardening, and the interaction with the concrete was represented by a bond-slip relation, as described in Chapter 2.5.

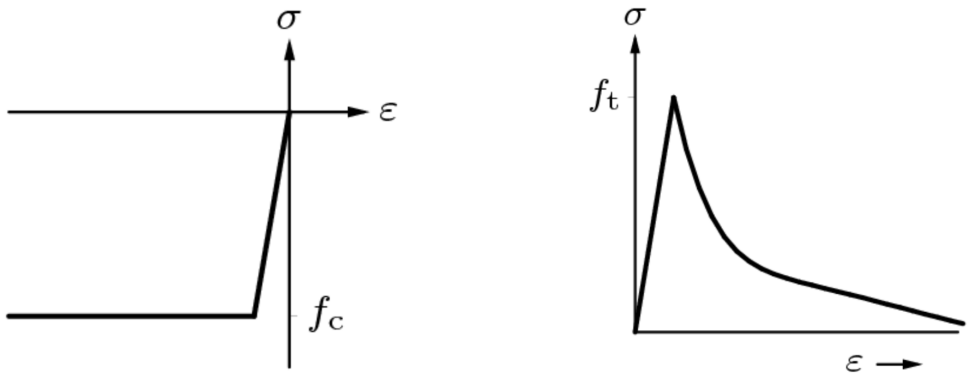

(a) Ideal compression curve. **(b)** Hordjik tension softening curve.

Figure 3.7: Non-linear material models used in FEA, retrieved from (Ferreira, 2024).

3.4.3 Crack modelling approach

Chapter 2.6.1 through 2.6.3 describe various crack modelling approaches, including the smeared crack approach and discrete crack approach. The smeared crack approach was chosen, and a vertical row with weakened elements was placed at the centre of each side with reduced strength properties. The tensile strength and fracture energy of the concrete was reduced by 10%, and the residual tensile strength parameters of the SFRC were also decreased by 10%. The weak elements were inserted to induce crack localisation at the expected location for all configurations. It was also assumed that a crack would localise within one element row. Therefore, the crack bandwidth was chosen equal to the element size. The crack pattern obtained from the NLFEA seemed reasonable, with a burst crack localised where expected and realistic crack development throughout the specimen.

In DIANA it is possible to define the crack orientation as rotating, fixed, or rotating to fixed. As described in section 2.6.1, the different crack orientation approaches affect the cracking development. The rotating crack orientation was chosen for all configurations. This was done to prevent unreasonable large crack widths in the region surrounding the edge of the anchorage plate. Similar crack localisation occur

around the elastic cylinder but with smaller crack widths. This caused the analysis to diverge at a low load level. Using rotating crack orientation, the cracks around the elastic concrete cylinder could rotate, allowing convergence for larger load levels.

3.4.4 Mesh

The element size of the weakened elements and the rest of the concrete was 0.02 m and 0.04 m, respectively. Hexahedral elements were implemented to create a smooth transition between the weakened element row and the rest of the specimen. Using weakened elements with hexahedral elements resulted in a crack pattern and crack widths that appeared reasonable for an anchorage zone.

3.4.5 Analysis

The structural non-linear analysis was performed for the different configurations, considering the physically non-linear effects. The Newton-Raphson solution method was used together with energy, displacement, or force as convergence norms. The analysis was performed with a load step of 4 kN, and the maximum number of iterations was approximately 450.

3.4.6 Preliminary results and design of specimens

The purpose of the thesis includes studying the post-cracking behaviour of different concrete anchorage zones. Studying the results from the NLFEA, it was numerically verified that the three specimens cracked and reached the desirable structural behaviour for the maximum load of the test rig. The resulting design of the structural components for each configuration is visualised in Figure 3.8

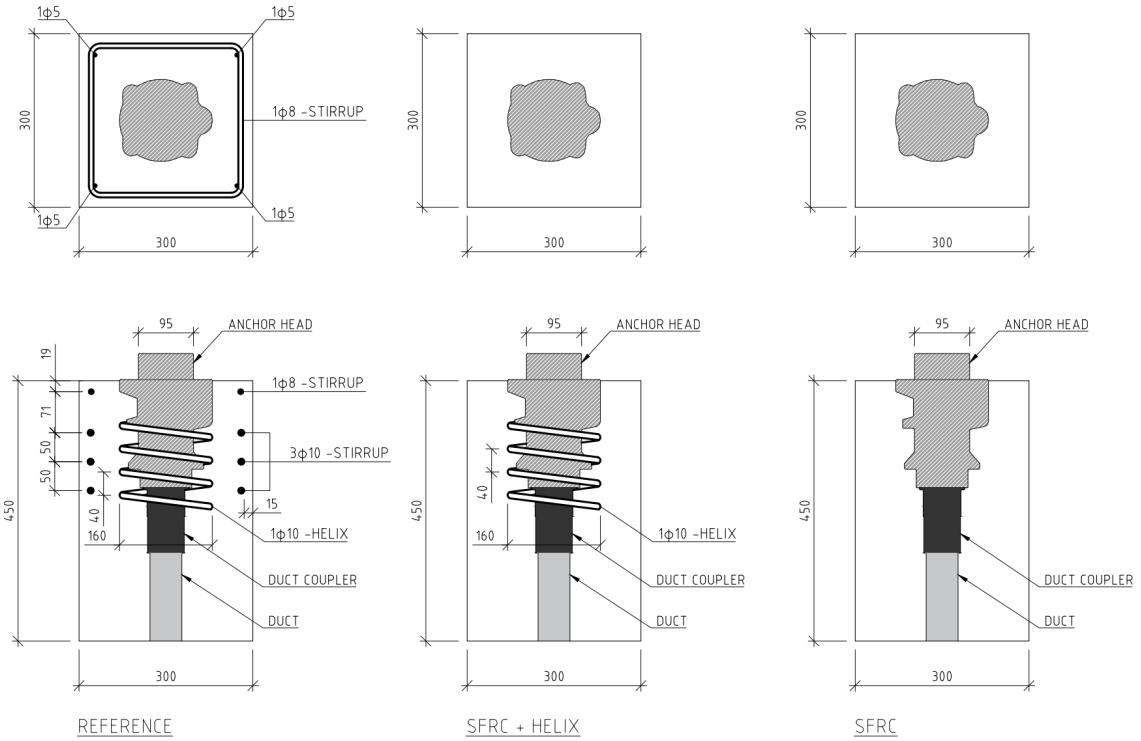

Figure 3.8: Top view and side view of three different configurations (Reference, SFRC + Helix and SFRC) along with their corresponding structural components.

Each specimen contained approximately 39 litres of concrete, and estimated reinforcement steel quantities for the different configurations are listed in Table 3.3.

Table 3.3: The calculated steel quantity used in the configurations.

Configuration	Steel Quantity
Reference	3.6 kg
SFRC + Helix	2.8 kg
SFRC	1.5 kg

The load-displacement curve was obtained for the most centric node located on top of the anchor head. The branches of the load-displacement curves presented in Figure 3.9 indicate cracking of the specimens, which was also verified by studying the crack and strain distribution in NLFEA.

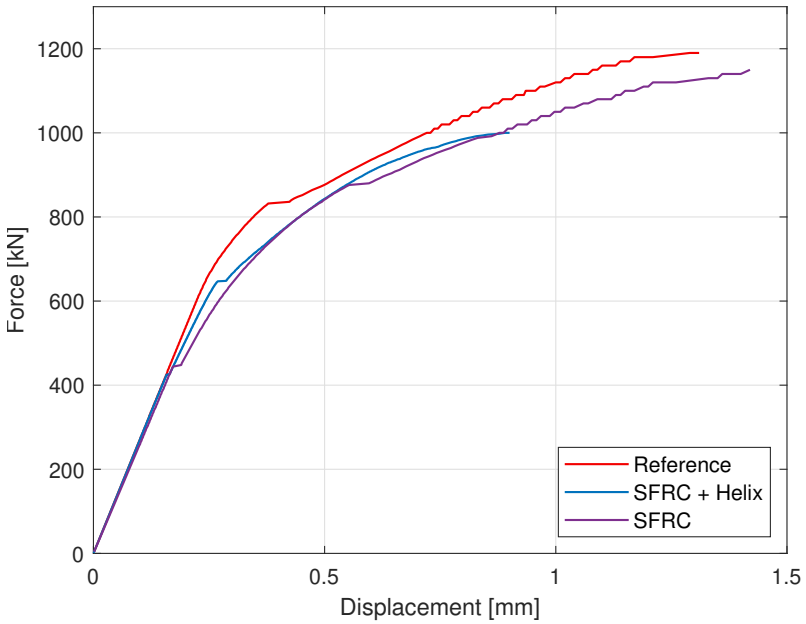

Figure 3.9: Load-displacement curve obtained from the FEA.

3.5 Design of fibre optics arrangement

The objective of the design of the fibre optics was to enable the monitoring of three-dimensional effects during the loading procedure. To achieve this, the fibre optics were arranged in a spiral shape, which enabled measuring of the tangential strain in all levels in the specimens. From the strain measurements, the localisation of cracks and crack widths could be evaluated. Two fibre spirals were desired in the specimen, one at the helix reinforcement and one near the outer faces.

3.5.1 Fibre optic type

A robust DOFS type that could withstand impacts during casting and load testing was desirable. The chosen type was Solifos' BRUsens DSS V9 grip with an outer diameter of 3.2 mm. The fiber sensor has a protective steel tube with additional ribbed cladding on the outside to increase its strain transfer. The fiber can measure strain up to 10000 $\mu\epsilon$.

3.5.2 Design of fiber optics support

The objective of supporting the fiber optics was to create a structure that maintains the fiber optics in their intended position throughout the casting process. The support should be designed to minimise its contribution of reinforcing the concrete. It was therefore chosen to construct the spiral using plastic material, which made it possible to 3D-print parts and design the spiral with high accuracy. The design of the support should facilitate the interaction between concrete and fibre optics such that the measured strains in the fiber optics represent the strains in the concrete. The spiral should also be designed to minimise the segregation of aggregates and steel fibres during casting. To increase its interaction with the concrete and minimise segregation, the spiral was designed with equally spaced holes along its length and with a certain pitch. To be able to build the spiral at the wanted dimensions, the spiral was divided into quarters and printed individually. This was done due to limited printing and avoiding an unreasonable amount of waste coming from the printing process. Dividing them into quarters also facilitated an efficient assembly of the spiral and room for height adjustments of the spiral later in the process.

The quarters were designed as a circle sector with an centre angle of 110°to ensure a smooth transition of the fiber optics between the quarter parts. Figures 3.10a and 3.10b present 3D drawings with dimensions of a quarter part in the outer and inner spiral presented, respectively. The outer and inner spiral were both supported by threaded rods with a diameter of 5 mm. The threaded rods for the outer spiral were attached with nuts and drilled through the form bottom, whereas the threaded rods for the inner spiral were attached to the predrilled holes in the anchorage system. The position of the quarters was kept in place by nuts at the specific height levels. The pitch of the spiral was facilitated by distances made of plastic pipes between each turn. The height of the distances was 25 mm and 20 mm for the outer and inner spirals, respectively. Nuts were screwed on top of each rod to keep the spiral stable and secure its dimensions.

To ensure the consistent pitch of the fiber optics, an embedded notch for the fiber optics was designed in the spiral. The pitch of the fiber optics in the outer spiral was set to 50 mm per turn. The inner spiral was designed with a pitch of 40 mm to replicate the helix reinforcements. Consequently, the different pitches resulted in different heights of the quarter parts. The height of the quarters of the inner and outer spiral were 10 mm and 12.5 mm, respectively. The thickness of the quarter parts was 5 mm for both spirals, and the spacing and width of the holes were 5 mm and 2.1 mm, respectively. The height of the hole in the outer and inner quarter was 7 mm and 6 mm, respectively.

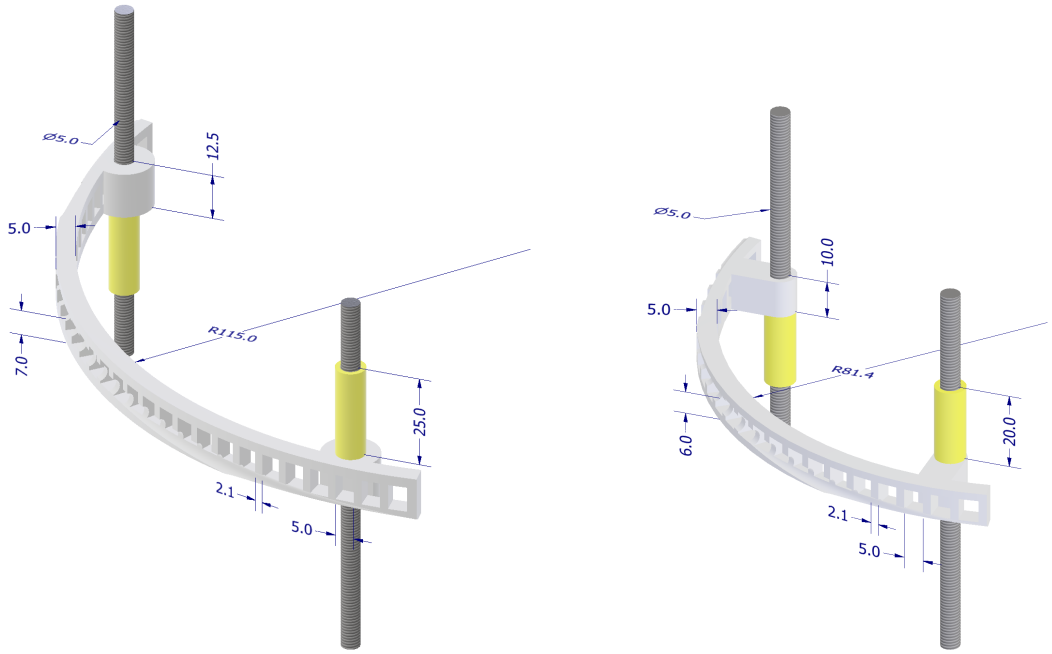

(a) Outer quarter **(b)** Inner quarter

Figure 3.10: Dimensions of the plastic quarters in the outer and inner spiral.

3.5.2.1 3D-printing of the support structure

The plastic quarters were designed in Inventor Professional 2024 by Autodesk and exported as STL files. PrusaSlicer 2.7.1 were used to convert the STL files to G-codes with instructions for the 3D printing. The parts were 3D-printed on the Original Prusa MK4 printer, which was equipped with an Input Shaper nozzle with a diameter of 0.4 mm. E-PLA material with a thickness of 1.75 mm was utilized for the printing process, and support material was only employed for support enforcement.

3.5.3 Attachement of the fiber optics

Both the last quarter and first quarter in the inner and outer spiral were designed to stop the pitch and facilitate a perpendicular attachment to the form. Therefore, these quarters were designed with a different notch that was kept horizontal from the centre of the quarter. The fiber optics cables were tensioned by special anchorage devices attached to the form. The anchorage devices consisted of a threaded cylinder in which 3D-printed wedges with the same surface pattern as the optic cable were placed. The cylinder was enveloped by a nut and by screwing it, the cylinder where pushed out from the form resulting in tensioning the fiber optics cable. The wedges in the cylinder prevented movement of the cable while tensioning. By tensioning the cable, it could be ensured that the fiber optic was kept in place during the casting of the concrete.

3.5.4 Localisation of the fiber optics

To localise the fiber optics and, consequently, the strains, a Kanthal resistance wire was wrapped around the fiber optics at every turn in the helix for both the inner and outer spiral. The wire was pulled out from the form, making it reachable after the concrete had hardened. By connecting the Kanthal wire to a power supply unit, the wire was heated up. Consequently, the wire induced a strain peak along the fiber optics in the output data, at their intersection points. The positions where the Kanthal wire and the fiber optics intersected were documented beforehand, which enabled to later orient the strains to the right position in the concrete specimen.

3.6 Construction

The specimens were constructed at the Structures lab at Chalmers. The spirals for the fiber optics were 3D-printed at the FUSE lab Rapid Prototyping. The construction phase included building the formwork, mounting the anchorage system, assembling the 3D-printed spirals, installing the fiber optics, processing the data, and casting.

3.6.1 Formwork and mounting of anchorage system

The final dimensions established during the design phase were 300x300x450 mm (width, depth, height). The formwork was built using 18mm thick shuttering plywood. The plywood was cut and assembled into a cuboid with the specified dimensions. A 3 mm cut-out was made on the side where the anchor system was mounted to ensure that the anchor head was slightly above the concrete surface, to facilate the load testing. The anchorage system and the metallic rods supporting the 3D spirals were both screwed into this side of the formwork. The metallic rods had a diameter of 5 mm and a length of 430 mm. The rods were designed not to penetrate the entire specimen. The bottom side of the formwork was chosen as the casting side to simplify the casting process. The mould side with the anchor system and metallic rods is shown in Figure 3.11.

Figure 3.11: Mould side where the anchor system and metallic rods were mounted.

3.6.2 Assembly of 3D spirals and mounting of fiber optics

The 3D-printing of the quarters described in chapter 3.5.2 were 3D-printed in Fuse lab Rapid prototyping. Two types of spirals were constructed: one large outer spiral, made for all six specimens, and a small spiral to replicate the helix reinforcement for two specimens. The large outer spiral was formed by stacking the 3D-printed outer quarters, as shown in Figure 3.10a, to create a spiral with 7.75 revolutions. The position of the first revolution was adjusted using nuts to place the underside of the first quarter 25 mm above the bottom mould side. Between the revolutions, a 25 mm tube was stacked to maintain a 25 mm distance. Nuts were screwed on top of the last revolution to keep the spiral intact. The same methodology was applied to the inner spiral, to create a spiral with 4 revolutions, shown in Figure 3.10b. The underside of the first quarter was placed 50 mm above the bottom mould. Between the revolutions, a 20 mm tube was stacked to maintain a 20 mm distance. Figure 3.12a presents the stacking principle and the complete spiral from the side and top views is presented in Figures 3.12b - 3.12c.

(a) Stacking of the first revolution of the inner spiral.

(b) Side-view of the complete inner and outer spirals.

(c) Top-view of the complete inner and outer spirals.

Figure 3.12: The assembly procedure of the 3D-printed spirals.

When the helical reinforcement was installed, the DOFS were attached and kept in position by using cable ties, see figure 3.13.

(a) Attachment of fibre optics on the anchorage reinforcement.

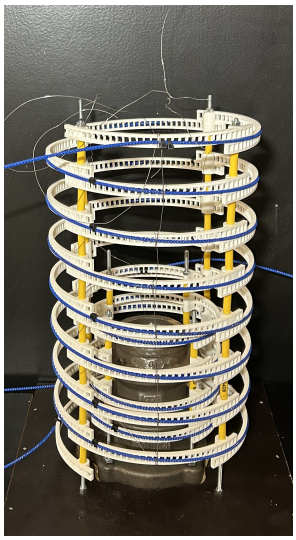

(b) Attachment of the fibre optics on the outer and inner 3D-printed sprial.

Figure 3.13: Attachment of fibre optics on the anchorage reinforcement and 3D-printed spirals.

After the attachment of DOFS, a Kanthal wire were wounded around the DOFS at each revolution. It was done for both the outer and inner spirals, as shown in Figure 3.14, to accurately locate the DOFS position, as described in chapter 3.5.4. A few layers were taped with electrical tape to avoid a short circuit between the Kanthal wire and the anchorage reinforcement, seen in Figure 3.14a.

(a) Winding of Kanthal wire around the anchorage reinforcement.

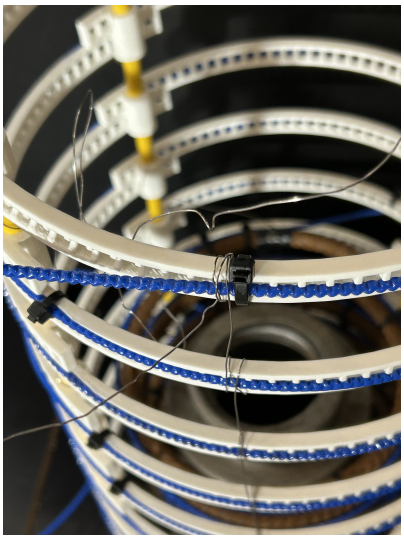

(b) Winding of Kanthal wire around the 3D-printed spirals.

Figure 3.14: Winding of the thread for the fire pinching.

3.6.3 Final design

Two specimens of each configuration were constructed to mitigate the potential sources of error that would comprise the validity of the results. The model rendering and the final design of one specimen of each configuration are presented in Figure 3.15-3.17.

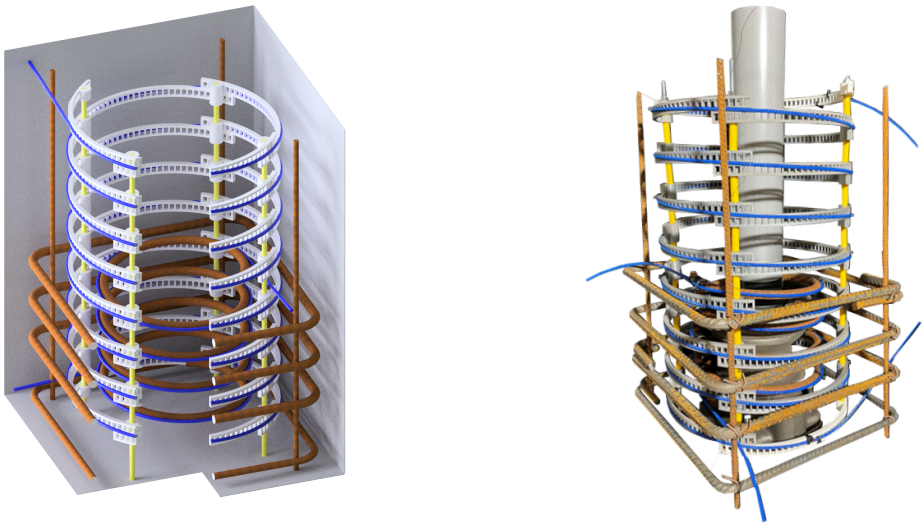

(a) Model rendering **(b)** Final design

Figure 3.15: Comparison between model rendering and final design for reference specimen.

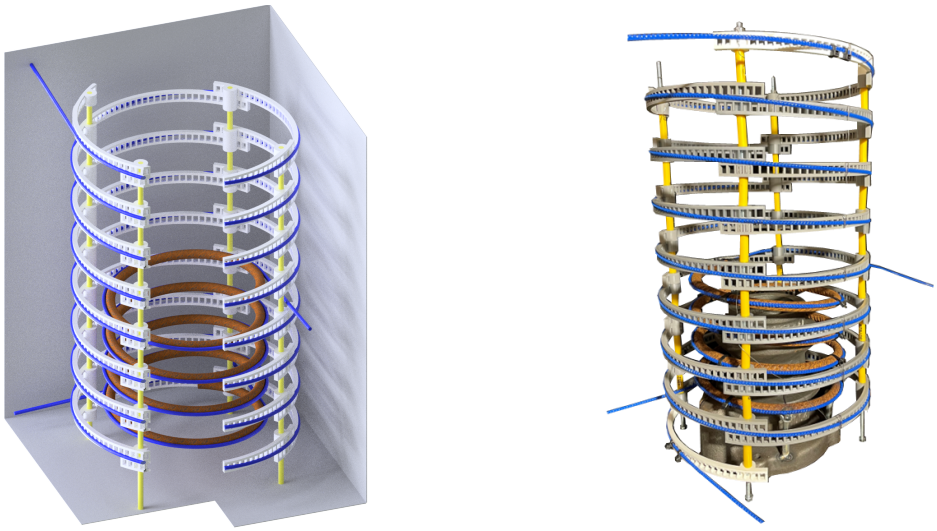

(a) Model rendering **(b)** Final design without duct

Figure 3.16: Comparison between model rendering and final design for SFRC + Helix specimen.

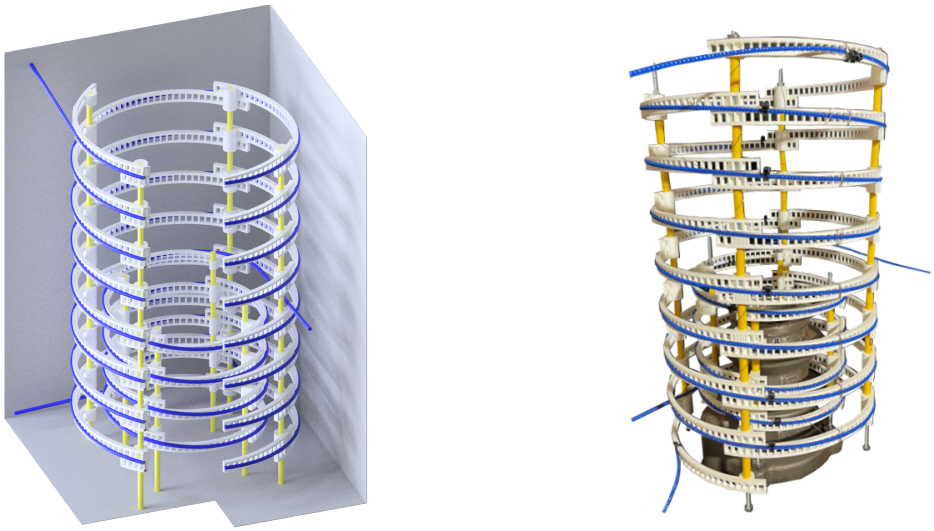

(a) Model rendering **(b)** Final design without duct

Figure 3.17: Comparison between model rendering and final design for SFRC specimen.

3.6.4 Casting of specimens

The specimens were cast with the anchorage system at the bottom mould side to facilitate the casting and enable vibration. A lid was mounted on top of the casted specimen to attain a flat surface after the concrete hardened. However, the lid entrapped air from the casting process, resulting in an uneven bottom surface. This was remedied by casting a thin layer of grout to even out the surface. The surface of one specimen before and after grouting is visualised in Figure 3.18.

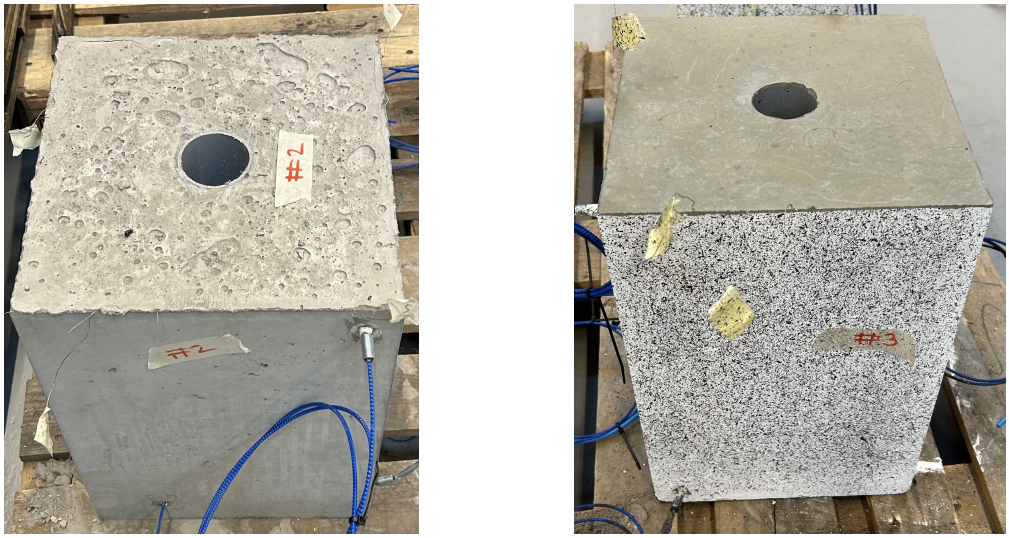

(a) Before grouting **(b)** After grouting

Figure 3.18: Grouting of the uneven bottom surfaces.

3.6.5 DIC surface preparations

It was decided to use Digital Image Correlation (DIC) to monitor strains, deformations, crack patterns, and crack widths on all faces of the specimens during load testing. Therefore, stochastic patterns had to be applied to all faces. The desired stochastic pattern was determined using the ARAMIS app and is based on the monitored surface area of the specimens and the camera setup. The pattern was conducted by first painting the specimens white. After drying, black paint was splashed on the surface using a paintbrush to achieve a stochastic pattern, as Jackson Pollock did in the 1940s-1950s. Several paintbrushes were tested to replicate the desired pattern properly. It was shown that the length, stiffness and amount of straws on the paintbrush influenced the pattern and the amount of water that was mixed into the paint. By adding more water, a more accurate shape and distribution of the black dots were achieved. However, there was a limit regarding the dilution as it caused less contrast in the pattern. A visualisation of the resulting pattern and comparison with the desired pattern is presented in Figure 3.19.

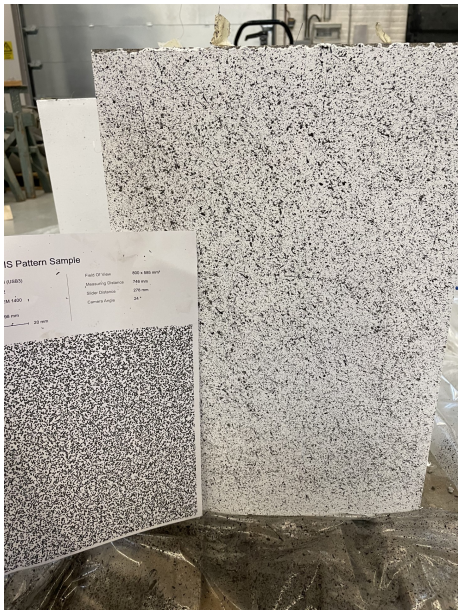

Figure 3.19: Comparison between final stochastic pattern and desired stochastic pattern for DIC monitoring of the surface of the specimens.

4

Experimental testing

4.1 Material testing

The material properties of plain concrete and steel fibre reinforced concrete were determined using the wedge split test method (WST) and the cube test method. The tests were conducted on three specimens of plain concrete and three specimens of fibre reinforced concrete respectively, for each test. The tests were performed 29 days after casting and one day after the centric load test of the specimens. After 7 days of hardening, all specimens were stored in water until the test were conducted. The dimensions of all test specimens were checked against the tolerance levels prescribed in the description of the representative test.

4.1.1 Compressive strength

The compression strength of the materials was determined by performing a cube test in accordance with EN 12390-3 (European Committee for Standardization, 2019). In the test, the specimen is successively loaded to failure, and the maximum compression strength is determined. The tests were conducted in a load frame for compressive strength tests provided by Toni technik, model 2040. The loading rate was set to 0.6 MPa/s. All specimens failed according to what is described in EN 12390-3 (European Committee for Standardization, 2019) as a satisfactory failure. The load setup is presented in Figure 4.1. The obtained results from the cube test are listed in Tables 4.1 and 4.2.

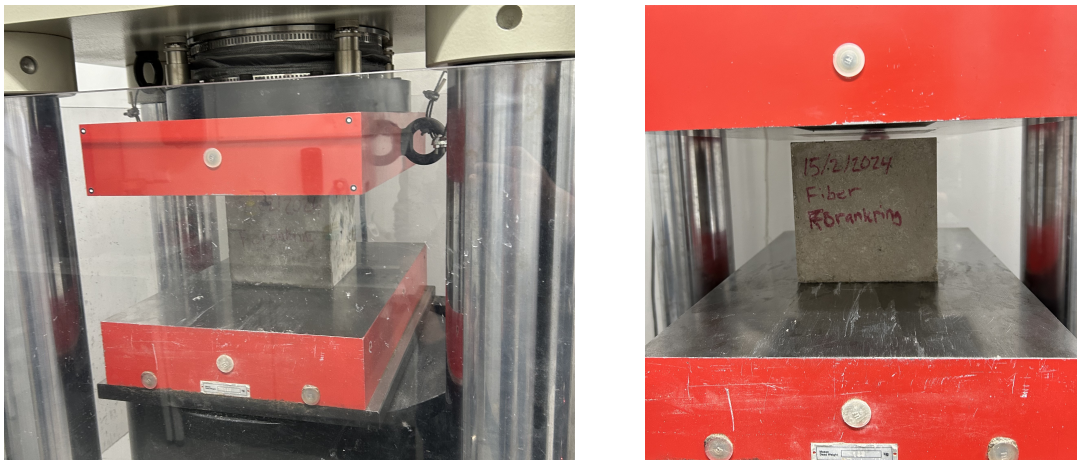

Figure 4.1: Cube test setup.

Table 4.1: Results from cube test for concrete specimens.

Concrete Specimen nr	Density (ρ)	Applied Load (F_m)	Applied stress (σ_m)
1	2.42 g/cm^3	895.32 kN	39.79 MPa
2	2.41 g/cm^3	921.06 kN	40.94 MPa
3	2.42 g/cm^3	911.03 kN	40.49 MPa
Mean value	2.42 g/cm^3	909.14 kN	40.41 MPa

Table 4.2: Results from cube test for SFRC specimens.

SFRC Specimen nr	Density (ρ)	Applied Load (F_m)	Applied stress (σ_m)
1	2.42 g/cm^3	783.35 kN	34.82 MPa
2	2.41 g/cm^3	797.75 kN	35.46 MPa
3	2.42 g/cm^3	789.07 kN	35.07 MPa
Mean value	2.42 g/cm^3	790.09 kN	35.12 MPa

4.1.2 Fracture properties

The fracture properties of the two materials were determined by performing a wedge split test in a test system provided by MTS Systems, model 380.10, according to Wedge Splitting Test Method (NORDTEST, 2005). To perform the tests, the specimens were cast with a groove on top and equipped with a crack-inducing starting notch that was sawn into the specimen after hardening. In the groove, two load devices with roller bearings were placed to pull the specimen apart when the load is applied. The load is applied by a wedge getting pushed down between the roller bearings. During the test procedure, the Crack Mouth Opening Displacement (CMOD) is monitored by a clip gauge placed in the groove, which expands when the load is applied. Additionally, the vertical displacement of the wedge and the applied force were monitored during the test procedure. The test setup is visualised in Figure 4.2.

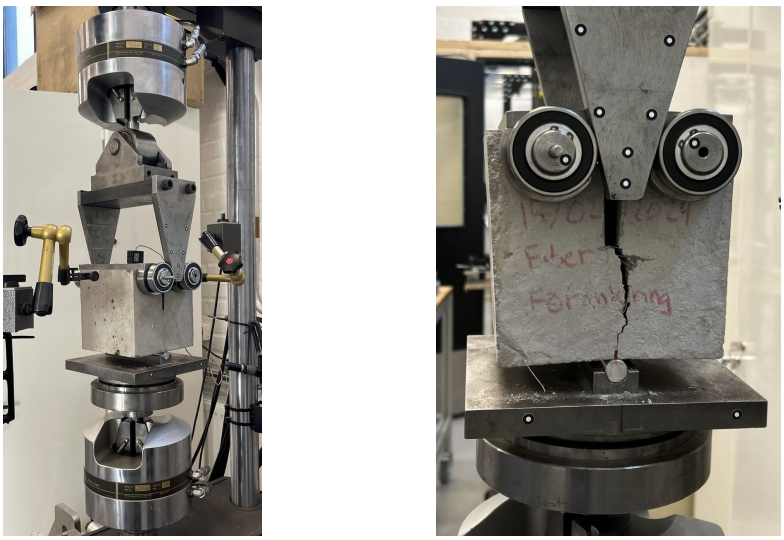

Figure 4.2: Wedge split test setup.

To determine the fracture energy of the materials, the splitting force (F_{sp}) needs to be derived accordingly:

$$F_{sp} = \frac{F_v}{2 \cdot \tan(\alpha)}, \tag{4.1}$$

where $\alpha = 15°$ is the angle of the wedge and F_v is the applied vertical force.

The fracture energy (G_F) was obtained by integrating the splitting force-CMOD curve and dividing by the ligament area. The maximum CMOD that could be obtained from the clip gauge was approximately 4 mm, and for larger CMOD values, the curve was extrapolated based on the vertical displacement of the wedge. Figure 4.3 and 4.4 display the splitting force-CMOD curve for the three specimens of each material.

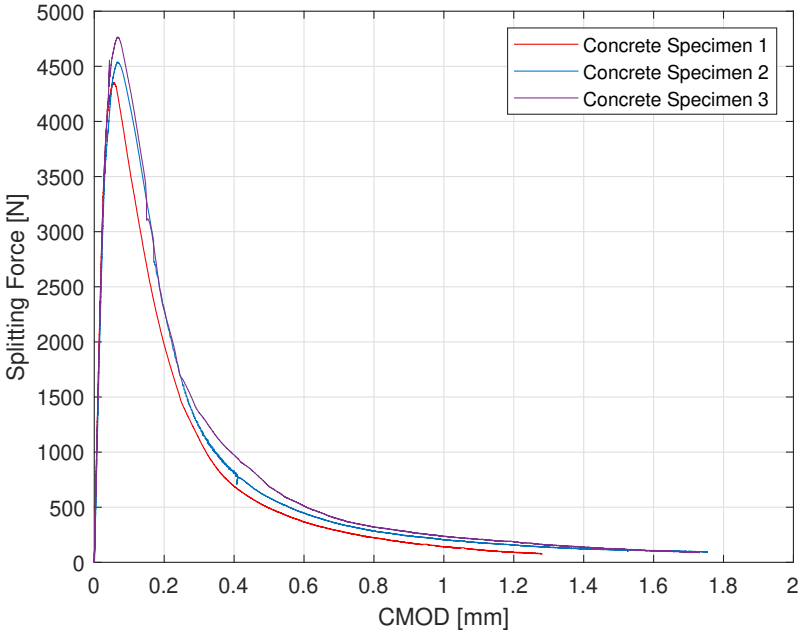

Figure 4.3: Splitting force-CMOD curve for concrete specimens.

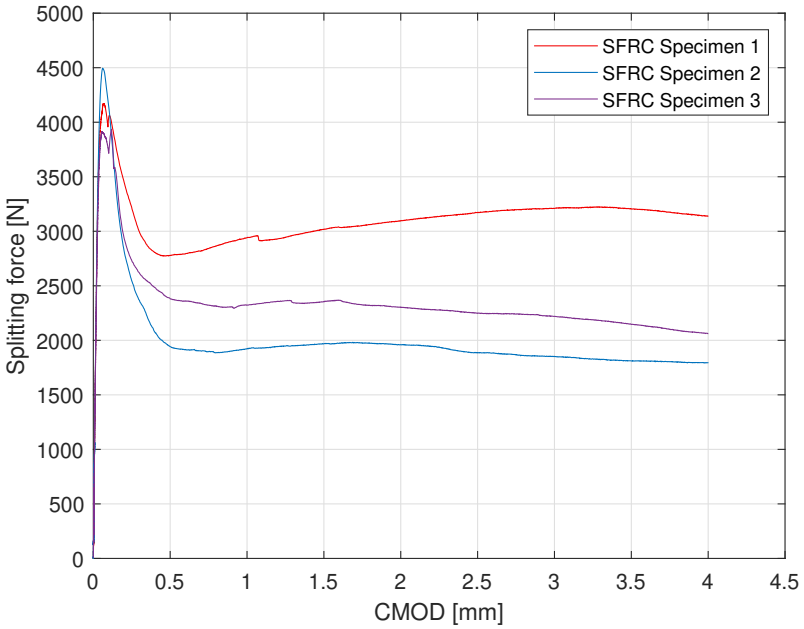

Figure 4.4: Splitting force-CMOD curve for SFRC specimens.

The tensile strength of the materials is obtained by analysing the peak splitting force. At the peak, the concrete cracks, and it can be assumed that the cross-section is fully activated and has a linear strain distribution just before the peak value. The tensile strength can then be obtained by moment equilibrium and contribution from the splitting force of the uncracked cross-section. Tables 4.3 and 4.4 list the fracture energy and tensile strength for each specimen and material.

Table 4.3: Results from WST for concrete specimens.

Concrete specimen nr	Fracture Energy (G_f)	Tensile Strength
1	95.89 Nm/m^2	3.53 MPa
2	114.75 Nm/m^2	3.68 MPa
3	123.02 Nm/m^2	3.86 MPa
Mean value	111.22 Nm/m^2	3.69 MPa

Table 4.4: Results from WST for SFRC specimens.

SFRC specimen nr	Fracture Energy (G_f)	Tensile Strength
1	6464.95 Nm/m^2	3.38 MPa
2	3746.08 Nm/m^2	3.62 MPa
3	4235.05 Nm/m^2	3.21 MPa
Mean value	4815.36 Nm/m^2	3.40 MPa

The stress-strain relationship for SFRC was obtained by first interpolating the splitting force-CMOD curves from the material testing. It was assumed that the compression height was constant and equal to one tenth of the alignment height. Additionally, it was assumed that the outer edge was subjected to stress equal to the compression strength. From horizontal equilibrium, the splitting stress can be derived. Until cracking, the material has a linear response, which could be derived using the modulus of elasticity obtained from the cube test. After cracking, the strain values depend on the chosen crack bandwidth, which was chosen to equal the element size, as described in Chapter 3.4.3. Figure 4.5 presents the resulting stress-strain relationship.

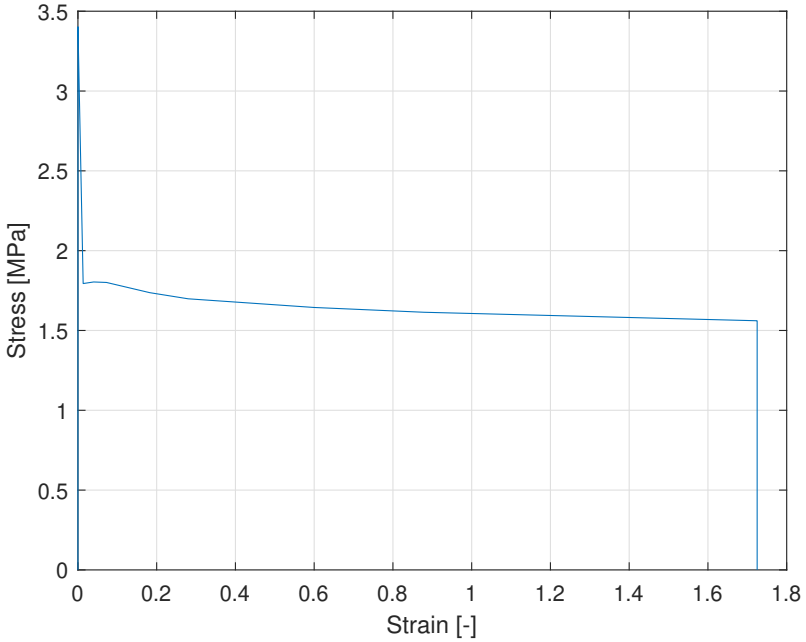

Figure 4.5: Stress-strain relationship for SFRC obtained from WST.

4.2 Concentric load testing

The concentric load testing of the specimens was conducted in a hydraulic machine equipped with a load cell of 1 MN provided by MFL Prüf- und Meßsysteme. The load was applied on the tendon head through a spherical bearing to obtain an even pressure distribution from the pressure plate. A plain contact area at the bottom was achieved by undercasting with a fast setting cement called Quik-rok in the test machine. The specimens were placed centrally in the test machine using laser devices. The deformation rate of the machine was set to 0.2 mm/min to capture the desirable structural behaviour of the specimens. The load and the axial displacement at the anchor head were recorded with a sampling rate of 10 Hz. The concentric load setup and positioning of the specimens are visualised in Figure 4.6.

Figure 4.6: Concentric load setup and positioning of specimen.

The fiber interrogator ODisI 6800 with 8 optical fiber channels, manufactured by LUNA, was used to collect strain data during the test. Before the loading procedure, the optical fibers were tared to remove strain measurements induced during the construction. The measurement rate of the fiber optics was set to 25 Hz for both the inner and outer spiral. The gauge pitch was set to 5.2 mm to obtain sufficient spatial resolution. The strain outputs were measured at the same locations along the fiber in every measurement. Figure 4.7 shows the strain data obtained from the optical fiber in the outer spiral of Specimen 6 at a load of 950 kN. The figure also shows how the raw strain data was refined for the analysis, by smoothing the data. The data was refined to minimise local disturbance and optimise data storage. It was done by adjusting outliers and replacing missing values.

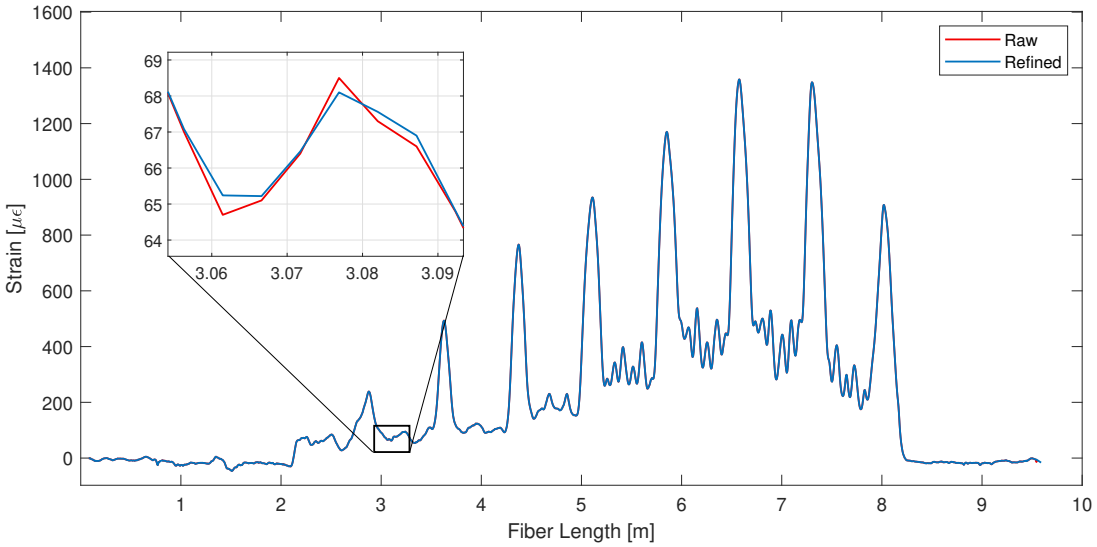

Figure 4.7: The strain data obtained from the optical fiber from the outer spiral in Specimen 6 at a load of 950 kN. The plot shows the raw data obtained and how it was refined for the analysis.

Four DIC cameras of type CMOS (2448x2048 pixels) were placed perpendicularly at a fixed distance of 0.85 m in front of the specimens' surfaces. The setup yielded a field of view of approximately 350 x 420 mm^2. White LED light panels illuminated the surfaces to obtain a high contrast in the speckle pattern. The connecting fiber optics cables were arranged to minimise shading the most interesting areas of the surfaces. An image rate of 0.5 Hz was chosen during the load testing. The DIC images from the load testing were post-processed in the Software GOM Correlate to obtain strain fields and crack widths on the surfaces of the specimens.

5

Results and observations

In the following chapter, the experimental testing results of the specimens will be presented. The experimental testing results consist of load-deformation relation, strain data from the optical fibres, and DIC data. In order to differentiate between the various specimens, the specimens have been assigned numbers based on Table 5.1. To facilitate the presentation of results and analyses, only the results Specimen 1, 4 and 5 are presented in the following. The specimen with the lowest maximum strain of each configuration was selected to avoid outliers. The results for Specimen 2, 3 and 6 are presented in Appendix A - H. The faces of the specimen and the revolutions of the spirals are presented in Figure 5.1, serving as the visual reference for the presentation of the results.

Table 5.1: The numbering of the specimens and the corresponding configuration.

Specimen No.	Configuration
1-2	Reference
3-4	SFRC + Helix
5-6	SFRC

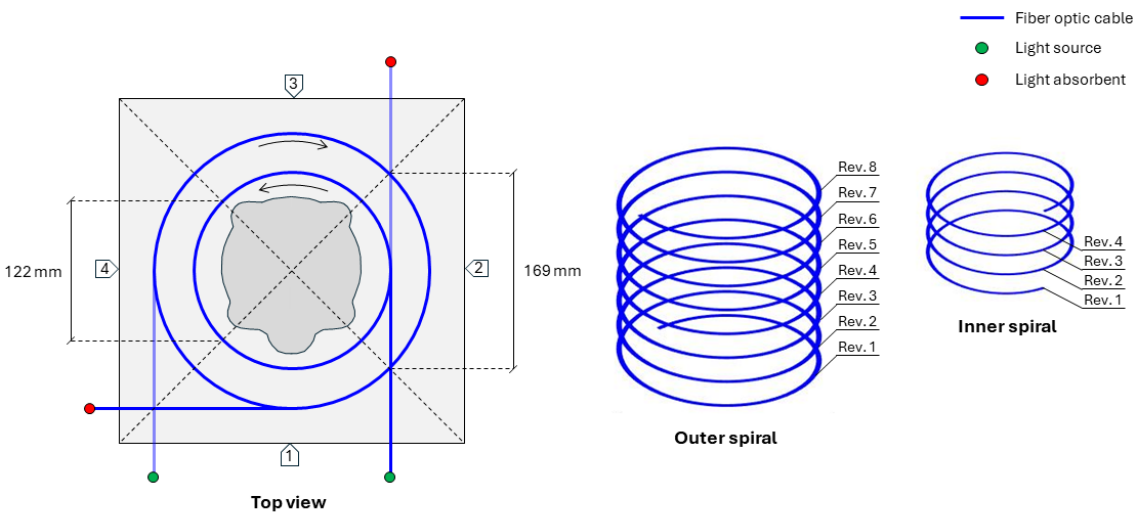

Figure 5.1: Arrangement of distributed fiber optics.

5.1 Load displacement curves

In the experimental testing, a load-displacement curve was obtained for all specimens and is presented in Figure 5.2. Analysing Figure 5.2, all load-displacement curves have a slight inclination increase with loading until 200 kN, which remains constant thereafter. The reason could be that the concrete becomes compacted under loading, closing pores and fixing aggregates in position, thus increasing the specimen's stiffness. Studying Figure 5.2, it becomes evident that Specimens 1,2,4 and 6 showed a similar response during loading. The load-displacement curves of these specimens have similar gradients and reached a maximum displacement of 3.1-3.3 mm at a load of 955 kN. The similar gradient of the load-displacement curves indicates that the specimens possess similar stiffness. The load-displacement curves of these specimens do not exhibit any significant change in slope, which may indicate that the concrete does not undergo global softening or hardening response.

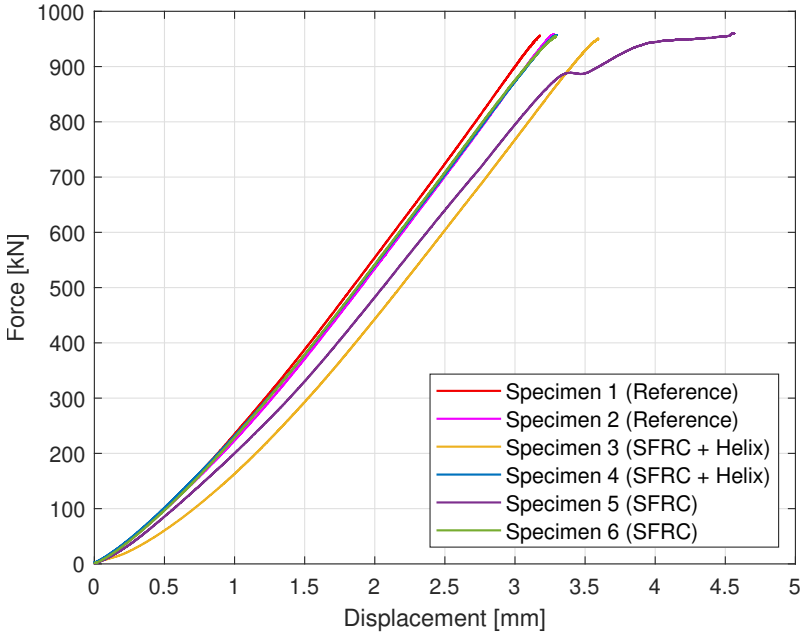

Figure 5.2: Load-displacement curve obtained from the concentric load testing.

The load-displacement curve of Specimen 3 exhibits a similar response as the previously mentioned specimens. Compared to the other specimens, Specimen 3 had a lower stiffness because it had a less steep gradient in the beginning. However, after a load of 400 kN, the slope became parallel to Specimen 1, 2, 4, and 6 curves, indicating similar stiffness. Due to the lower stiffness initially, the maximum displacement became larger, reaching 3.6 mm at 950 kN. The stiffness difference between Specimen 3 and the other specimens may be due to the early formation of cracks in Specimen 3. As the other specimens formed cracks, the difference in stiffness was equalised. There was no significant change in the slope of Specimen 3's load-displacement curve, which may indicate that the concrete does not undergo strain-softening or strain-hardening during loading.

Specimen 5 has the largest displacement among the specimens, with a maximum of 4.6 mm at 960 kN. The load-displacement curve of Specimen 5 shows a significantly different response than the other specimens. At a force of 888 kN, the specimen undergoes global softening, resulting in a noticeable stiffness decrease due to the less steep slope. The global softening could be due to one or multiple cracks being formed or further opened. At this point, fibres start to transfer tensile stresses over these cracks and can begin to pull out. The post-peak behaviour of the SFRC was expected to be strain-softening rather than strain-hardening since the volume fraction of fibres was low to moderate.

The NLFEA analysis conducted in the design phases was repeated using the material data obtained from the material tests, as described in Chapter 4.1. Figure 5.3 presents the load-displacement curves obtained from NLFEA and the concentric load testing. Comparing the load-displacement curves indicates that the NLFEA models exhibit significantly greater stiffness than the specimens, indicating the steep curve. The NLFEA models and the specimens are similar in that all configurations demonstrated similar elastic stiffness within each category. However, the NLFEA models tend to form cracks at lower loads, around 600-800 kN, compared to the specimens. The post-crack response is more pronounced in the NLFEA models, characterized by a noticeable change in slope in the load-displacement curves. Due to limitations in the load-testing facilities, the investigation of the post-crack response was constrained. However, in Specimen 5, a global softening response is evident, causing a more rapid change in slope compared to the NLFEA, where the slope inclination decreases more gradually.

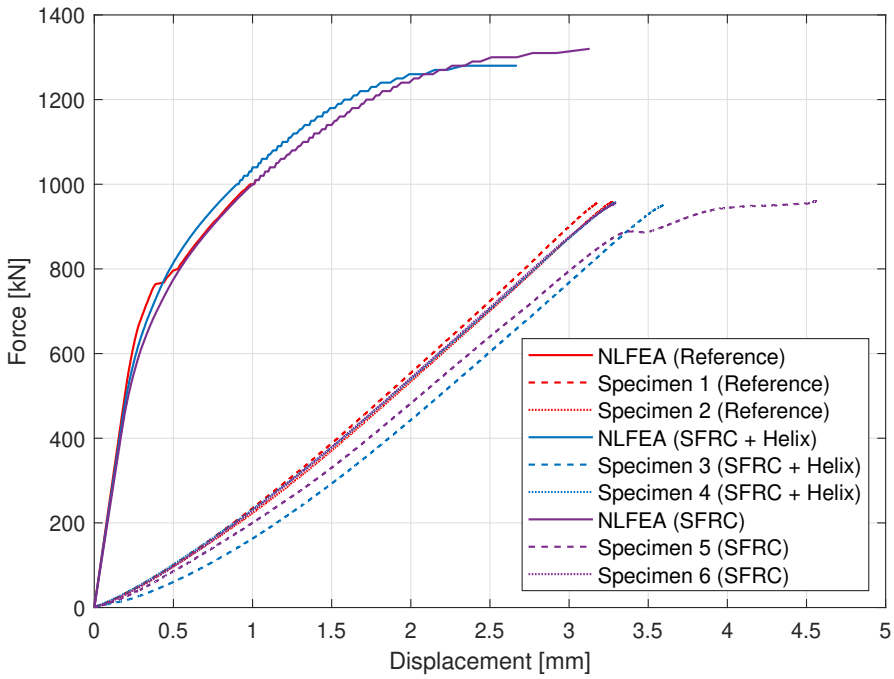

Figure 5.3: The load-displacement curves obtained from NLFEA and the concentric load testing.

5.2 Postprocessing of DOFS measurements for visualisation of strain distribution

The DOFS measured strain during the loading for all specimens in the two different spirals. Figures 5.4 - 5.6 present the geometry of DOFS visuilaised within the Specimen 1, 4, and 5. The numbers 1-4 in Figure 5.4 - 5.6 refer to the faces depicted in Figure 5.1. Figures 5.4 - 5.6 shows the strain distribution obtained by DOFS at a load of 950 kN for Specimen 2, 3, and 6.

Upon studying Figures 5.4 - 5.6, it is apparent that the maximum strains of the inner spirals and outer spirals are localised in the centre of a face. Moreover, it is pronounced that the maximum strains of the outer spiral are distributed at revolution 5-7. In comparison, the maximum strains for the inner spiral are distributed over all revolutions. However, revolutions 1-4 of the inner spiral are located at the same height range as revolutions 5-7 of the outer spiral.

The maximum strain of Specimen 1 are localised to the centre of face 1, see Figure 5.4. The larger strains of the outer spiral are more localized at the centre of face 1 than the larger strains of the inner spiral. The larger strains of the inner spiral are distributed more uniformly, with larger strains at the centre and corners of the specimen.

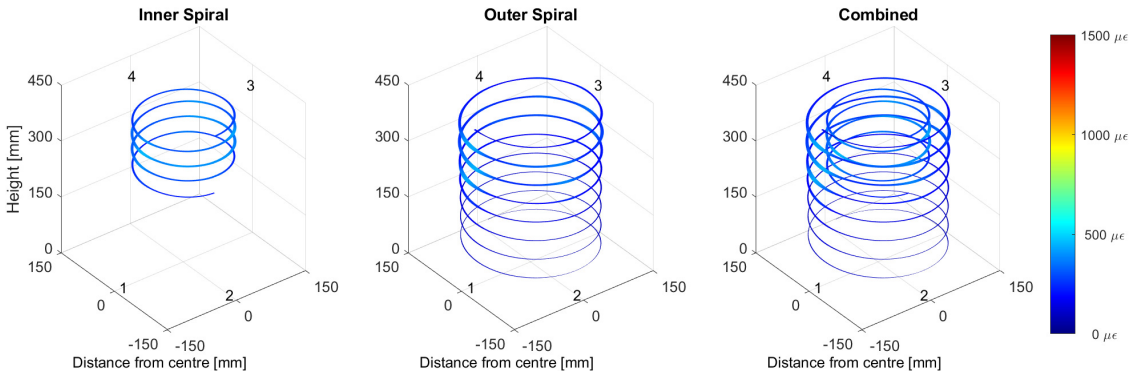

Figure 5.4: Strain distribution at 950 kN obtained by DOFS located at the inner and outer spiral of Specimen 1 (Reference).

The maximum strains of Specimen 4 are localised to the centre of face 2 and 4 for both the inner and outer spiral, see Figure 5.5. The symmetry of the specimen could be the reason for the similar strain localisation and magnitude of faces 2 and 4. The strain localisation of Specimen 4 is more significant than that in Specimen 1. The difference in strains between the centre of the face and at the corners considerable larger in Specimen 4. Additionally, the strains of the inner spiral are less evenly distributed in Specimen 4 compared to Specimen 1.

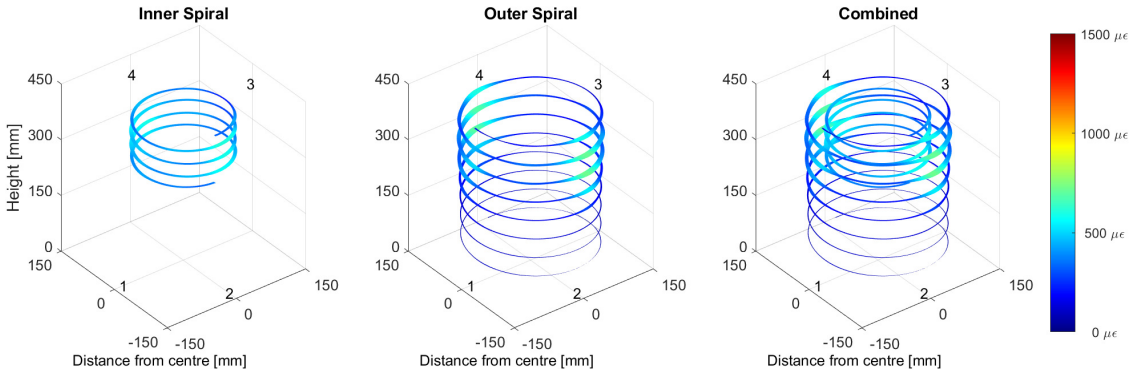

Figure 5.5: Strain distribution at 950 kN obtained by DOFS located at the inner and outer spiral of Specimen 4 (SFRC + Helix).

The largest strains of the inner and outer spiral are localised to the centre of Face 1 for Specimen 5, see Figure 5.6. The difference in average strain between the inner and outer spirals is more significant in Specimen 5 than in Specimen 1 and 4. Additionally, smaller areas of high strain, such as in the corner between Faces 3 and 4, can be observed compared to the outer spiral. No such difference in localisation is observed for Specimens 1 and 5.

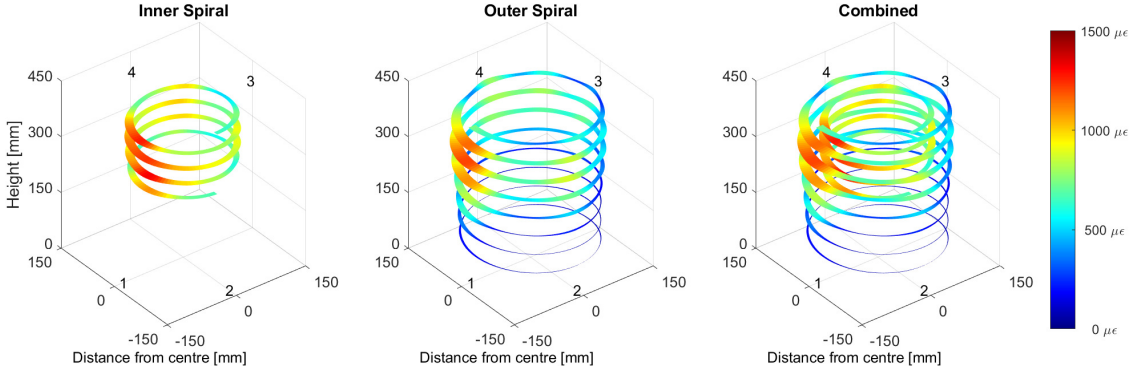

Figure 5.6: Strain distribution at 950 kN obtained by DOFS located at the inner and outer spiral of Specimen 5 (SFRC).

5.3 DOFS measurements for evaluation of strain development and localisation

The development of strain profiles throughout the load testing, measured by the DOFS located at both the inner and outer spiral, are presented in Figures 5.7 to 5.12. The strain profiles are presented along the fiber length and height in the specimen, and are divided into faces and revolutions of the inner and outer spiral, as described in Figure 5.1. Upon analysis of the strain profiles along the height of the specimens, it can be observed that the largest strains occur between revolutions 5 and 7, corresponding to a height range of approximately 225 mm to 375 mm. It can also be observed that the SFRC configuration has larger strains and more distinct

localisation further down the specimen compared to the other two configurations. The most condensed distribution of strains occurs in the reference case, where a significant lowering of strains occurs at a height of approximately 225 mm. For the SFRC + Helix configuration, this shift occurs slightly lower whereas for the plain SFRC, strain localisations can be observed along the entire height.

It is also possible to distinguish that strain localisation occurs at a load of approximately 500 kN, which is typically pronounced at Face 1 for Specimen 1 and 5 and Faces 2 and 4 for Specimen 4. From this load, the overall strain, as well as the strain peaks, successively increases with the increasing load. The most significant strain increase occurs at the load of 950 kN.

The strain profile of Specimen 1's outer spiral exhibits a concentration of strains at the middle of the faces, see Figure 5.7. In contrast, the strain profiles are less pronounced in the middle of the face of the inner spiral, see Figure 5.8. Instead, strain peaks vary in localisation in the specimen, except for Face 1, where peaks can be identified centrally for all revolutions. The maximum strain for Specimen 1 at 950 kN is 446 µϵ and 458 µϵ for the outer and inner spiral, respectively.

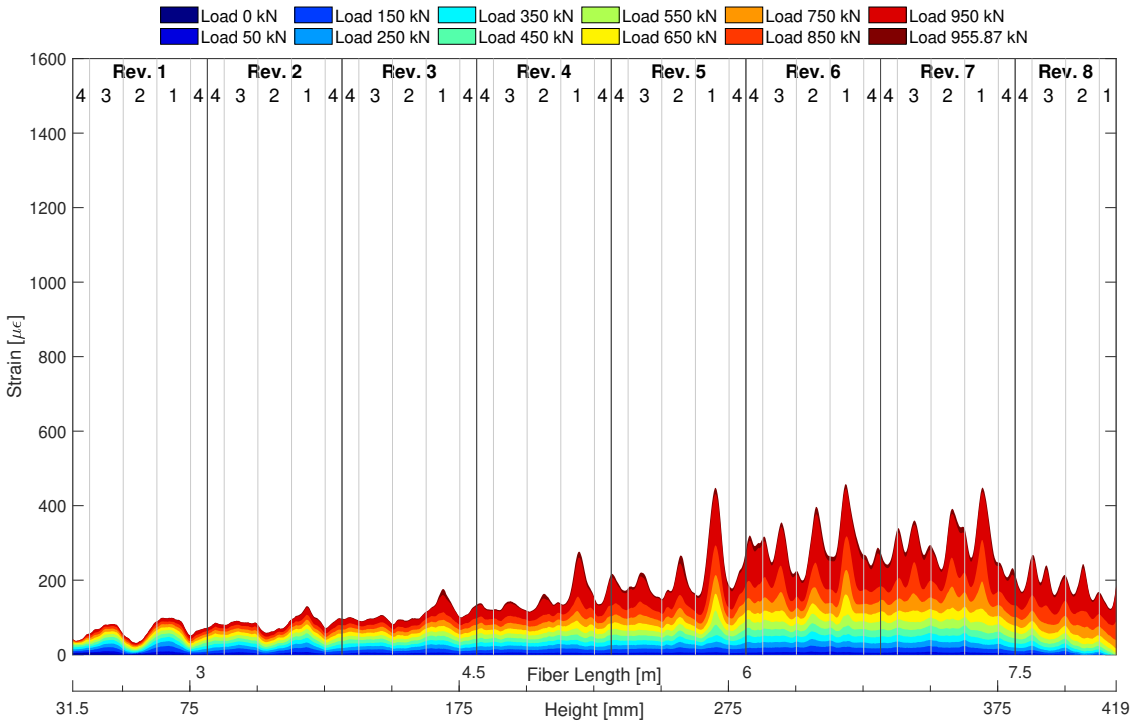

Figure 5.7: Strain profiles for different load steps obtained by DOFS located at the outer spiral of Specimen 1 (Reference).

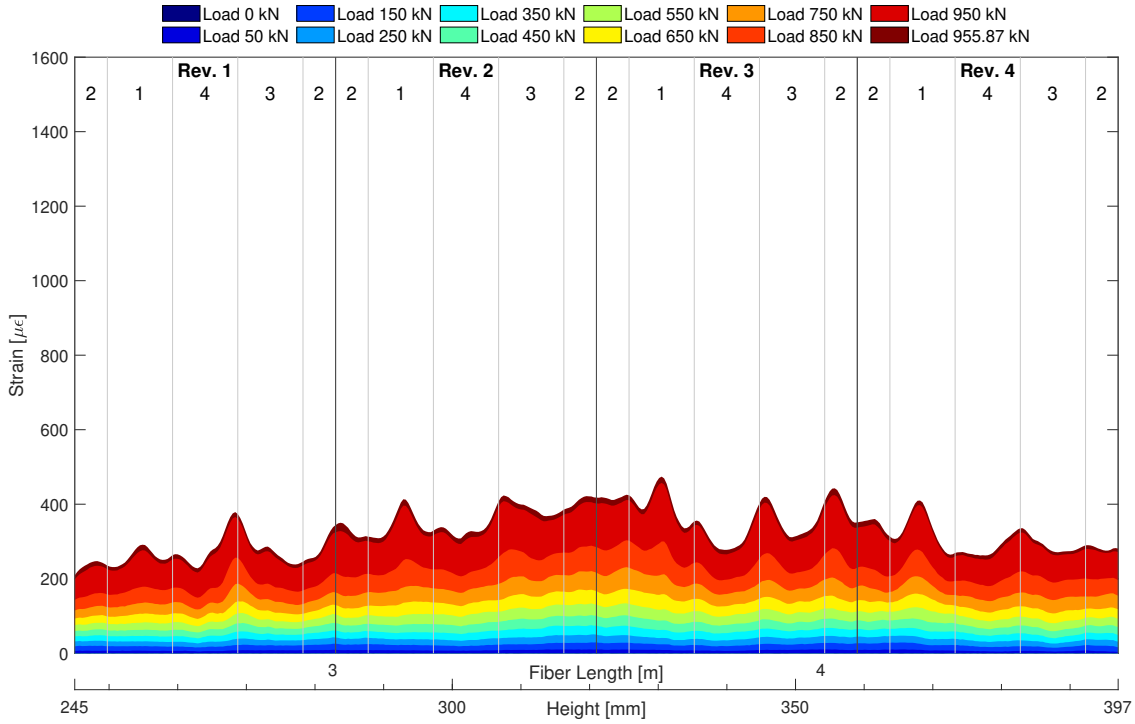

Figure 5.8: Strain profiles for different load steps obtained by DOFS located at the inner spiral of Specimen 1 (Reference).

In the case of Specimen 4, the highest strains for both the inner and outer spirals are localised to Faces 2 and 4, see Figure 5.9 and 5.10. Upon analysing the strain profile for the outer spiral, it is evident that the localisation of strain has a distinct orientation towards the middle of the faces. As for the inner spiral, there are instances of localised strain towards the middle of the surfaces, although some exceptions exist where strain peaks are oriented slightly shifted towards the corners. The maximum strain for Specimen 4 at 950 kN amounts to 722 µϵ and 611 µϵ for the outer and inner spiral, respectively.

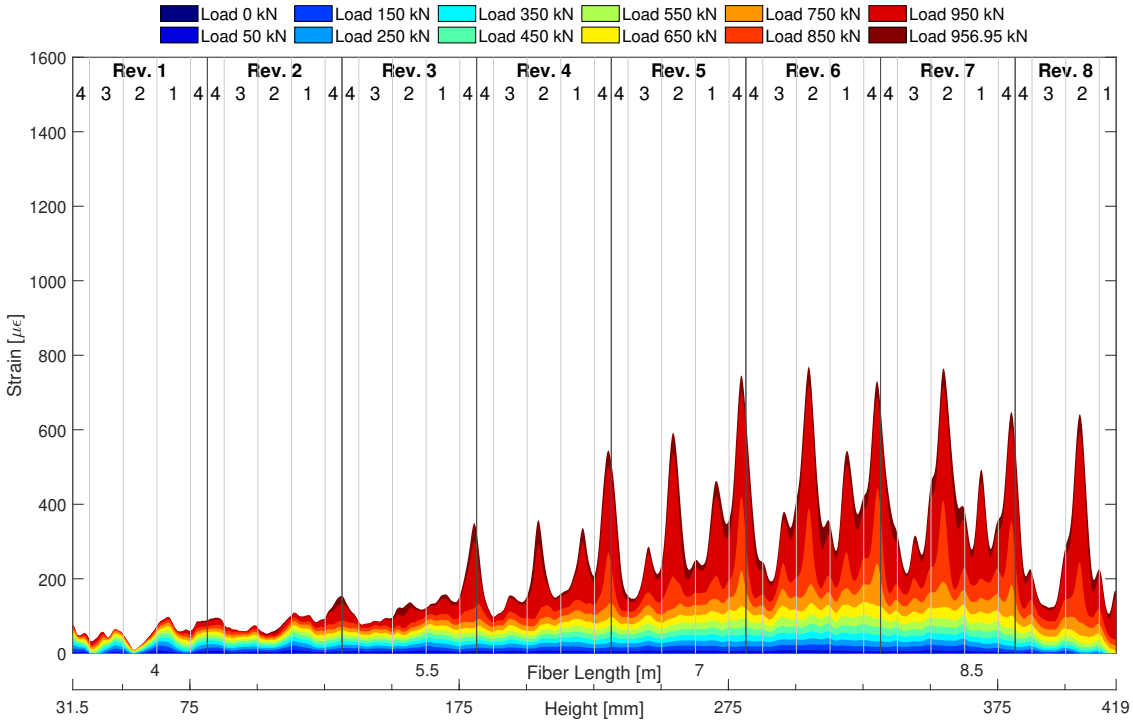

Figure 5.9: Strain profiles for different load steps obtained by DOFS located at the outer spiral of Specimen 4 (SFRC + Helix).

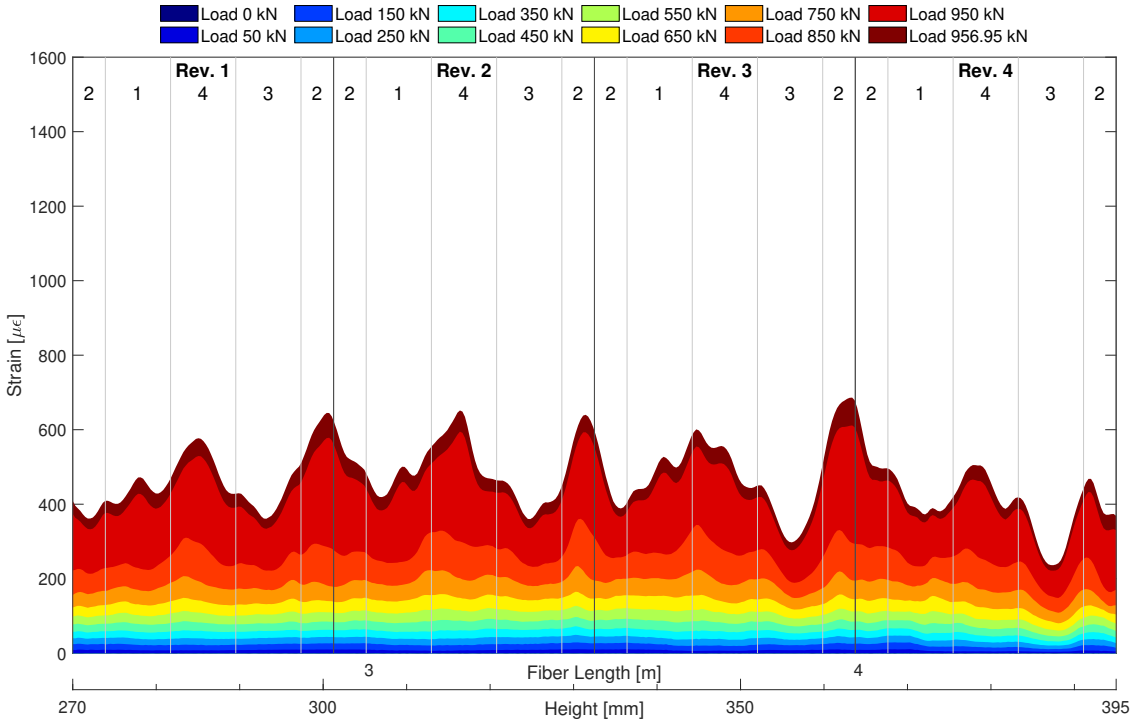

Figure 5.10: Strain profiles for different load steps obtained by DOFS located at the inner spiral of Specimen 4 (SFRC + Helix).

Regarding specimen 5, it is possible to distinguish centrally located strain peaks in most of the faces, see Figure 5.11. As for Specimen 4, some shifts of strain localisation is present for some revolutions in the inner spiral, see Figure 5.12. The maximum strain peak is significant over Face 1 for both the inner and outer spiral. The maximum strain for Specimen 5 at 950 kN amounts to 1211 µϵ and 1319 µϵ for the outer and inner spiral, respectively.

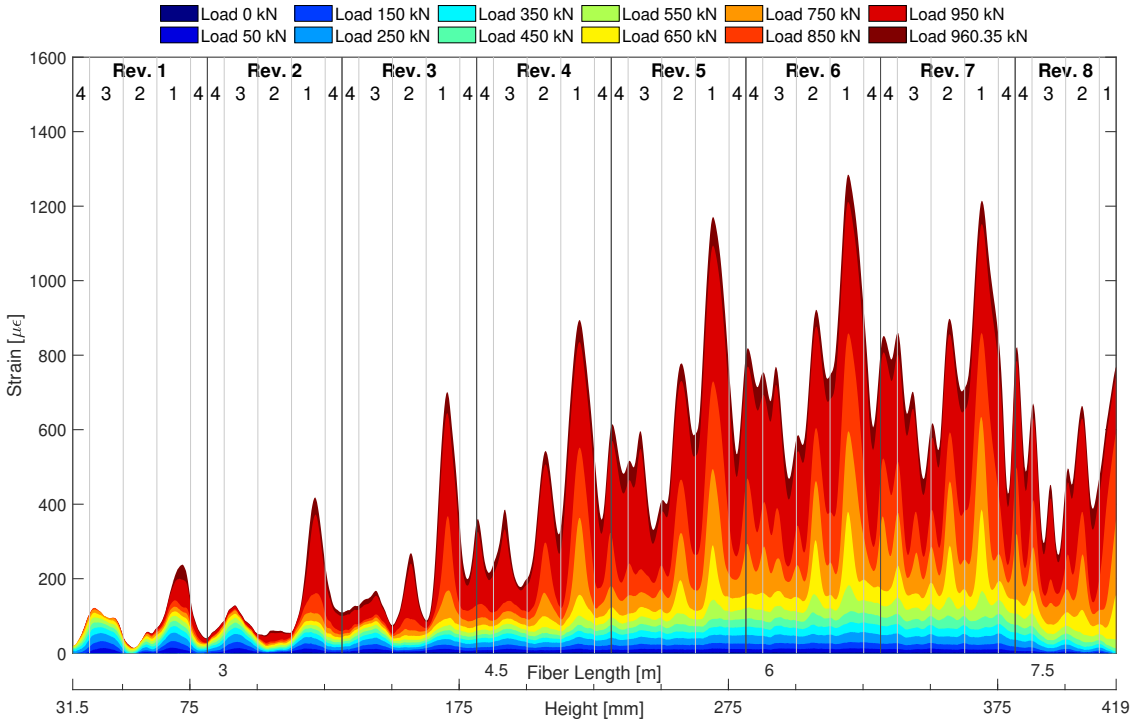

Figure 5.11: Strain profiles for different load steps obtained by DOFS located at the outer spiral of Specimen 5 (SFRC).

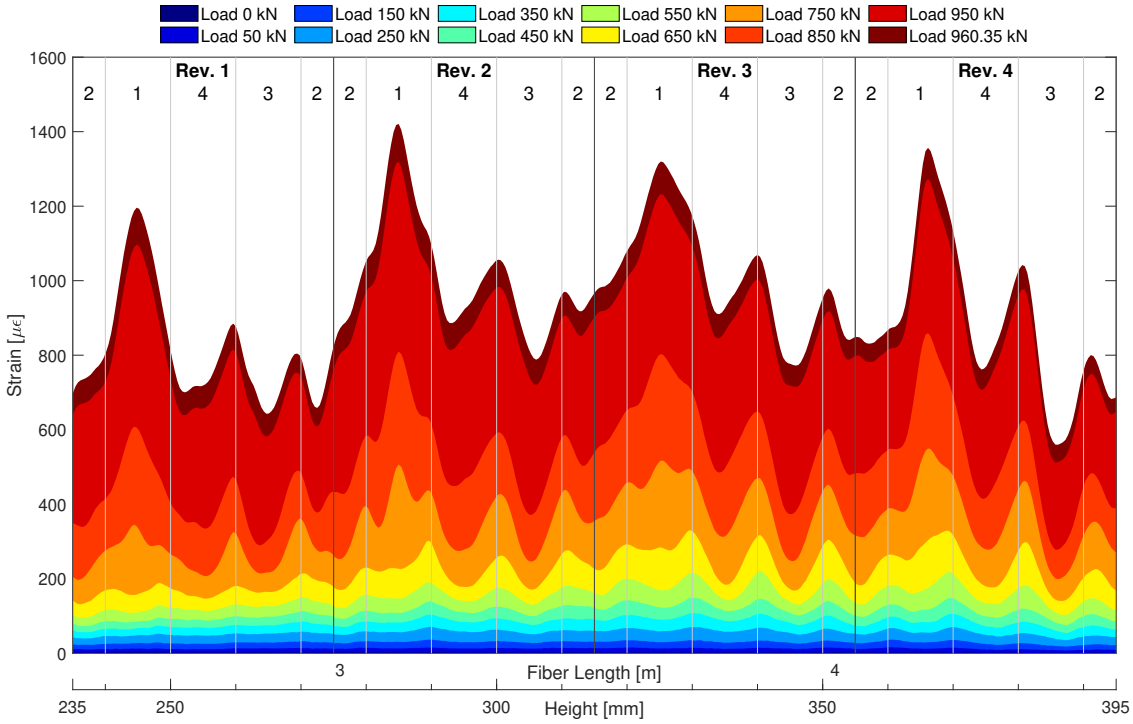

Figure 5.12: Strain profiles for different load steps obtained by DOFS located at the inner spiral of Specimen 5 (SFRC).

In the specimen containing only SFRC, the highest strain values are concentrated in the inner spiral, unlike in the configurations with helix reinforcement. The addition of helix reinforcement results in a more even strain distribution with slightly larger values oriented towards the surface. Notably, the specimen made of only SFRC has significantly larger strains than the other two configurations, both in terms of peak values and overall strain distribution. Out of the three specimens, the reference configuration has the smallest strains.

5.4 Comparison between DOFS measurements and DIC strain field

During the load testing, 2D-DIC was used to monitor all four faces of each specimen, as well as DOFS measuring along the spirals. The development of strain profiles of each face of the specimens are presented in Figures 5.13, 5.15 and 5.17. The measurements are obtained from the DOFS located in the outer spiral. The top graphs are the same as presented in Chapter 5.3 and the bottom plots display the strains projected on to the distance specified in Figure 5.1 for each face of the specimens. Figures 5.13, 5.15 and 5.17 present the strain profile projected on each face of the specimen, along with the DIC measurements for a load of 950 kN.

By analysing the strain profiles along the height of the specimens, similar observations can be made as presented in Chapter 5.3. The plain SFRC specimen develops higher strains for a larger part of its height than the other configurations. It can also be verified that the strain localises centric for most specimens' faces. Some noticeable shift is observed in Figure 5.17 (Face 1) and 5.17 (Face 1 and 3), where the projected strains are oriented centrally at the upper part of the specimen and propagate towards the corners further down.

Studying Figure 5.14, the most pronounce strain localisation is present within a height span of approximately 225 mm to 375 mm, which matches very well the range of which visible cracks develops at the surface. The highest strains on the surface is present at a height of 300 mm, along with the peak strain values measured by the DOFS. Apart from Face 4, all surfaces develops a centrally located crack, following the path of the peak strain measured by the DOFS.

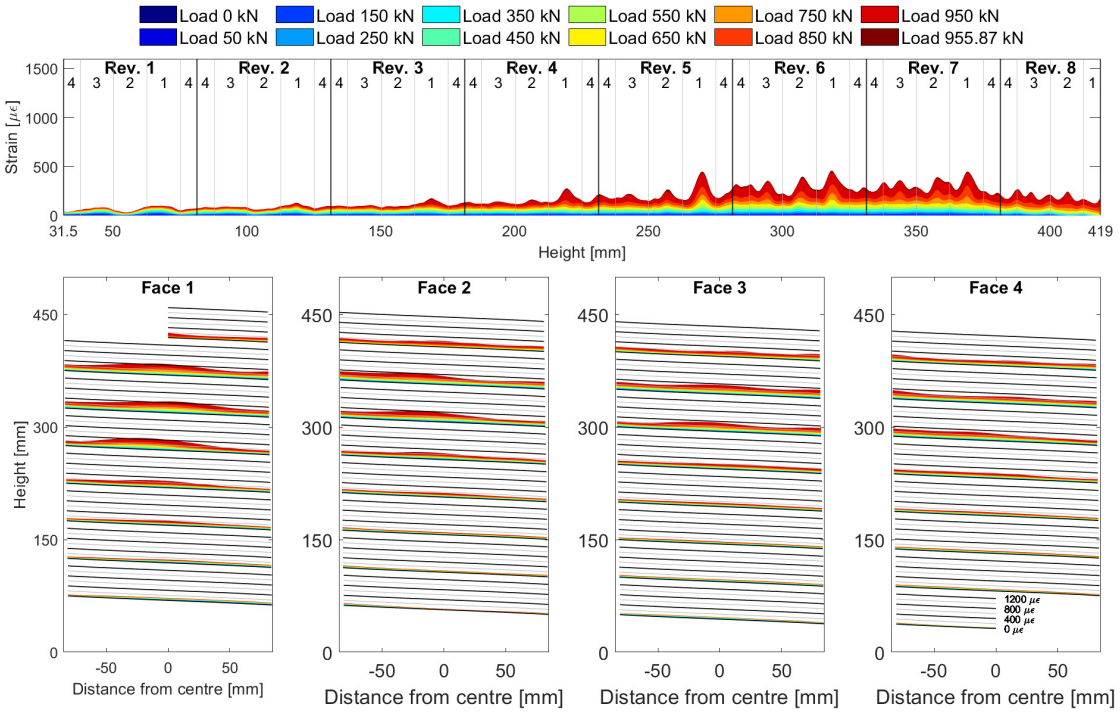

Figure 5.13: Strain profiles for different load steps obtained by DOFS located at the outer spiral of Specimen 1 (Reference). The bottom plots display the projected strain profiles on each face of the specimen.

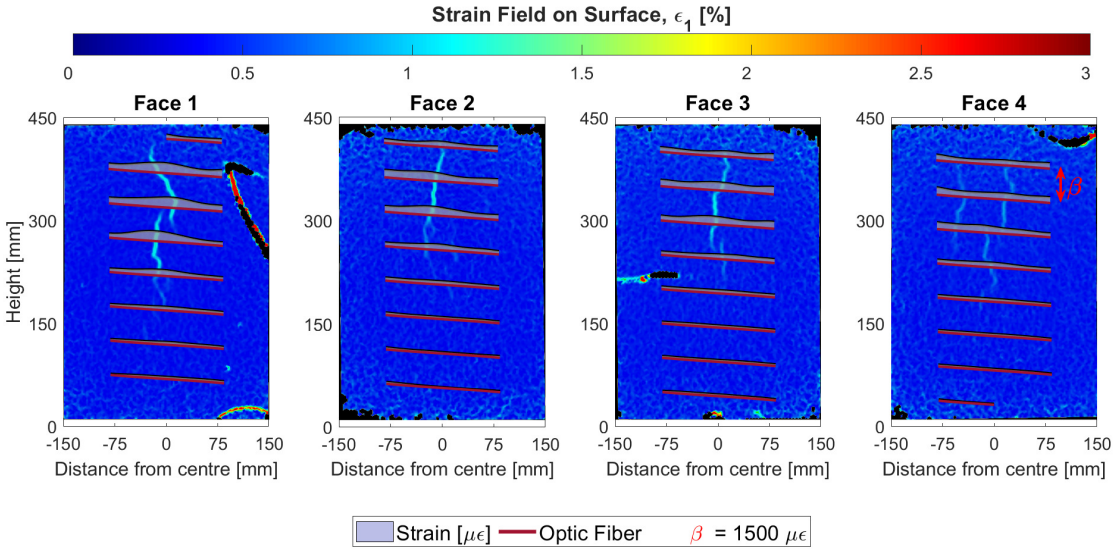

Figure 5.14: Surface strain fields measured with DIC compared with DOFS measured strains at 950 kN for Specimen 1 (Reference).

Studying Figure 5.16, the most pronounce strain localisation is present from a height of approximately 175 mm to the highest measuring point on Face 2 of 410 mm. Studying the range of crack development it agrees very well with the range of strain localisation obtained from the DOFS. Similar as for Specimen 1, the highest strains

on the surface is present at a height of 300 mm, along with the peak strain values measured by the DOFS. The most pronounce cracks develop at Face 2 and 4, where the latter one is centrally located. Face 1 develops cracks starting at an height of 300 mm and and propagates slightly shifted to the corner at a height of 175 mm, similarly as for Face 2. The cracks developed on Face 3 are the least pronounced.

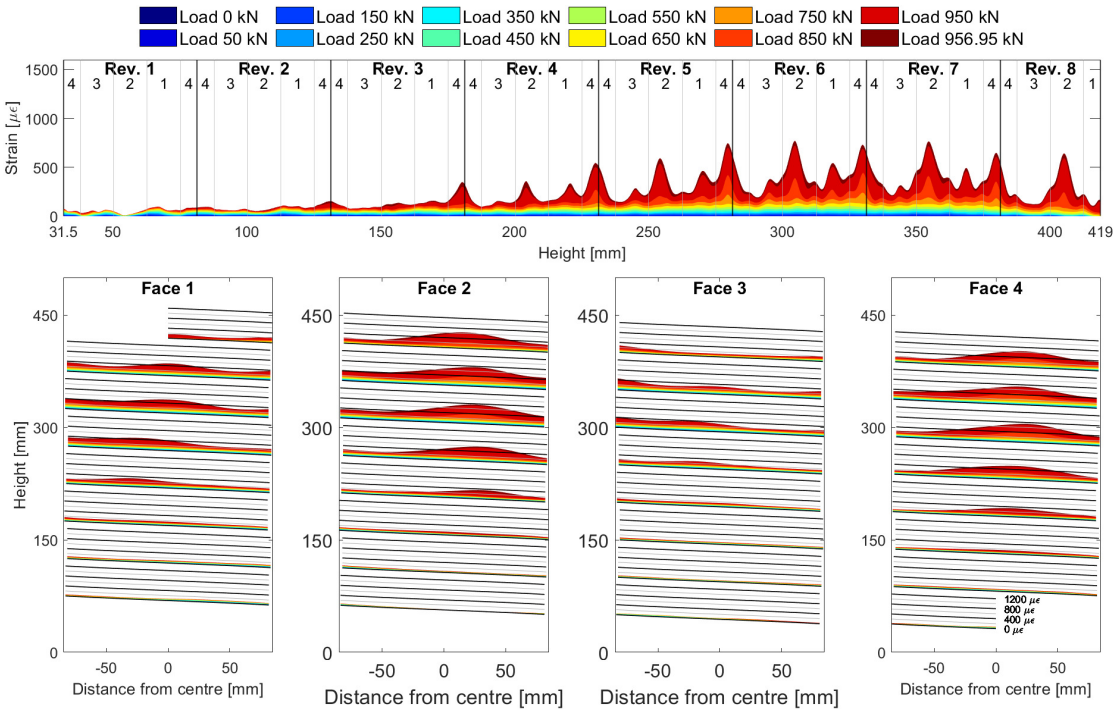

Figure 5.15: Strain profiles for different load steps obtained by DOFS located at the outer spiral of Specimen 4 (SFRC + Helix). The bottom plots display the projected strain profiles on each face of the specimen.

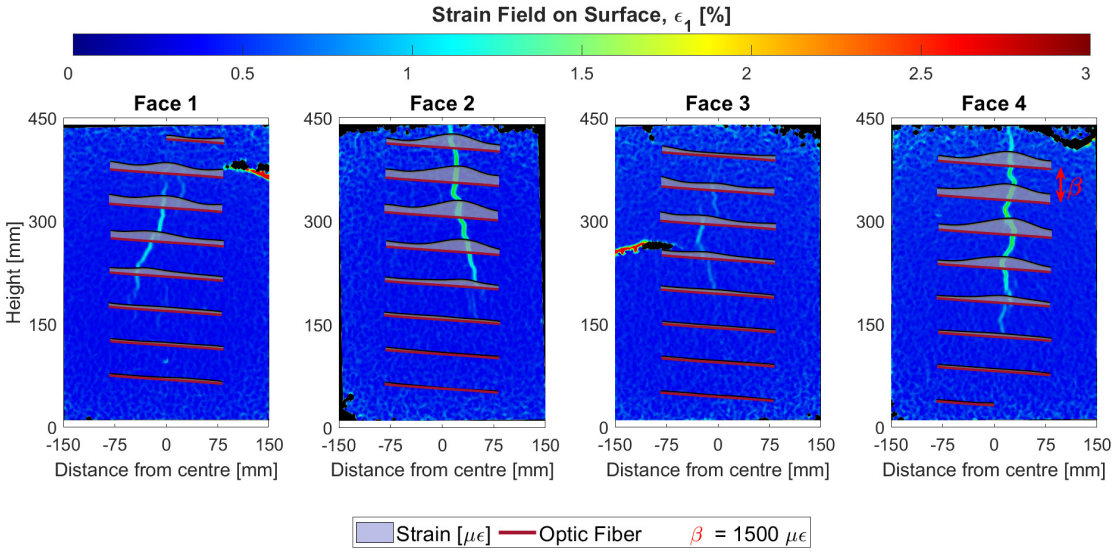

Figure 5.16: Surface strain fields measured with DIC compared with DOFS measured strains at 950 kN for Specimen 4 (SFRC + Helix).

Studying Figure 5.18, strain localisation is present for all revolutions in the spiral, which agrees with the crack development provided by DIC. Similar as the previous specimens, the highest strains on the surface is present at a height of 300 mm, along with the peak strain values measured by the DOFS. All of the faces obtain clear cracks and the most pronounce ones develop at Face 1 and 2. The crack on Face 1 starts off centrally and propagtes slightly shifted towards the corner whereas the crack on Face 2 is centrally located over its height.

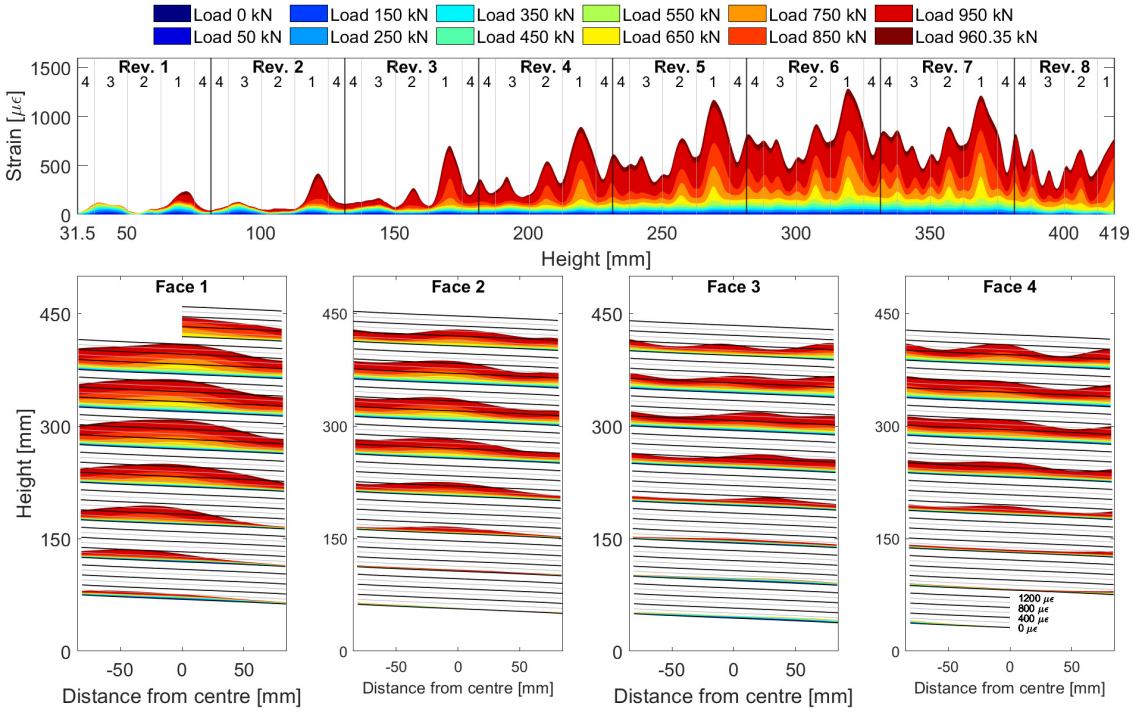

Figure 5.17: Strain profiles for different load steps obtained by DOFS located at the outer spiral of Specimen 5 (SFRC). The bottom plots display the projected strain profiles on each face of the specimen.

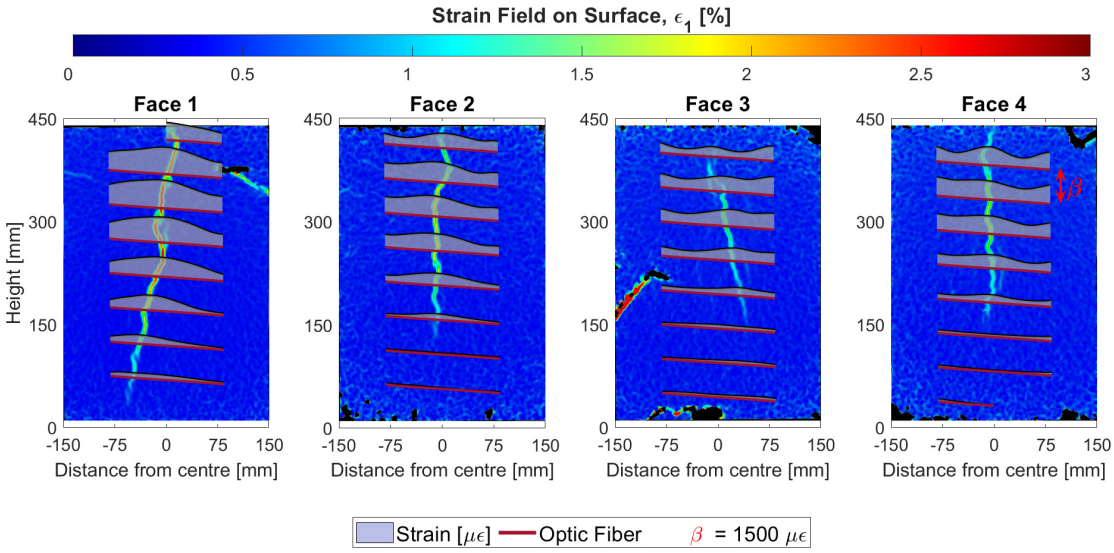

Figure 5.18: Surface strain fields measured with DIC compared with DOFS measured strains at 950 kN for Specimen 5 (SFRC).

The figures show that the strain localisation obtained from DOFS in the outer spiral agrees well with the data obtained from DIC. However, some specimens have minor discrepancies between the DOFS and DIC data, which could be associated with the scaling of the DIC images. Since the field view of the camera could not capture the entire surface, the data needs to be scaled accordingly. Yet, all images have been uniformly scaled to facilitate post-processing, which may result in some variability in presented results.

5.5 Crack width evaluation based on DOFS measurements and DIC

The data obtained by the DIC made it possible to follow the formation and development of the surface cracks during loading. Since the strains were largest at revolution 5-7 of the outer spirals, the surface cracks were measured at those heights. Thus, the surface crack development obtained from DIC can be compared the DOFS measurements. Two approaches were employed to calculate the crack width based on DOFS measurement: a lower and an upper crack width, denoted as lower and upper bound, respectively. For both approaches, it was assumed that the measured strains on the face correlated with the surface crack because only one crack was formed per face at those heights for all specimens. In the lower bound approach, defined in Equation 5.1, it was assumed that only strains exceeding the elastic concrete strain contribute to crack width. The crack strain was set to zero if the strain did not exceed the elastic strain. In the upper bound approach, defined in Equation 5.2, all strains, except negative ones, was assumed to contribute to the crack width. The crack width for both approaches was determined by integrating the crack strains along the face's arc length of the outer spiral, see Figure 5.19. In the following chapter, calculated crack widths refer to the cracks calculated based on DOFS measurement, and measured crack widths refer to the cracks measured from the DIC data. The Mean Absolute Error (MAE) for the calculated crack width in relation to the measured crack widths is presented in Table 5.2 and was calculated using Equation 5.3. The upper bound approach has the lowest average MAE, and specimen 4 has the lowest MAE.

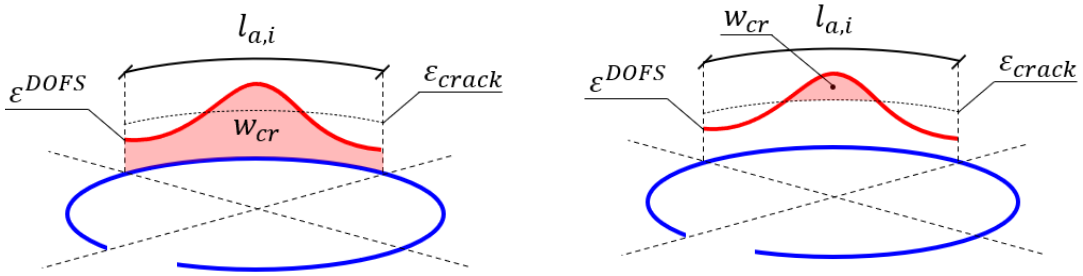

(a) Upper bound **(b)** Lower bound

Figure 5.19: Methodology for determining crack widths using DOFS measurements.

$$w_{cr}^{lb} = \int_{-l_{a,i}/2}^{l_{a,i}/2} \begin{cases} \epsilon^{DOFS}(x) - \epsilon_{crack} & \text{for} \quad \epsilon^{DOFS}(x) \geq \epsilon_{crack} \\ 0 & \text{for} \quad \epsilon^{DOFS}(x) < \epsilon_{crack} \end{cases} dx \tag{5.1}$$

$$w_{cr}^{ub} = \int_{-l_{a,i}/2}^{l_{a,i}/2} \begin{cases} \epsilon^{DOFS}(x) & \text{for} \quad \epsilon^{DOFS}(x) \geq 0 \\ 0 & \text{for} \quad \epsilon^{DOFS}(x) < 0 \end{cases} dx \tag{5.2}$$

where w_{cr}^{lb} is the lower bound calculated crack width, w_{cr}^{ub} is the upper bound calculated crack width, $l_{a,i}$ is the arc length, ϵ^{DOFS} is the strain measured by DOFS, and ϵ_{crack} is the crack strain of concrete.

$$MAE = \frac{\sum_{i=1}^{n} \left| w_{cr}^{calculated} - w_{cr}^{measured} \right|}{n} \tag{5.3}$$

where $w_{cr}^{calculated}$ is the calculated crack width obtained by lower bound or upper bound approach, $w_{cr}^{measured}$ is the measured crack width obtained via DIC, and n is the number of measurement points.

Table 5.2: The Mean Absolute Error for the upper and lower bound calculated crack width to the measured crack widths, calculated according to Equation 5.3.

Specimen No.	Height	MAE Lower Bound	MAE Upper Bound
1	269 mm	0.017 mm	0.005 mm
	319 mm	0.016 mm	0.003 mm
	369 mm	0.008 mm	0.007 mm
2	269 mm	0.013 mm	0.002 mm
	319 mm	0.014 mm	0.003 mm
	369 mm	0.015 mm	0.002 mm
3	269 mm	0.016 mm	0.018 mm
	319 mm	0.014 mm	0.014 mm
	369 mm	0.015 mm	0.015 mm
4	256 mm	0.004 mm	0.008 mm
	306 mm	0.003 mm	0.011 mm
	356 mm	0.003 mm	0.013 mm
5	269 mm	0.016 mm	0.009 mm
	319 mm	0.017 mm	0.010 mm
	369 mm	0.013 mm	0.010 mm
6	269 mm	0.020 mm	0.018 mm
	319 mm	0.021 mm	0.018 mm
	369 mm	0.026 mm	0.019 mm
Mean		0.014 mm	0.010 mm

The crack widths measured by DIC and calculated based on DOFS measurement during loading for Specimens 1, 4, and 5 are presented in Figures 5.20-5.22. The face with the widest crack was chosen for each specimen: Face 1 for Specimen 1 and 5 and Face 2 for Specimen 4. It can be observed that all specimens have the largest measured cracks and calculated cracks at revolutions 6 and 7. According to Table 5.3, the DOFS strains in the inner spiral exceed the elastic concrete strain at a lower load than the outer spiral. Hence, cracking initiates in the region near the inner spiral and propagates towards the surface. Upon studying Figure 5.20-5.22, all graphs show a noticeable slope change during loading. This change in slope may be due to crack formation or widening.

Table 5.3: The loads when the strain exceeds the cracking strain at the inner spiral and outer spiral for the different specimens.

Specimen No.	Inner Spiral	Outer Spiral
1	514 kN	559 kN
2	521 kN	579 kN
3	360 kN	404 kN
4	520 kN	591 kN
5	377 kN	461 kN
6	487 kN	576 kN

The smallest crack widths develop in Specimen 1. Figure 5.20 shows that the crack widths are largest at 319 mm (rev 6), with a maximum measured crack width of 0.06 mm at 960 kN. The strains measured by DOFS on the outer spiral exceed the crack strain of approximately 600 kN, and surface cracking was observed at approximately 700 kN. When cracking is initiated, there is no significant change in the slope, which may indicate a relatively stable crack development. The upper bound approach correlates better with the measured crack width, as shown in Figure 5.20. This is also confirmed by the lower MAE in Table 5.2.

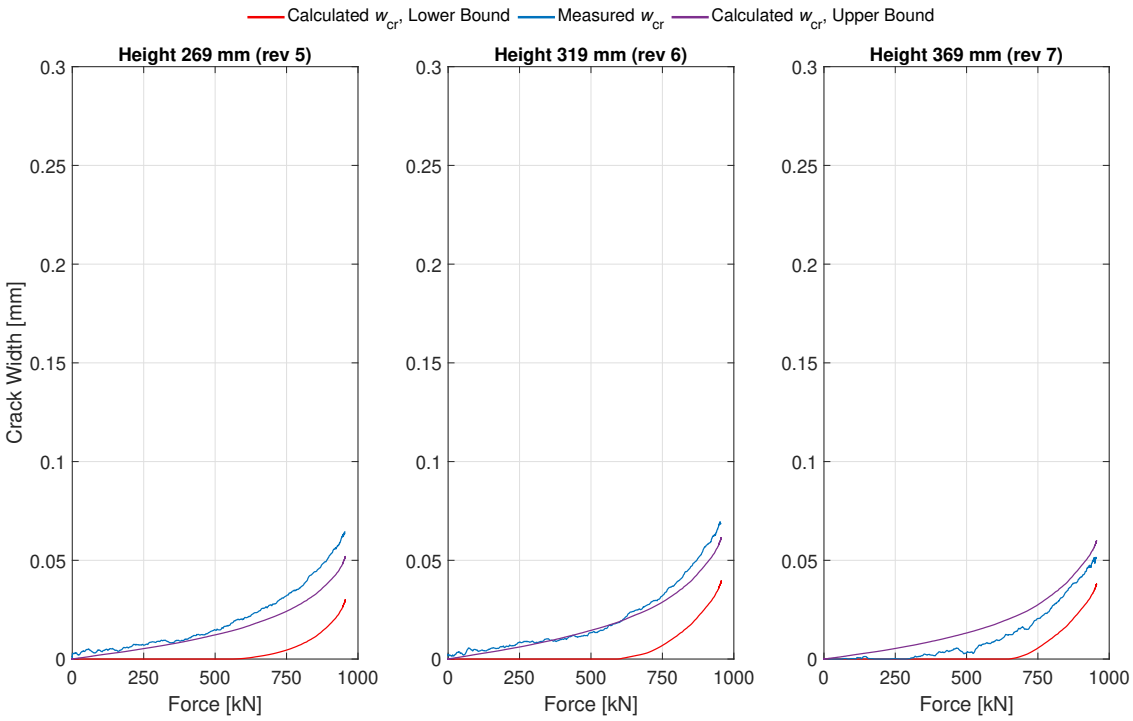

Figure 5.20: Comparison of measured crack widths from DIC and calculated crack widths based on DOFS measurements calculated using Equations 5.1 and 5.2 during loading for Specimen 1 (Reference).

Upon studying Figure 5.21, a similar response as for Specimen 1 can be observed for Specimen 4. The DOFS-measured strains exceed crack strains at approximately 650 kN and surface cracks are observed at 750 kN. However, the crack widths are

larger for Specimen 4, and the slope of the curves changes significantly at 920 kN. The slope change may indicate a more rapid crack development for loads over 920 kN. The measured crack width reaches a maximum value of 0.09 mm at 356 mm with a load of 960 kN. Studying Figure 5.2, the measured cracks correlate better to the lower bound approach of calculated crack widths. This is also confirmed by the lower MAE in Table 5.2

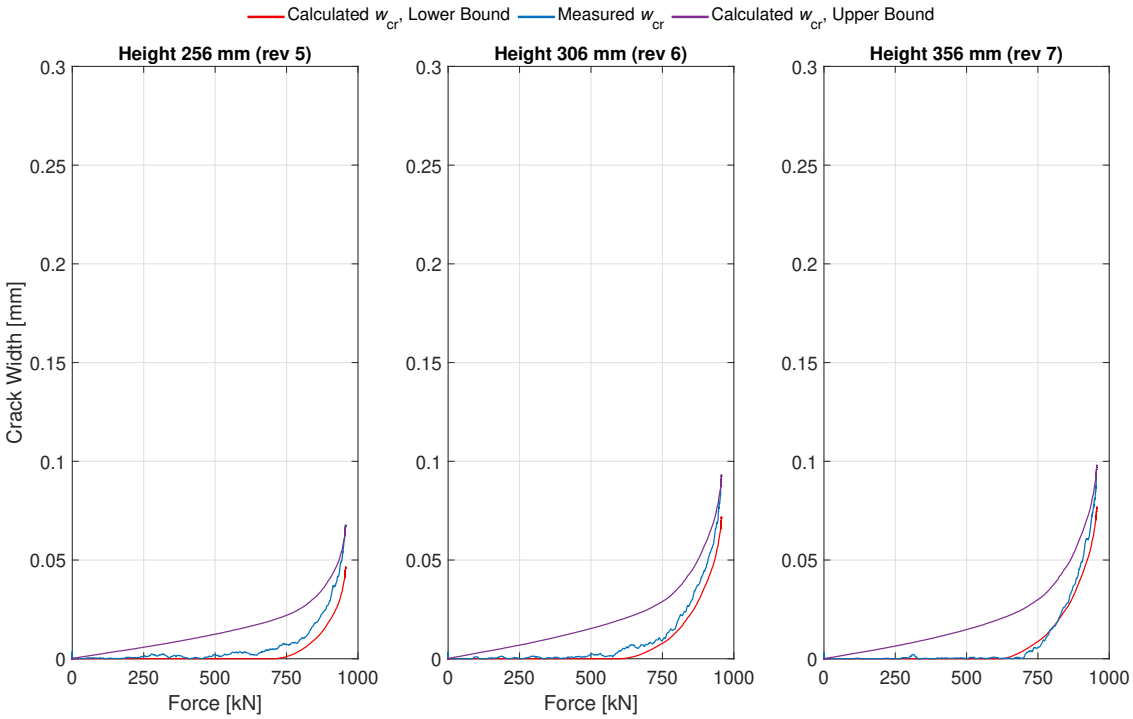

Figure 5.21: Comparison of measured crack widths from DIC and calculated crack widths based on DOFS measurements calculated using Equations 5.1 and 5.2 during loading for Specimen 4 (SFRC + Helix).

The largest crack width are present in Specimen 5. The DOFS-measured strains exceed crack strains at approximately 480 kN, and surface cracks are observed at 600 kN. The crack-width curves for Specimen 5, in Figure 5.22, have steeper slopes than the other specimens. The calculated curves have a constant slope up to 900 kN, beyond which there is a sudden change in crack widths and slope inclination. The same response can be observed in the measured curves with a sudden change in crack width at 900 kN, followed by a change in inclination. This sudden change may be due to a full crack opening and followed by initiation of fibre pull out. The load of 960 kN caused a measured maximum crack width of 0.22 mm at 319 mm height (rev. 6). The measured crack width has slightly stronger correlations to the upper bound approach than the lower bound in Figure 5.22. It is further supported by the smaller MAE values given in Table 5.2.

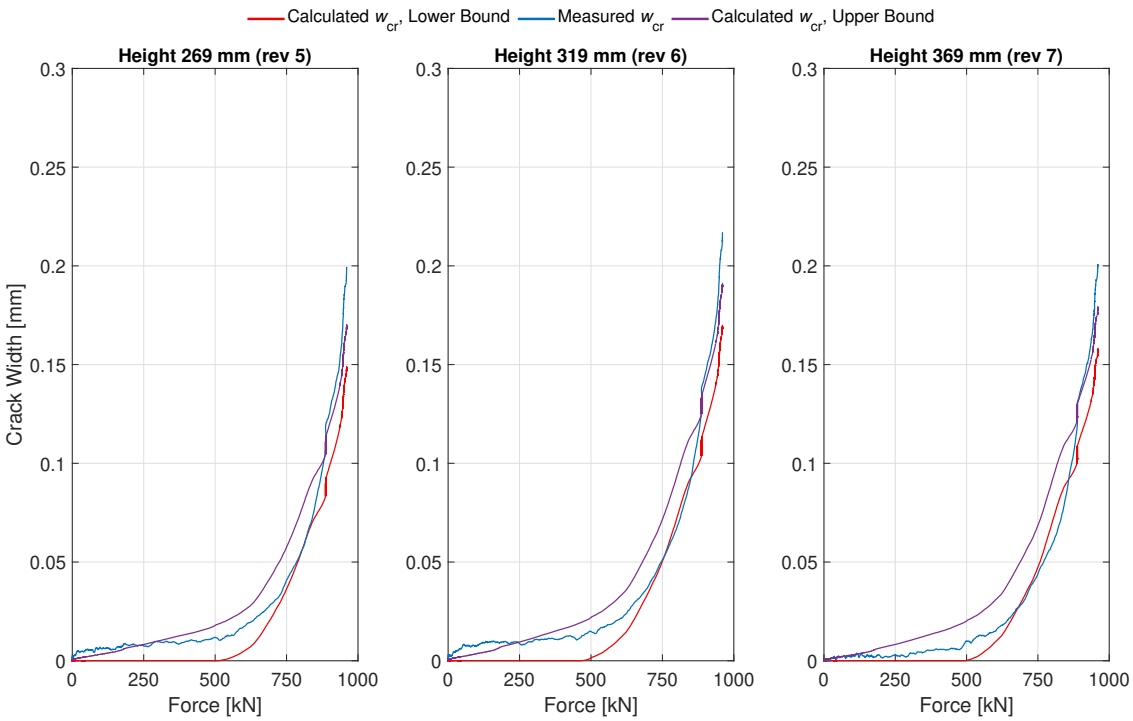

Figure 5.22: Comparison of measured crack widths from DIC and calculated crack widths based on DOFS measurements calculated using Equations 5.1 and 5.2 during loading for Specimen 5 (SFRC).

6
Discussion

6.1 Evaluation of assessment method

Designing an assessment method to monitor 3D effects in a discontinuity region involves several challenges. The major part involves creating a support for the DOFS that enables monitoring over a complex area and does not influence the structural response of the anchorage zone. Additional considerations include creating support that does not interfere with data collection via DOFS, which imposes requirements on the interaction between the materials. Positioning of the fibre optics is also crucial to enable the post-processing of data. This requires ensuring that the supports maintain their intended position throughout casting and enable the precise localisation of strain data.

The proposed assessment method in this master's thesis enables a structural response comparison of a discontinuity region with varying designs. Without material testing of the spiral and its interaction with the concrete, quantifying the impact on measured strains and the specimens' structural response is unattainable. However, the spiral was designed to have minimal influence on the structural response. This was achieved by designing the spiral with a large pitch to minimise segregation and choosing a plastic material with low stiffness. The plastic parts were also designed with holes to improve the bonding effect and, more likely, measure the true concrete strains. After aligning the strain distribution from DOFS with DIC, it can be verified that the fiber optics' support structure allows for the assessment of the specimens' structural response.

With the current design of the DOFS, certain desired analyses were not feasible to conduct. As the two spirals have different pitches, directions, and starting positions, comparisons of the results provided by the inner and outer spirals were unfeasible. If the spirals had the same pitch and direction, the data along the length of the fiber would be compatible as it would correspond to the same orientation in the specimen. Throughout the post-processing of the results, some difficulties were raised regarding the localisation of the strains provided by the DOFS attached to the helix reinforcement. The helix reinforcement provided by CCL was not identical in terms of geometry, where some helices had different diameter and pitches. This implied some issues regarding the localisation of the strains and also an error source to potential shifts in the strain localisation between the data obtained from the inner and outer spiral, see for example Figure A.2. To improve the results, it would have

been beneficial to strive for identical helical reinforcement with consistent geometry. Based on those helices, the outer should haven be designed with the same pitch. The inconsistency of the geometry of the helix reinforcement is noticeable in Figures E.1 - E.4.

The DIC images and DOFS data reveal that all specimens experienced strain localization and crack initiation. However, in some cases, the evaluation of the post-crack response was restricted because the test rig reached its maximum load early in the crack propagation phase. Therefore, enhancing the load capacity of the test rig would be advantageous to facilitate a more comprehensive analysis of the structural response. This is essential since the NLFEA, as illustrated in Figure 5.3, demonstrates global softening for all configurations, which is also expected in practice.

6.2 Evaluation of the different configurations of anchorage zones

Upon analysing the structural response of the various anchorage zones, it becomes evident that the plain SFRC specimen develops the largest strains and crack widths during the load testing, as observed in Chapters 5.3 - 5.5. Unlike the other reinforcement configurations, the largest strains develop around the inner spiral, as mentioned in Chapter 5.3. The additional helix reinforcement appears to significantly influence this cracking process by reducing strains and crack widths in the specimen, particularly around the anchorage system. Consequently, the same magnitude of strains is developed around both the inner and outer spiral, comparable to the response of the reference specimen. Therefore, it can be concluded that the addition of helix reinforcement significantly influences the cracking process, decreases the strain development near the anchorage system, and prevents crack propagation against the surface. These phenomena may be attributed to the confinement of the concrete.

As stated in Chapter 2.2 and upon analysing DOFS and DIC, multiaxial stress states are present in the anchorage zones. As concrete strengths are dependent on the actual stress state, as described in Chapter 2.3.4, this may influence the formation of cracks in those regions. Similarly, as stated in Chapter 2.2, crack initiation occurs locally around the anchorage system for all specimens and propagates towards the surfaces of the specimens, see Table 5.3. It can also be observed that the largest strains and crack widths occur at a height of approximately 300 mm, a bit further down compared to where the maximum tensile stresses are observed in Chapter 2.2. This could be attributed to the ribs and depth of the anchorage system, which may contribute to the force introduction being distributed more vertically within the specimen rather than applying it directly on top of it. This may lead to a vertical shift in the discontinuity regions causing the peak strains and crack widths are located further down. Studying the crack pattern in Chapter 5.4 and Appendix F, it is evident that the SFRC has a crack spanning a larger height than the other configurations. The presence of a helix seems to contribute to a more predictable

response with cracks in the bursting zone, as mentioned in Chapter 2.2, by confining the concrete in this zone. In the bursting zone of the plain SFRC, cracks localise as expected but propagate unpredictably below this region.

Strain localisation was observed centrally oriented on the faces of the different specimens. However, the most pronounced strain localisation occurred on Face 1 for all specimens except Specimen 4. This phenomenon is likely due to the design of the anchorage system, which features a protruding rounding towards Face 1. Consequently, Face 1 has the smallest concrete cover, and the protruding rounding likely concentrates stresses on this face, leading to crack initiation and propagation.

Upon evaluating the response of specimens containing SFRC, notable variations can be observed, particularly between Specimens 3 and 4. These variations may be attributed to factors such as local segregation of concrete or misalignment of the tendon head, leading to uneven pressure distribution. However, the material tests presented in Chapter 4.1 indicates a greater variability in the results for SFRC compared to plain concrete. Therefore, it is also reasonable to associate the differing structural responses with the inconsistent SFRC material properties. Additionally, the material curves show that plain concrete has a larger mean tensile strength, which results in crack initiation at higher loads.

7
Conclusion

Designing an effective assessment method for monitoring 3D effects in discontinuity regions requires careful consideration of designing the support structure of the DOFS. The proposed method allowed for analysis and comparison of the structural response of anchorage of varying designs. Additionally, the proposed method, with the strive of minimising the structural influence, allowed the assessment of crack propagation with high compliance to surface crack propagation.

Analysing the structural response of the different reinforcement configurations, the contemporary design approach exhibited the smallest crack widths, while the SFRC configuration exhibited the widest. The presence of helix reinforcement had a notable influence on crack propagation, reducing strains and crack widths, leading to a more predictable crack propagation compared to plain SFRC. However, when considering material efficiency, working conditions, and crack width limitations, the SFRC configuration has many advantages.

7.1 Further outlook

Overall, although variations in structural response were observed among specimens, the proposed assessment method offers valuable insights into the response of different reinforcement configurations. Future improvement in the design of DOFS monitoring could enhance the assessment method for evaluating structural responses in discontinuity regions. Investigating designs that are commonly used in the industry could provide additional valuable insight. Furthermore, investigation of the utilisation of SFRC in post-tensioned anchorage zones could be improved by elaborating on the fibre volume fraction and types of fibres used.

Bibliography

Al-Emrani, M., Engström, B., Johansson, M., & Johansson, P. (2011). *Bärande konstruktioner Del 2* (tech. rep.). Chalmers tekniska högskola.

Barrias, A., Casas, J. R., & Villalba, S. (2016, May). A review of distributed optical fiber sensors for civil engineering applications. https://doi.org/10.3390/s16050748

Bekaert. (2023). Datasheet Dramix4D 65/35BG EN-UK.

Berrocal, C. G., Fernandez, I., & Rempling, R. (2021). Crack monitoring in reinforced concrete beams by distributed optical fiber sensors. *Structure and Infrastructure Engineering*, *17*(1), 124–139. https://doi.org/10.1080/15732479.2020.1731558

Blomfors, M., Berrocal, C. G., Lundgren, K., & Zandi, K. (2020). Incorporation of pre-existing cracks in finite element analyses of reinforced concrete beams without transverse reinforcement. https://doi.org/10.1016/j.engstruct.2020.111601

Breen, J., Burdet, O., Roberts, C., Sanders, D., & Wollmann, G. (1994). *Anchorage Zone Reinforcement for Post-Tensioned Concrete Girders*.

CCL. (2017). POST-TENSIONING SYSTEMS - XM SYSTEM. www.cclint.com

Engström, B. (2015). *Design and analysis of deep beams, plates and other discontinuity regions*. Chalmers University of Technology.

Engström, B. (2011). *Design and analysis of prestressed concrete structures*. Chalmers University of Technology.

European Committee for Standardization. (2005). Eurocode 2 – Design of concrete structures – Part 2: Concrete bridges – Design and detailing rules.

European Committee for Standardization. (2004). Eurocode 2: Design of concrete structures - Part 1-1: General rules and rules for buildings.

European Committee for Standardization. (2019). Testing hardened concrete - Part 3: Compressive strength of test specimens.

European Technical Assessment. (2015). European Technical Approval CCL 'X' Range Post-tensioning system.

Fernandez, I., Berrocal, C. G., & Rempling, R. (2023). Two-dimensional strain field analysis of reinforced concrete D-regions based on distributed optical fibre sensors. *Engineering Structures*, *278*. https://doi.org/10.1016/j.engstruct.2022.115562

Ferreira, D. (2024). Theory Manual - DIANA 10.8. https://manuals.dianafea.com/d108/en/931990-931990-theory-dev.html

Galeote, E., Picazo, Á., Alberti, M. G., de la Fuente, A., Enfedaque, A., Gálvez, J. C., & Aguado, A. (2022). Statistical analysis of an experimental database

on residual flexural strengths of fiber reinforced concretes: Performance-based equations. *Structural Concrete*, *23*(5), 3140–3153. https://doi.org/10.1002/suco.202100416

Geel, E. v. (1998). *Concrete behaviour in multiaxial compression : experimental research*. Technische Universiteit Eindhoven, Faculteit Bouwkunde.

Gencturk, B., Hossain, K., Kapadia, A., Labib, E., & Mo, Y. L. (2014). Use of digital image correlation technique in full-scale testing of prestressed concrete structures. *Measurement: Journal of the International Measurement Confederation*, *47*(1), 505–515. https://doi.org/10.1016/j.measurement.2013.09.018

Glišić, B., Hubbell, D., Sigurdardottir, D. H., & Yao, Y. (2013). Damage detection and characterization using long-gauge and distributed fiber optic sensors. *Optical Engineering*, *52*(8), 087101. https://doi.org/10.1117/1.oe.52.8.087101

Häussler-Combe, U. (2022). Computational structural concrete: Theory and applications. *Computational Structural Concrete: Theory and Applications*, 1–423. https://doi.org/10.1002/9783433610268

Hillerborg, A. (1985). The theoretical basis of a method to determine the fracture energy GF of concrete. *Materials and Structures*, *18*(4), 291–296. https://doi.org/10.1007/BF02472919/METRICS

International Federation for Structural Concrete. (2013). *Fib model code for concrete structures 2010*. Ernst & Sohn.

Kanstad, T. (2021). Background document to the Stable version of prEN 1992-1-1:2021- 09 (CEN/TC 250/SC 2/WG 102 N 321) Annex L Steel Fibre Reinforced Concrete (SFRC).

Kotsovos, M. D. (2015). *Finite-Element Modelling of Structural Concrete*. CRC Press. https://doi.org/10.1201/b18496

Kupfer, H., Hilsdorf, H. K., & Rusch, H. (1969). Behavior of Concrete Under Biaxial Stresses. *Journal Proceedings*, *66*(8), 656–666. https://doi.org/10.14359/7388

Lee, Y. H., & Kim, M. S. (2019). Investigation and Improvement of Bursting Force Equations in Posttensioned Anchorage Zone. *Advances in Materials Science and Engineering*, *2019*. https://doi.org/10.1155/2019/9807975

Löfgren, I. (2005). *Fibre-reinforced Concrete for Industrial Construction - a fracture mechanics approach to material testing and structural analysis* [Doctoral dissertation, Chalmers University of Technology].

Markeset, G., & Hillerborg, A. (1995). Softening of concrete in compression — Localization and size effects. *Cement and Concrete Research*, *25*(4), 702–708. https://doi.org/10.1016/0008-8846(95)00059-L

NORDTEST. (2005). WEDGE SPLITTING TEST METHOD (WST): FRACTURE TESTING OF FIBRE-REINFORCED CONCRETE (MODE I).

Omondi, B., Aggelis, D. G., Sol, H., & Sitters, C. (2016). Improved crack monitoring in structural concrete by combined acoustic emission and digital image correlation techniques. *Structural Health Monitoring*, *15*(3), 359–378. https://doi.org/10.1177/1475921716636806

Pham, Q. Q., Dang, N. L., Ta, Q. B., & Kim, J. T. (2021). Optimal localization of smart aggregate sensor for concrete damage monitoring in psc anchorage zone. *Sensors*, *21*(19). https://doi.org/10.3390/s21196337

Plos, M. (2000). *Finite element analyses of reinforced concrete structures*. Chalmers University of Technology.

Plos, M., Johansson, M., Zandi, K., & Shu, J. (2021). *Recommendations for Assessment of Reinforced Concrete Slabs*. Chalmers University of Technology.

Samani, A. K., & Attard, M. M. (2012). A stress–strain model for uniaxial and confined concrete under compression. *Engineering Structures*, *41*, 335–349. https://doi.org/10.1016/J.ENGSTRUCT.2012.03.027

Singh, H. (2017). Steel Fiber Reinforced Concrete. https://doi.org/10.1007/978-981-10-2507-5

A

Strain distribution arranged 3D

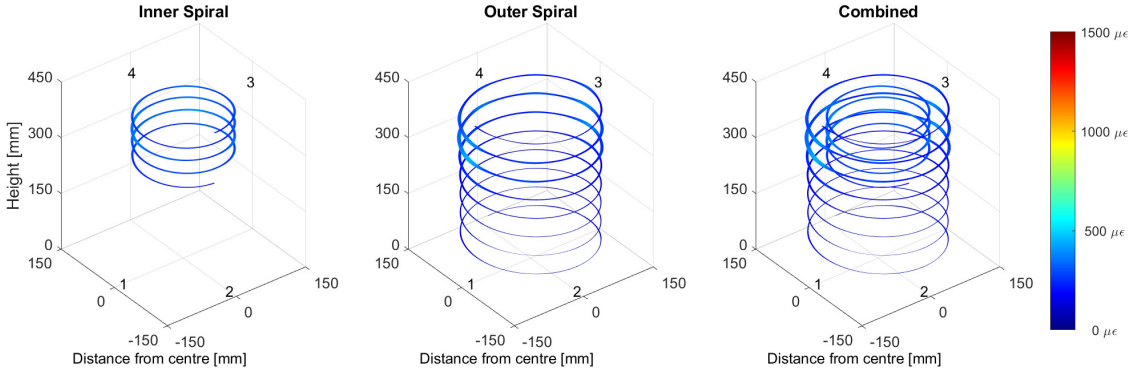

Figure A.1: Strain distribution at 950 kN obtained by DOFS located at the inner and outer spiral of Specimen 2 (Reference).

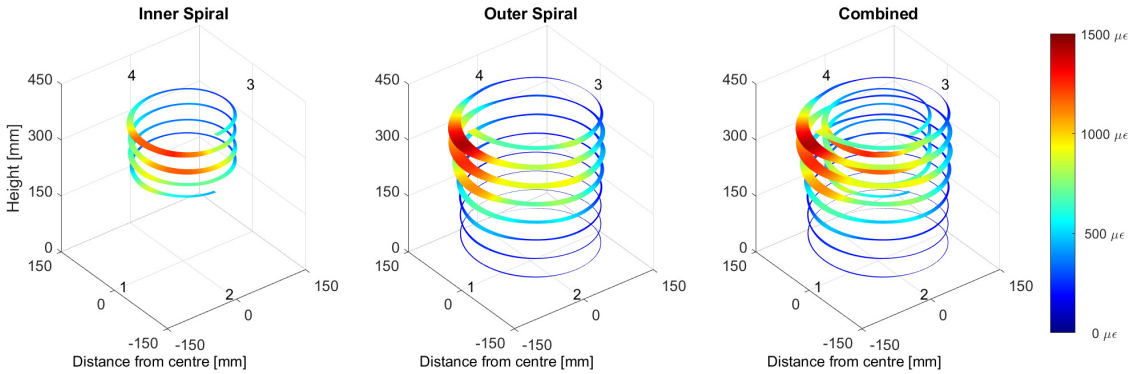

Figure A.2: Strain distribution at 950 kN obtained by DOFS located at the inner and outer spiral of Specimen 3 (SFRC + Helix).

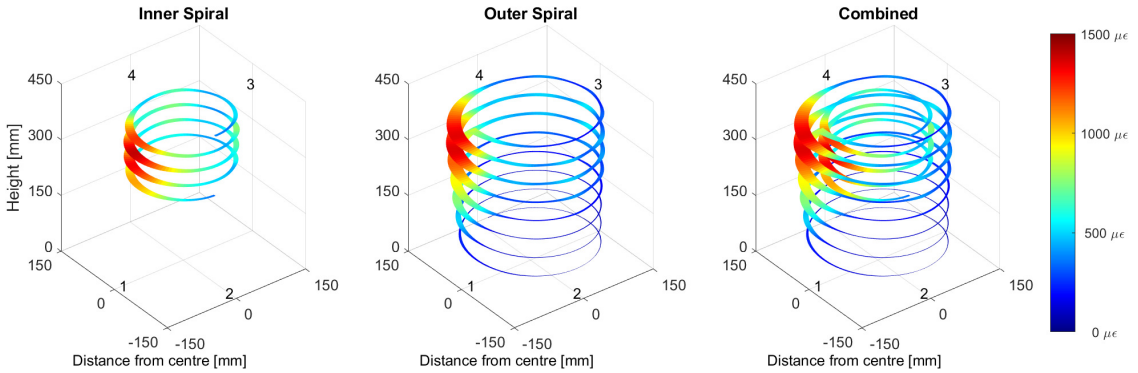

Figure A.3: Strain distribution at 950 kN obtained by DOFS located at the inner and outer spiral of Specimen 6 (SFRC).

B

Strain distribution in outer spiral

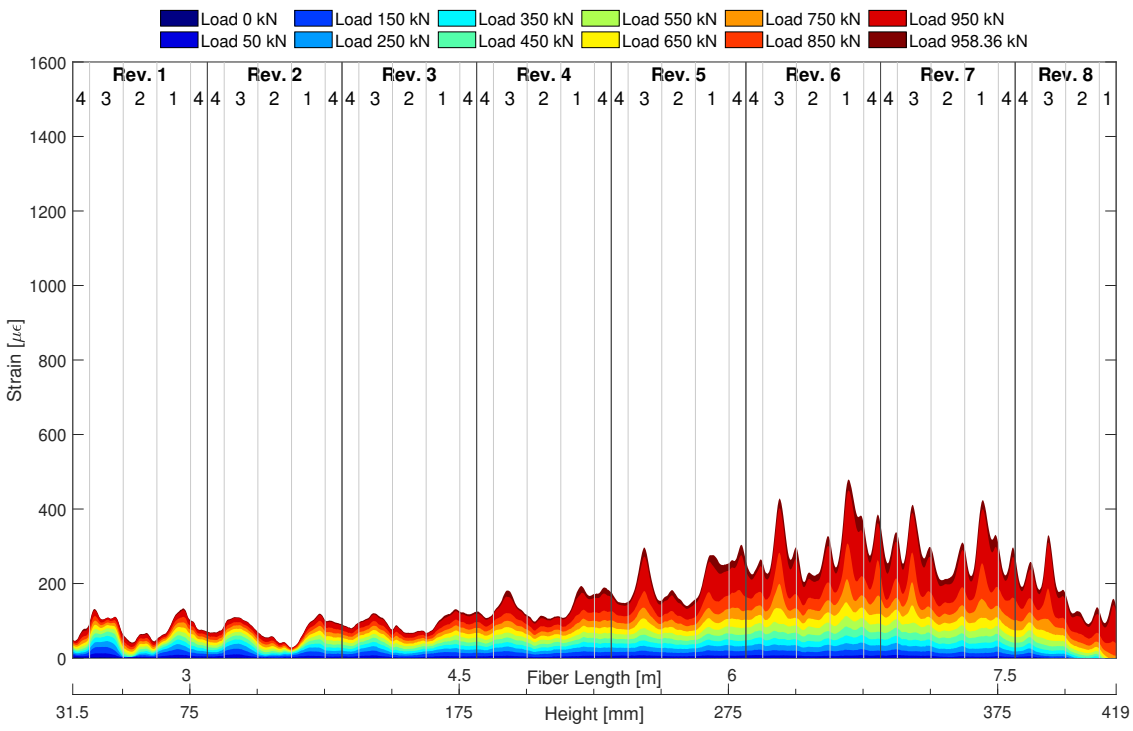

Figure B.1: Strain profiles for different load steps obtained by DOFS located at the outer spiral of Specimen 2 (Reference).

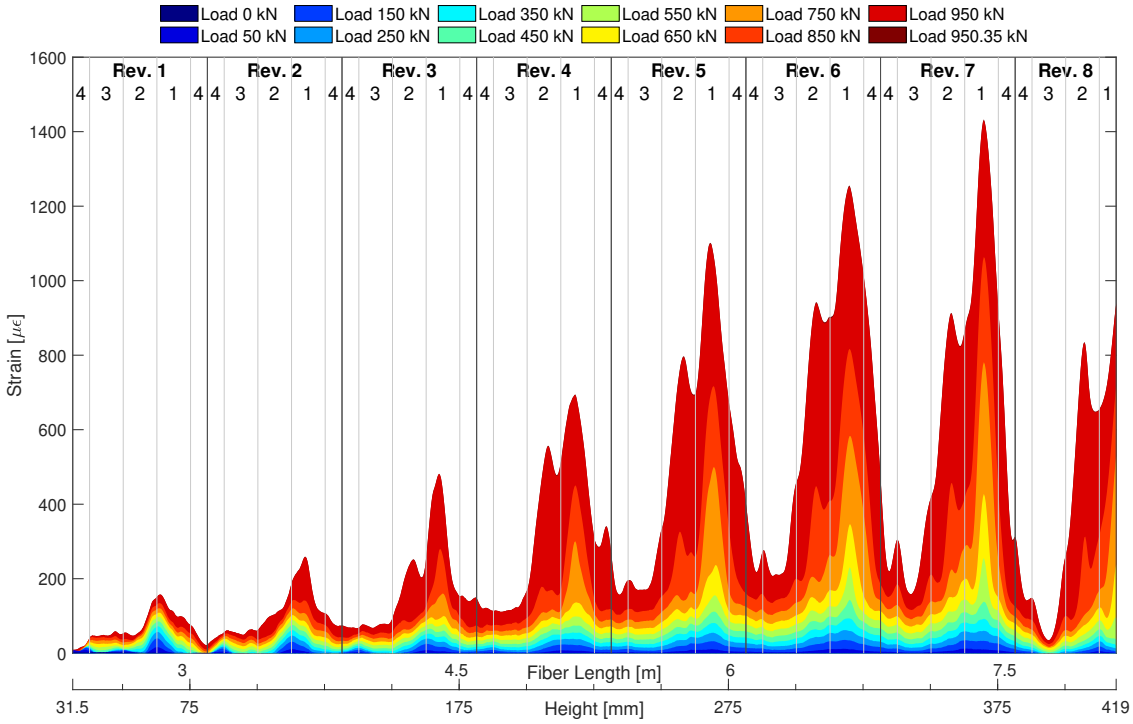

Figure B.2: Strain profiles for different load steps obtained by DOFS located at the outer spiral of Specimen 3 (SFRC + Helix).

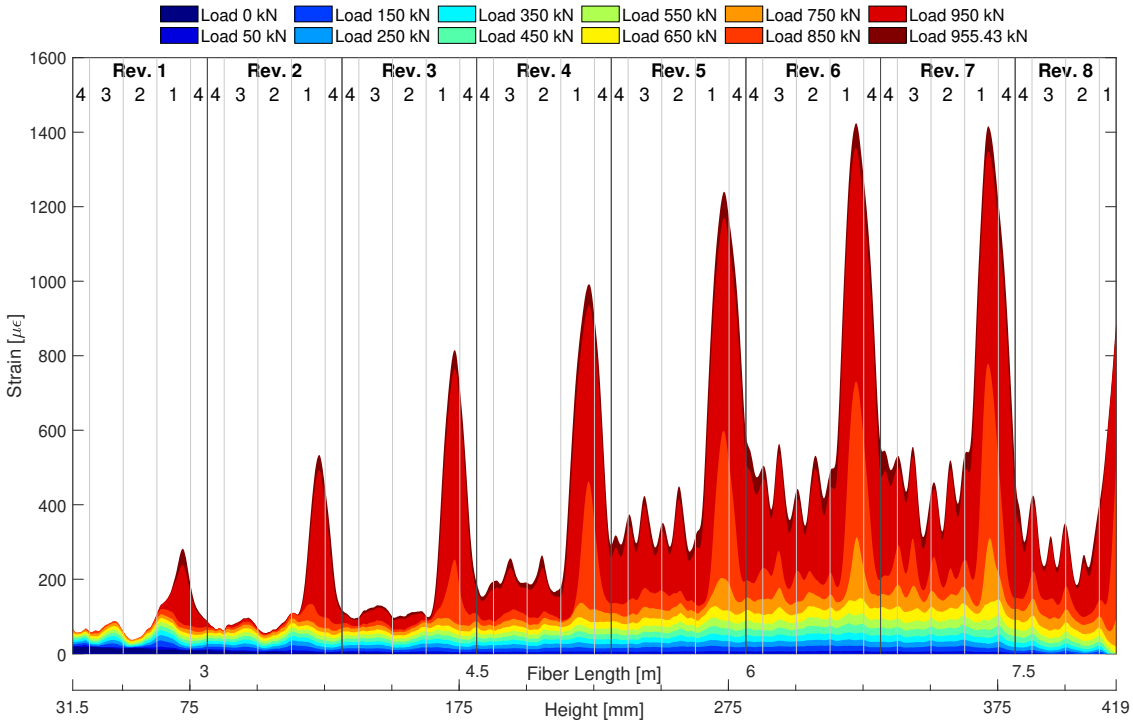

Figure B.3: Strain profiles for different load steps obtained by DOFS located at the outer spiral of Specimen 6 (SFRC).

C

Strain distribution in inner spiral

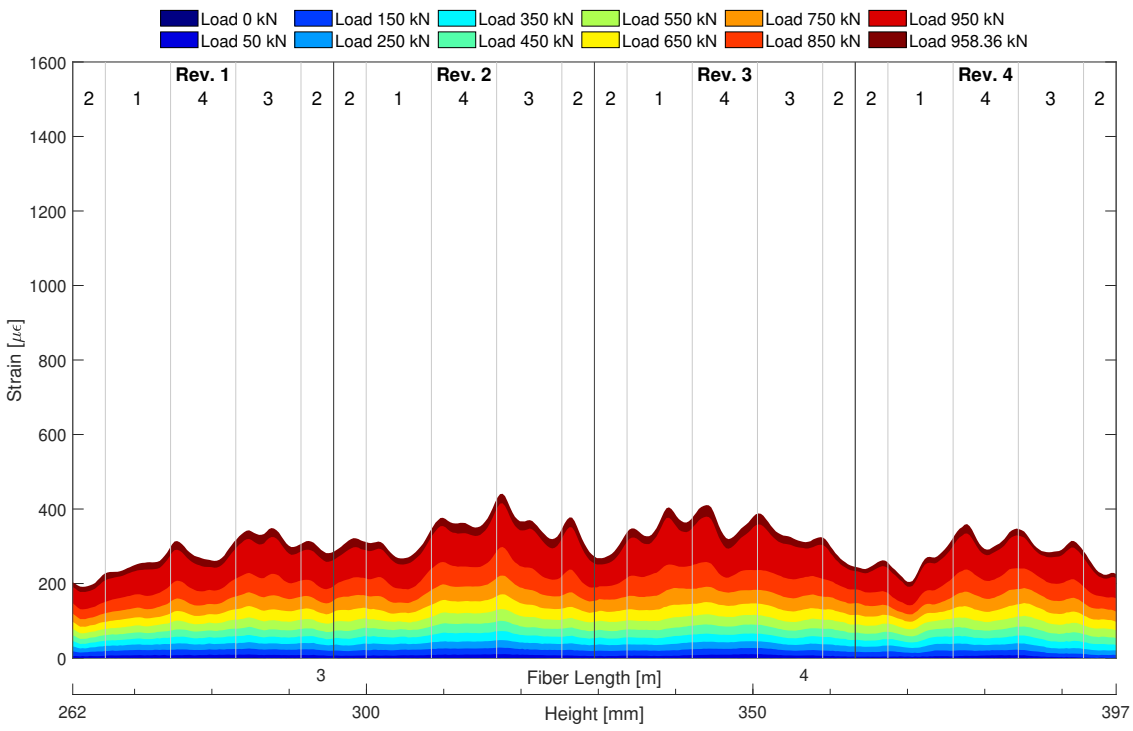

Figure C.1: Strain profiles for different load steps obtained by DOFS located at the inner spiral of Specimen 2 (Reference).

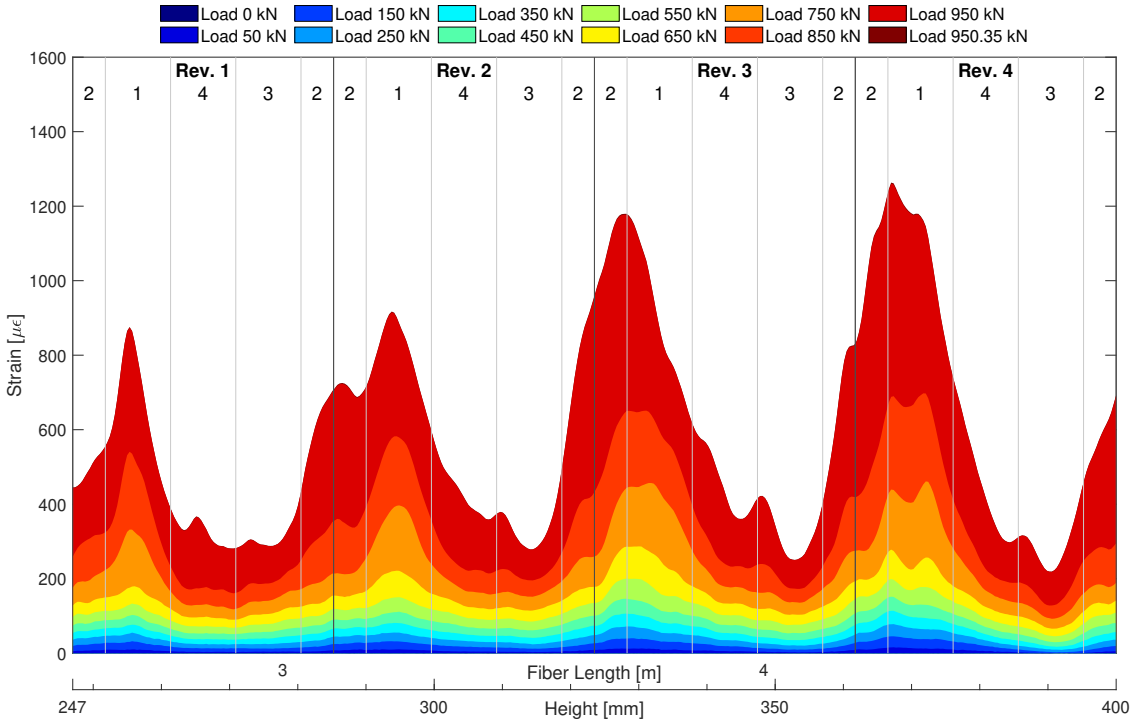

Figure C.2: Strain profiles for different load steps obtained by DOFS located at the inner spiral of Specimen 3 (SFRC + Helix).

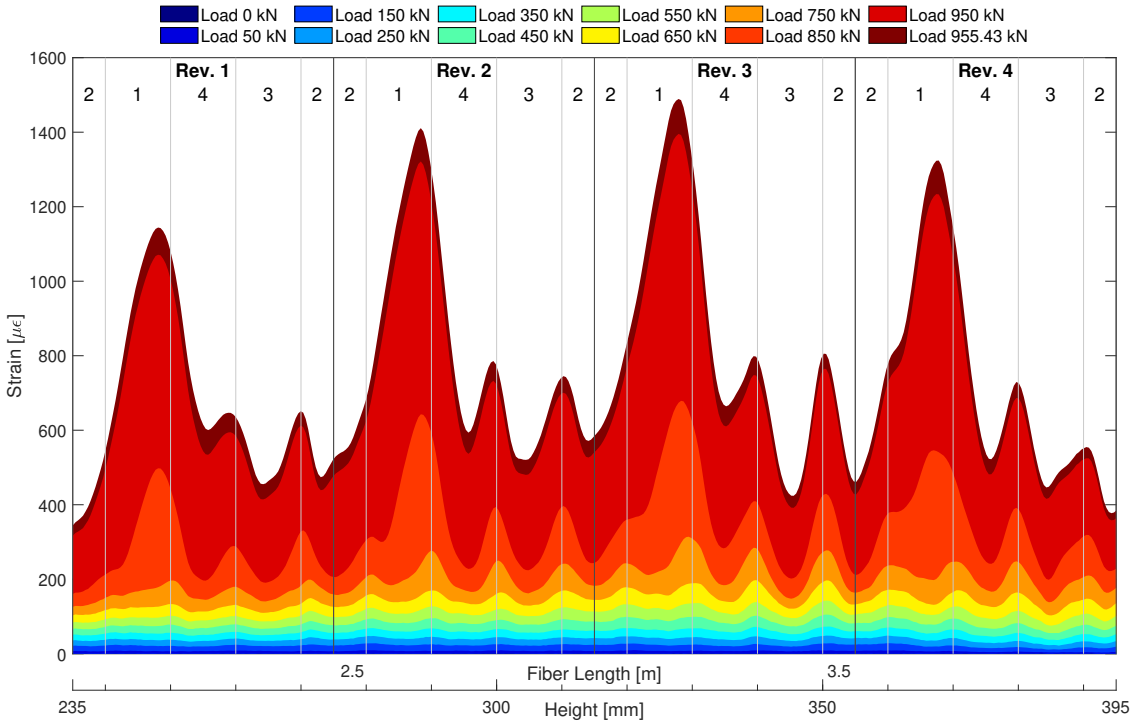

Figure C.3: Strain profiles for different load steps obtained by DOFS located at the inner spiral of Specimen 6 (SFRC).

D

Strain distribution in outer spiral divided by side

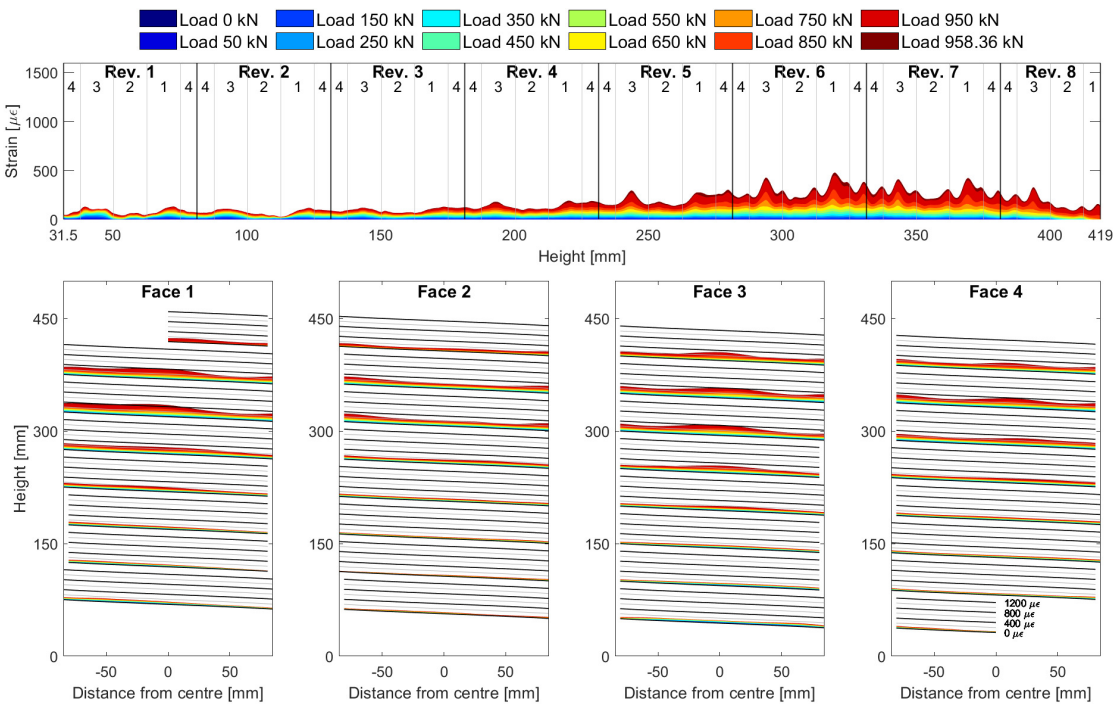

Figure D.1: Strain profiles for different load steps obtained by DOFS located at the outer spiral of Specimen 2 (Reference). The bottom plots display the projected strain profiles on each side of the specimen.

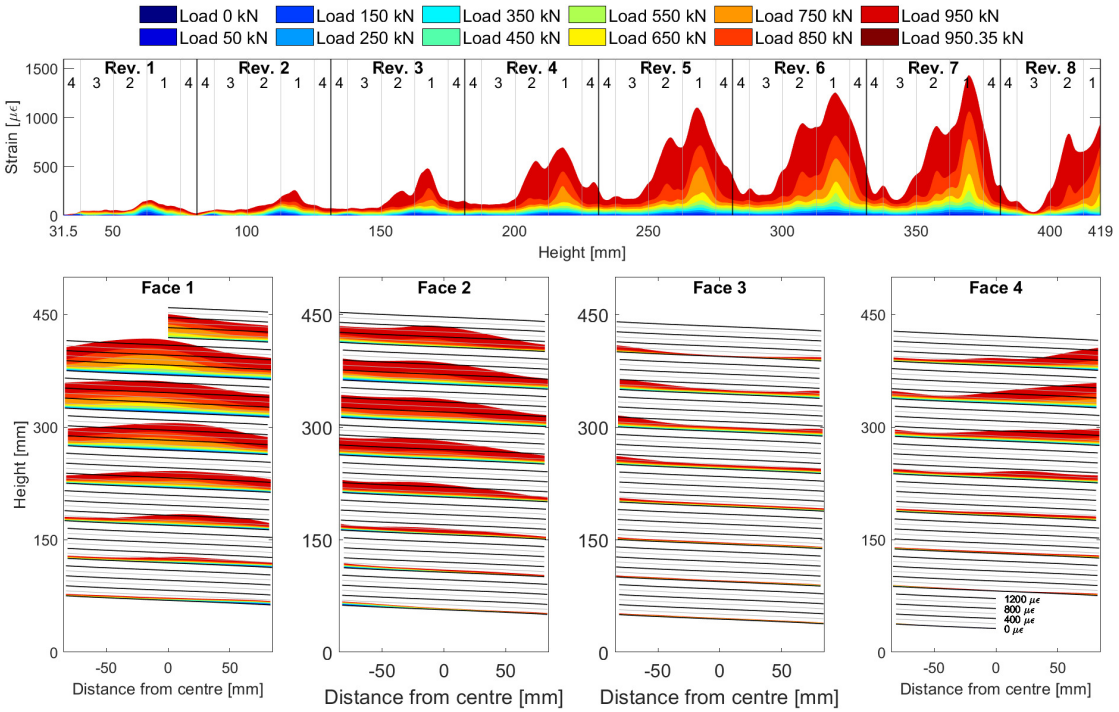

Figure D.2: Strain profiles for different load steps obtained by DOFS located at the outer spiral of Specimen 3 (SFRC + Helix). The bottom plots display the projected strain profiles on each side of the specimen.

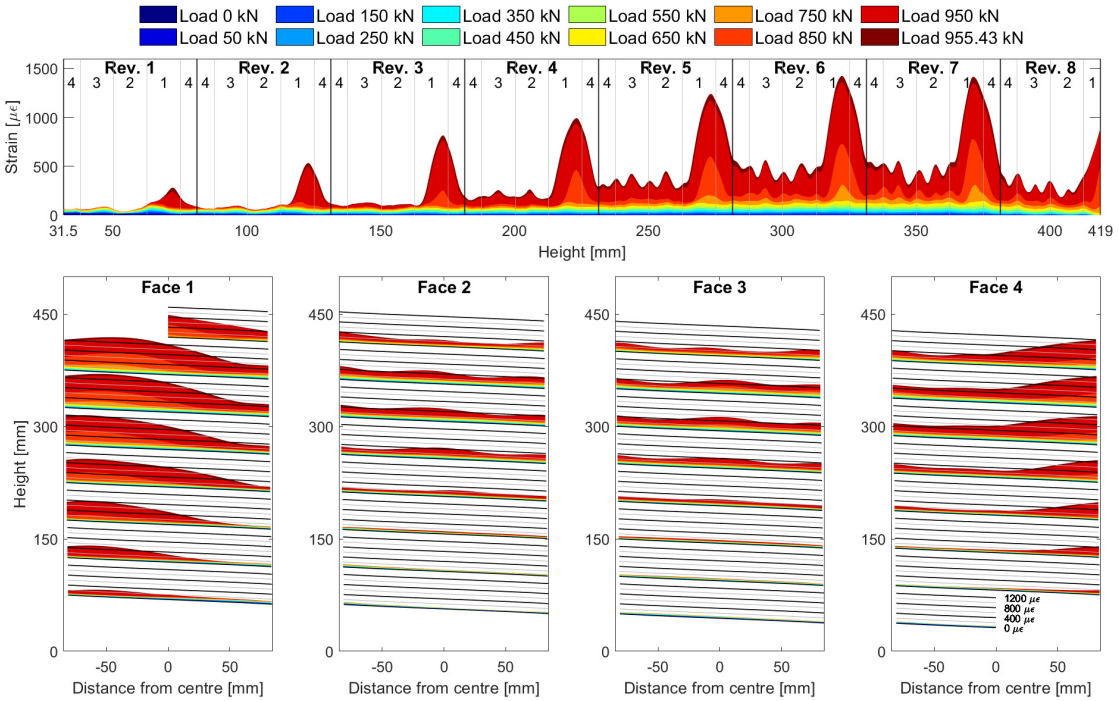

Figure D.3: Strain profiles for different load steps obtained by DOFS located at the outer spiral of Specimen 6 (SFRC). The bottom plots display the projected strain profiles on each side of the specimen.

E

Strain distribution in inner spiral divided by side

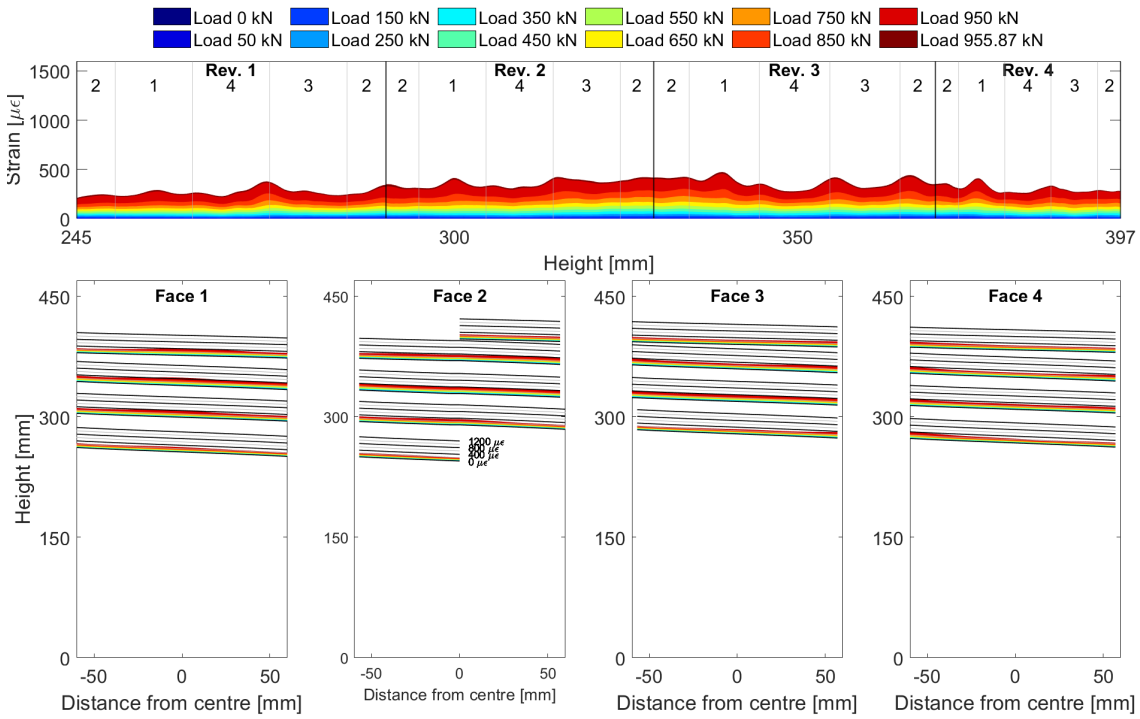

Figure E.1: Strain profiles for different load steps obtained by DOFS located at the inner spiral of Specimen 1 (Reference). The bottom plots display the projected strain profiles on each side of the specimen.

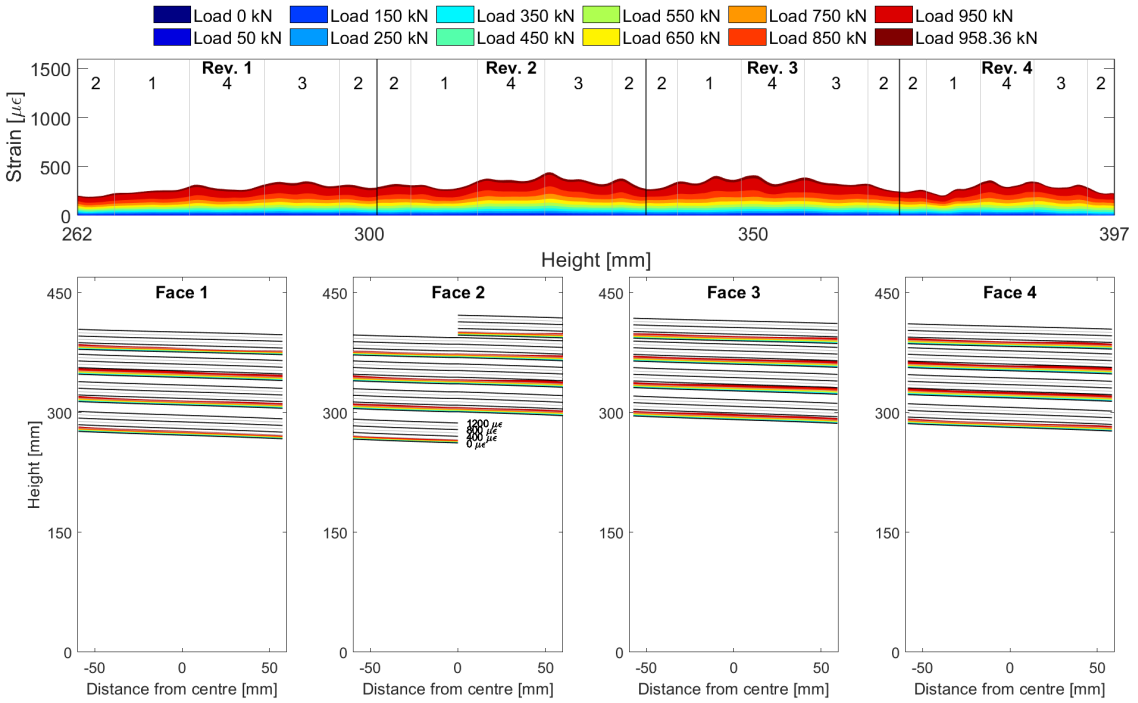

Figure E.2: Strain profiles for different load steps obtained by DOFS located at the inner spiral of Specimen 2 (Reference). The bottom plots display the projected strain profiles on each side of the specimen.

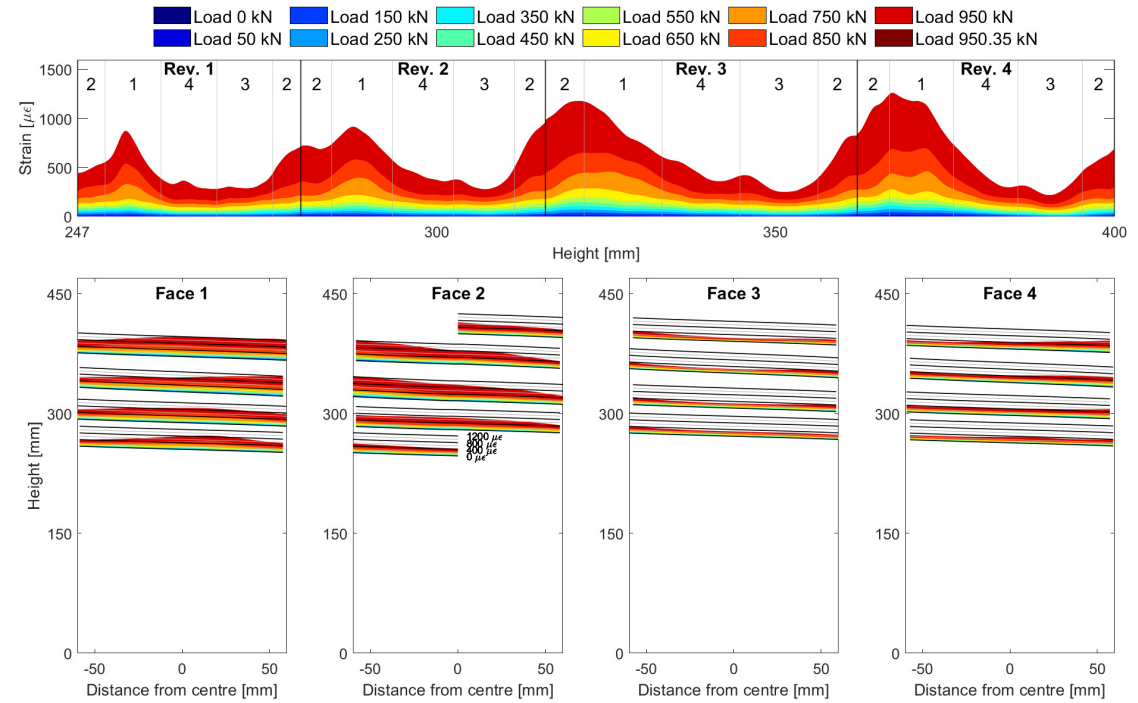

Figure E.3: Strain profiles for different load steps obtained by DOFS located at the inner spiral of Specimen 3 (SFRC + Helix). The bottom plots display the projected strain profiles on each side of the specimen.

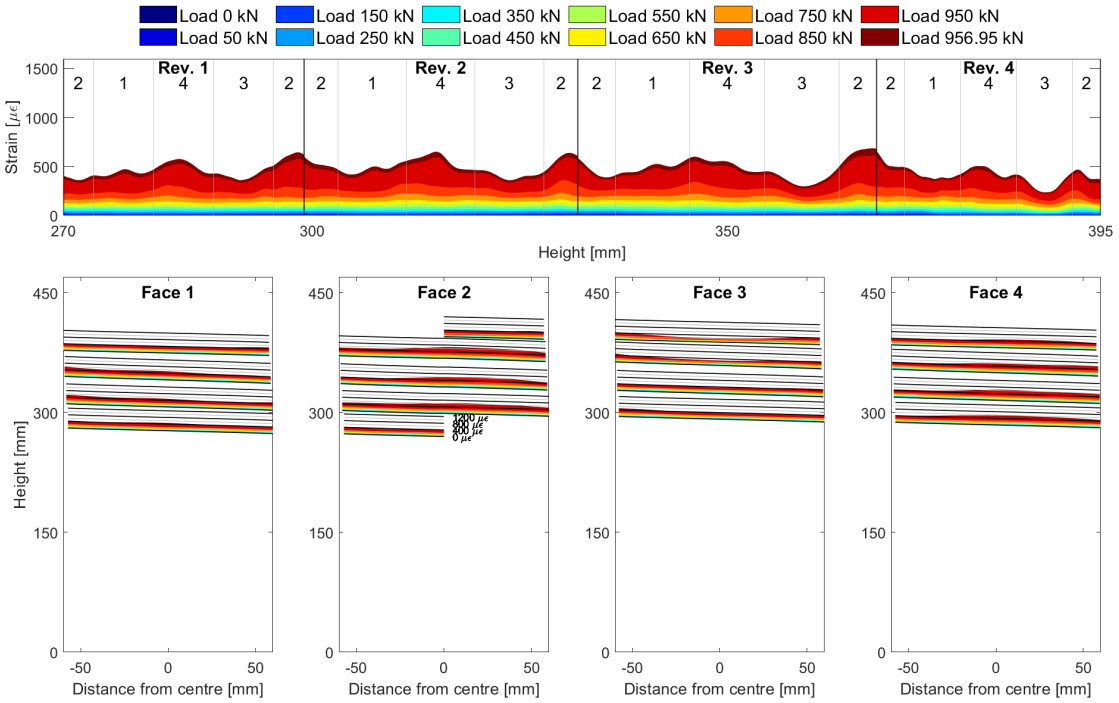

Figure E.4: Strain profiles for different load steps obtained by DOFS located at the inner spiral of Specimen 4 (SFRC + Helix). The bottom plots display the projected strain profiles on each side of the specimen.

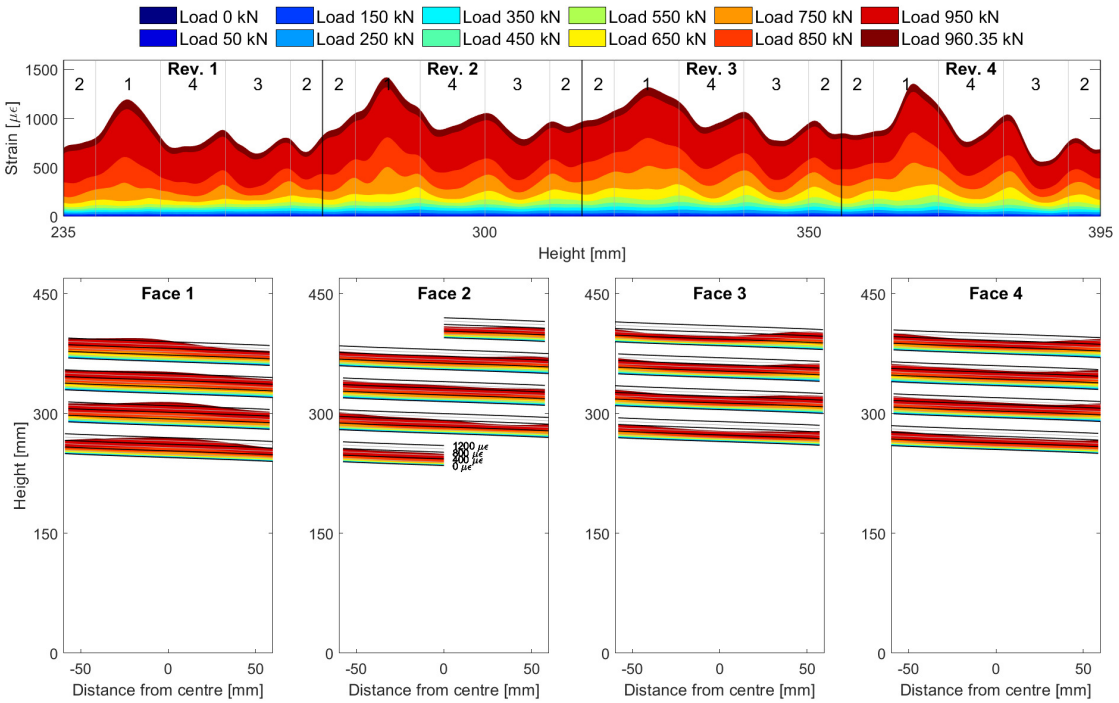

Figure E.5: Strain profiles for different load steps obtained by DOFS located at the inner spiral of Specimen 5 (SFRC). The bottom plots display the projected strain profiles on each side of the specimen.

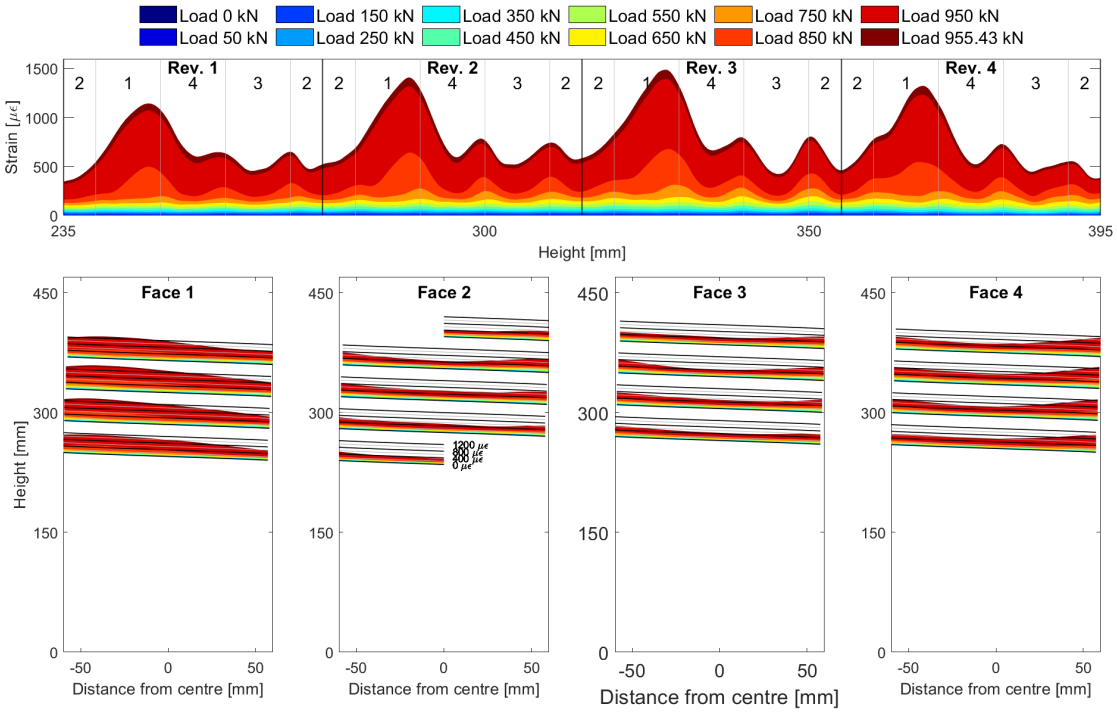

Figure E.6: Strain profiles for different load steps obtained by DOFS located at the inner spiral of Specimen 6 (SFRC). The bottom plots display the projected strain profiles on each side of the specimen.

F

DIC images

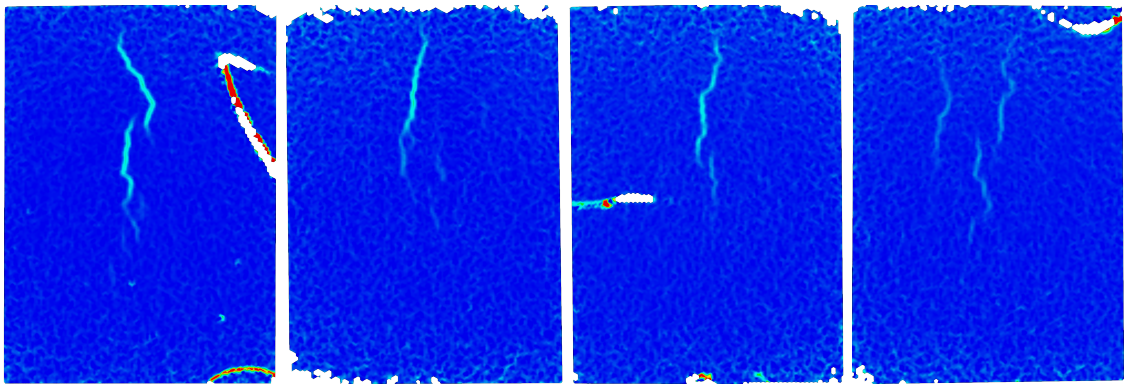

(a) Side 1 **(b)** Side 2 **(c)** Side 3 **(d)** Side 4

Figure F.1: Surface strain fields measured with DIC at 950 kN for Specimen 1 (Reference).

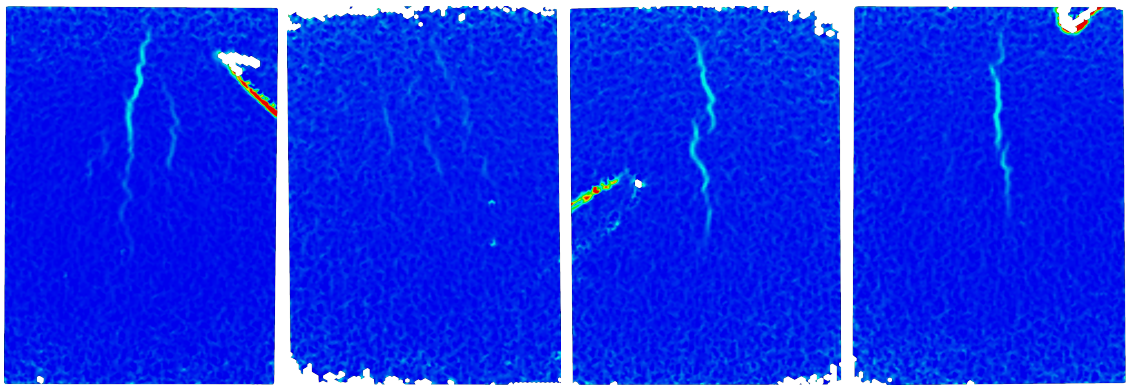

(a) Side 1 **(b)** Side 2 **(c)** Side 3 **(d)** Side 4

Figure F.2: Surface strain fields measured with DIC at 950 kN for Specimen 2 (Reference).

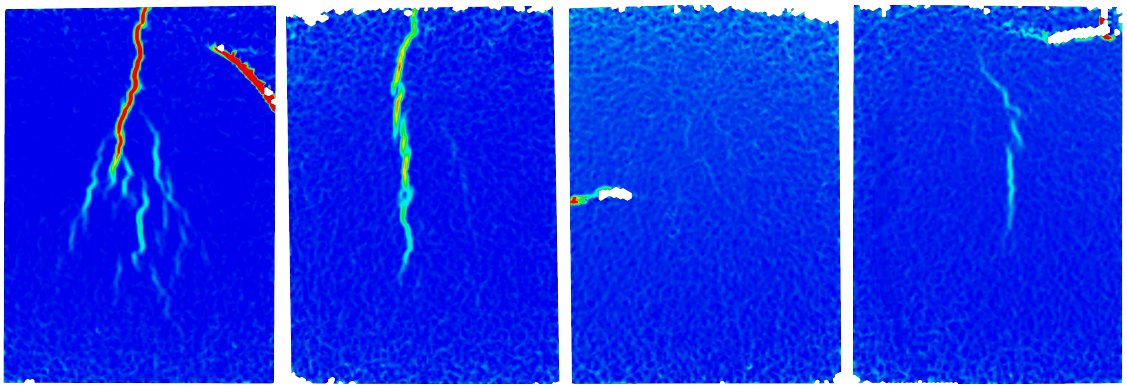

(a) Side 1 **(b)** Side 2 **(c)** Side 3 **(d)** Side 4

Figure F.3: Surface strain fields measured with DIC at 950 kN for Specimen 3 (SFRC + Helix).

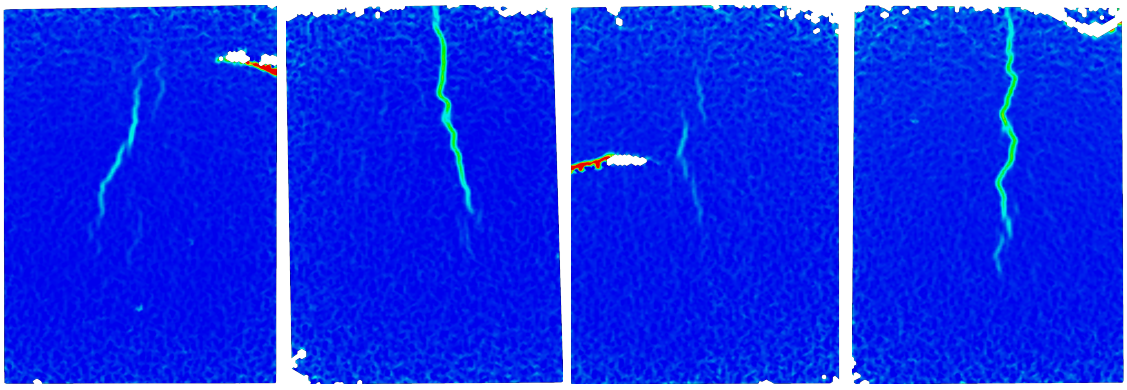

(a) Side 1 **(b)** Side 2 **(c)** Side 3 **(d)** Side 4

Figure F.4: Surface strain fields measured with DIC at 950 kN for Specimen 4 (SFRC + Helix).

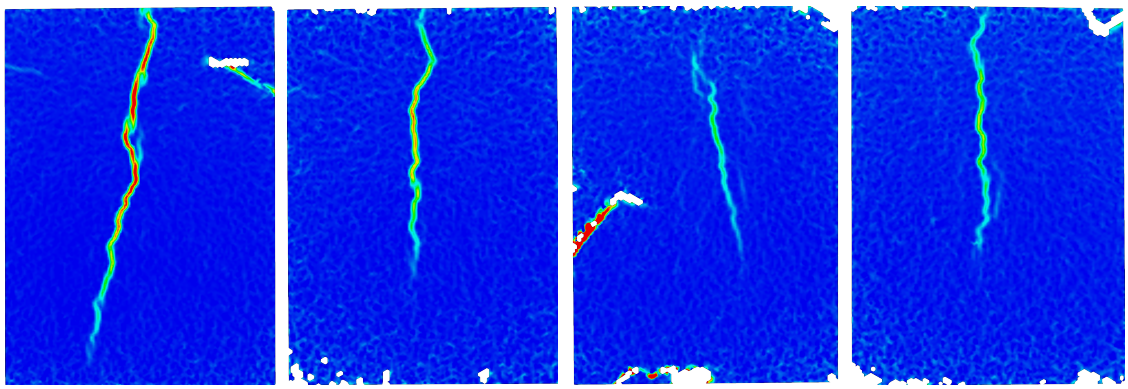

(a) Side 1 **(b)** Side 2 **(c)** Side 3 **(d)** Side 4

Figure F.5: Surface strain fields measured with DIC at 950 kN for Specimen 5 (SFRC).

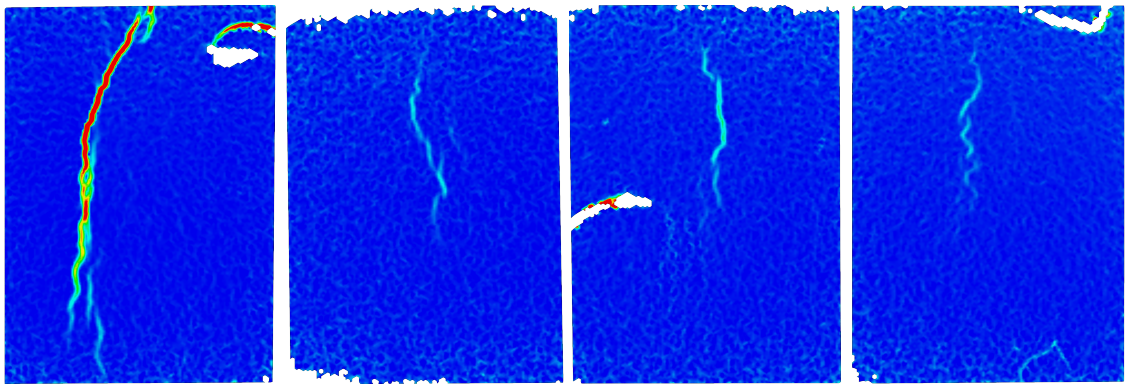

(a) Side 1 **(b)** Side 2 **(c)** Side 3 **(d)** Side 4

Figure F.6: Surface strain fields measured with DIC at 950 kN for Specimen 6 (SFRC).

G

Surface strain fields measured with DIC compared with DOFS measured strains

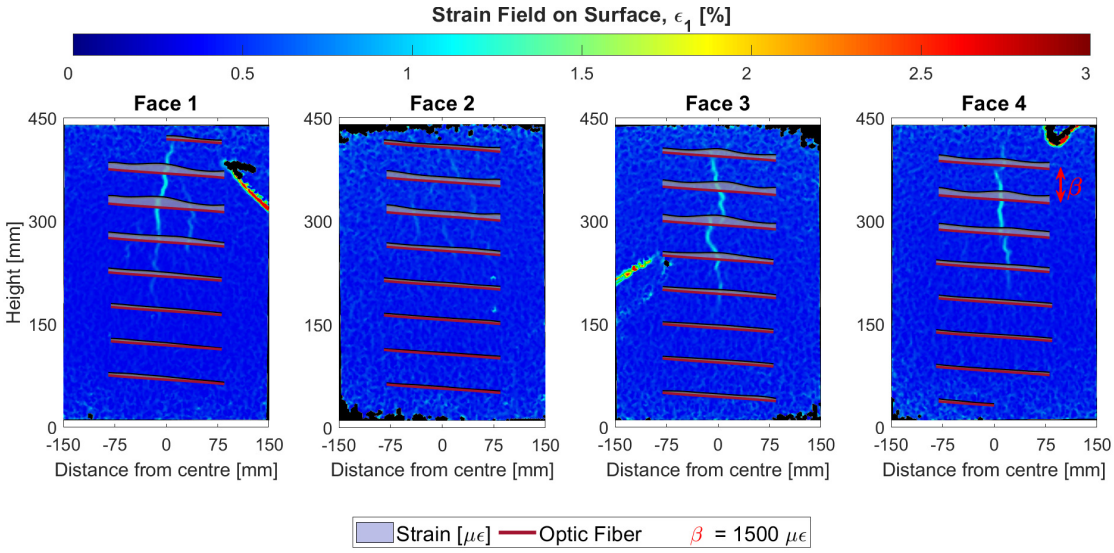

Figure G.1: Surface strain fields measured with DIC compared with DOFS measured strains at 950 kN for Specimen 2 (Reference).

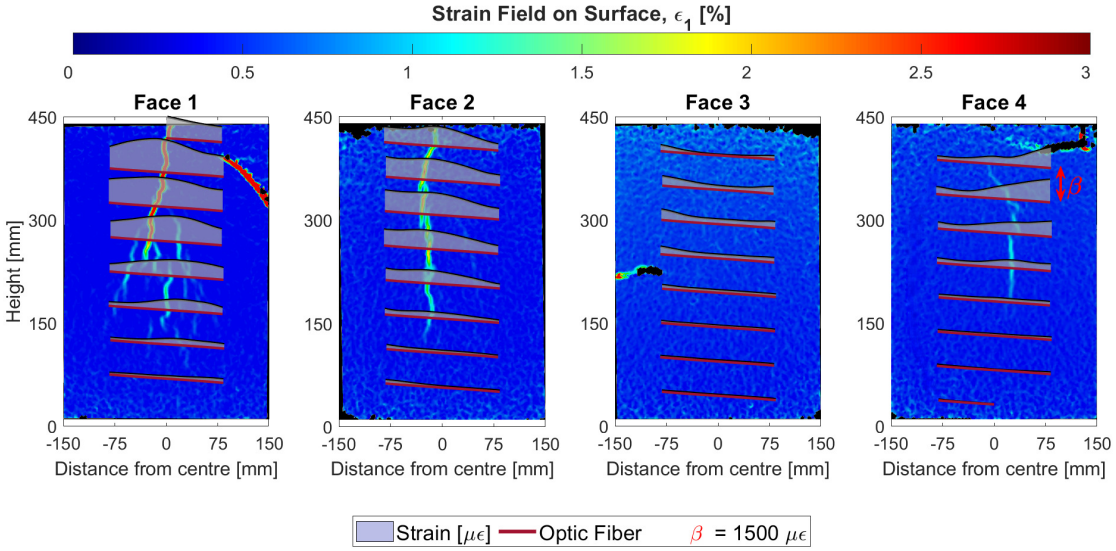

Figure G.2: Surface strain fields measured with DIC compared with DOFS measured strains at 950 kN for Specimen 3 (SFRC + Helix).

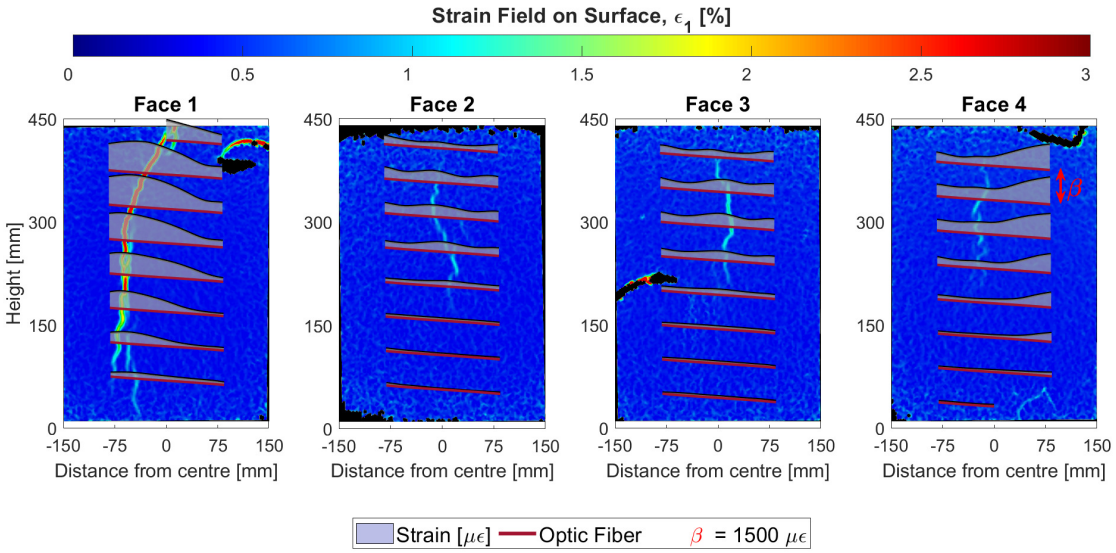

Figure G.3: Surface strain fields measured with DIC compared with DOFS measured strains at 950 kN for Specimen 6 (SFRC).

H

Crack widths

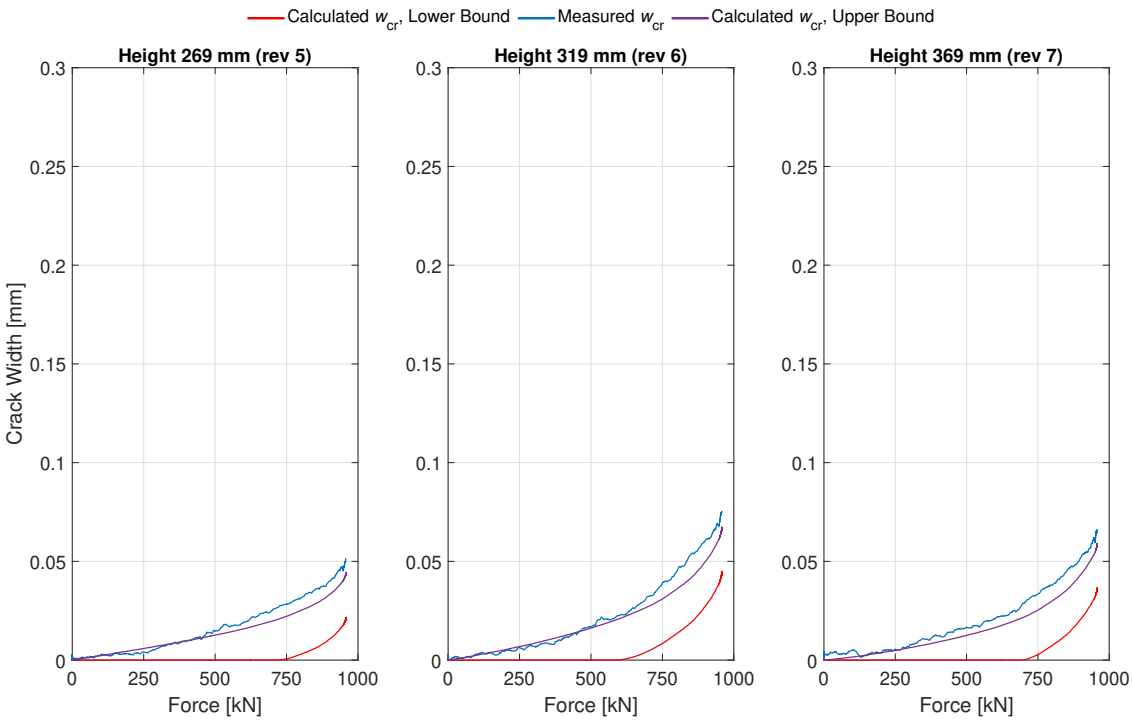

Figure H.1: Comparison of measured crack widths from DIC and calculated crack widths based on DOFS measurements calculated using Equations 5.1 and 5.2 during loading for Specimen 2 (Reference).

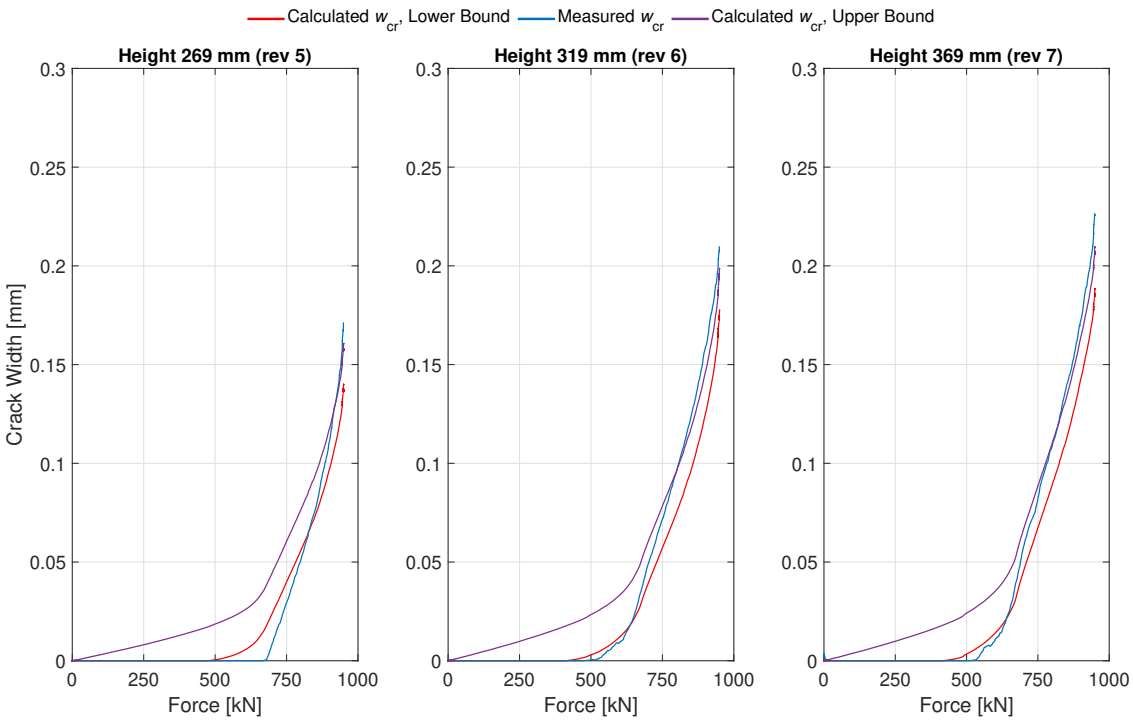

Figure H.2: Comparison of measured crack widths from DIC and calculated crack widths based on DOFS measurements calculated using Equations 5.1 and 5.2 during loading for Specimen 3 (SFRC + Helix).

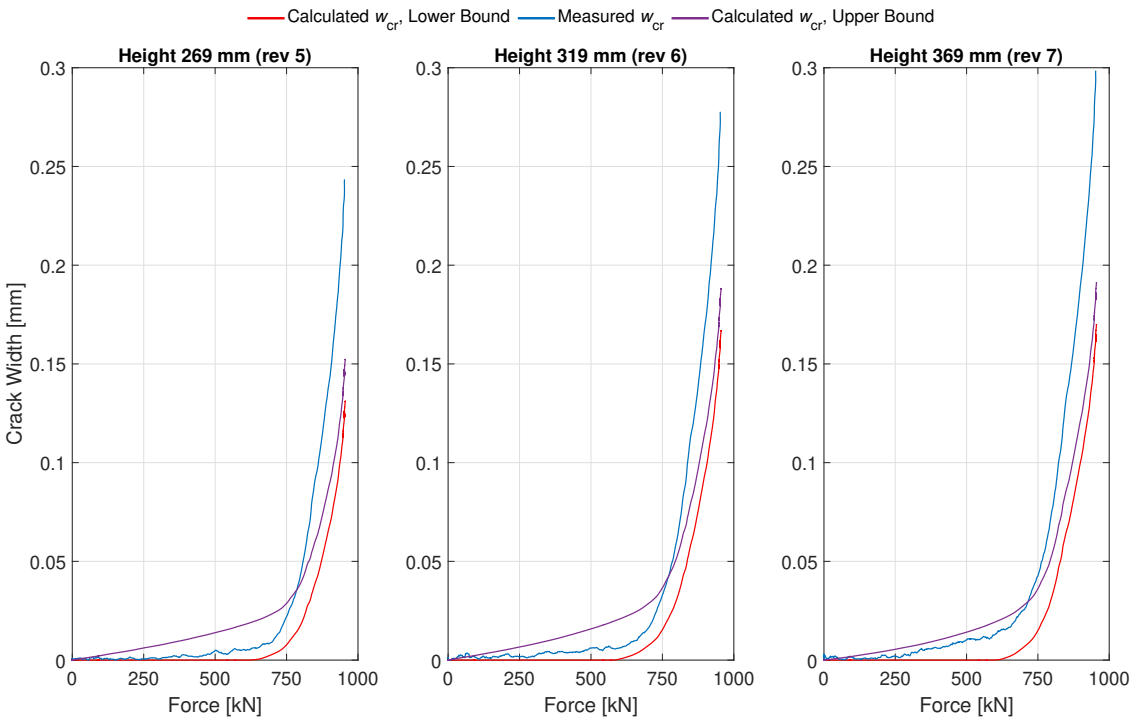

Figure H.3: Comparison of measured crack widths from DIC and calculated crack widths based on DOFS measurements calculated using Equations 5.1 and 5.2 during loading for Specimen 6 (SFRC).

I

Product sheet XM20

The appendix provides product information sourced from the European Technical Assessment dated 22/09/2015 for the XM anchor system, with the subsequent pages from the approval (European Technical Assessment, 2015).

Table 11 Maximum Allowable Stressing Force of Tendons with Ø15.7mm Strand

				Y1770-15.7		Y1860-15.7	
Anchorage	***n***	A_p **mm²**	M_p **kg/m**	F_{pk} **kN**	F_0 **kN**	F_{pk} **kN**	F_0 **kN**
XM/XMC-10	3	450	3.52	797	632	837	664
XM/XMC-20	4	600	4.69	1062	842	1116	886
XM/XMC-30	7	1050	8.20	1859	1474	1953	1550
XM/XMC-35	9	1350	10.55	2390	1895	2511	1993
XM/XMC-40	12	1800	14.06	3186	2527	3348	2657
XM/XMC-45	13	1950	15.24	3452	2738	3627	2878
XM/XMC-50	15	2250	17.58	3983	3159	4185	3321
XM/XMC-55	17	2550	19.92	4514	3580	4743	3764
XM/XMC-60	19	2850	22.27	5045	4001	5301	4207
XM/XMC-70	22	3300	25.78	5841	4633	6138	4871
XM/XMC-75	25	3750	29.30	6638	5265	6975	5535
XM/XMC-80	27	4050	31.64	7169	5686	7533	5978
XM/XMC-90	31	4650	36.33	8231	6529	8649	6863
XM/XMC-95	35	5250	41.02	9293	7371	9765	7749
XM/XMC-100	37	5550	43.36	9824	7792	10323	8192

1.2.4. CCL Stressing Jacks

The CCL ‘MG’ Stressing Jacks used for the CCL ‘XM’ and ‘XMC’ Systems have the following features:

- Automatic gripping of the wedges on the strands.
- The simultaneous stressing of all the strands of the tendon.
- Support of the Jack on the FTU, by means of a temporary Bearing Ring.
- The simultaneous hydraulic lock-off of all the wedges in the AH.
- Partial stressing of the tendons with later recovery up to the final values of the prestressing force.
- The stressing by successive loadings of the Jack when the final extension is greater than the full extension of the CCL Jack.

Other different Jacks may be used by the CCL Specialist PT Distribution/Licence Company, provided their suitability to the CCL ‘XM’ and ‘XMC’ Anchorages is approved by CCL before use.

Manuals and procedures are supplied with each CCL Stressing Jack.

Various dimensions and characteristics of CCL ‘MG’ Stressing Jacks are given in Annex 34 & 35. CCL ‘MG’ Jacks are marked on the Outer Cylinder with their Serial Numbers for identification purposes.

Different Jack innards are required for each system type.

Live End Anchorage Ø15.2/15.3/15.7mm Strand

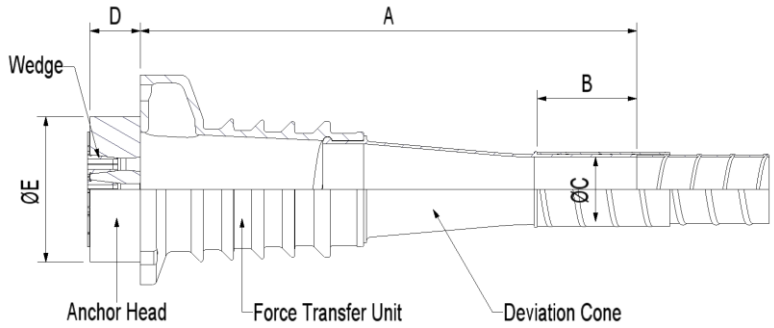

Anchorage	A	B	ØC	D	ØE
XM-10	234	70	48	45	95
XM-20	300	70	50	45	105
XM-30	362	100	64	48	130
XM-35	493	113	74	47	155
XM-40	629	113	74	54	180
XM-45	629	113	74	63	180
XM-50	693	130	84	60	195
XM-55	742	150	98	62	215
XM-60	749	150	98	76	220
XM-70	913	150	98	70	245
XM-75	1001	175	113	80	265
XM-80	1001	175	113	83	270
XM-90	1118	190	123	94	295
XM-95	1079	210	138	94	305
XM-100	1089	210	138	102	310

Bursting Reinforcement Sizes for Helices $f_{cm,0}$ on cube 46MPa (f_{yk} = 500MPa)

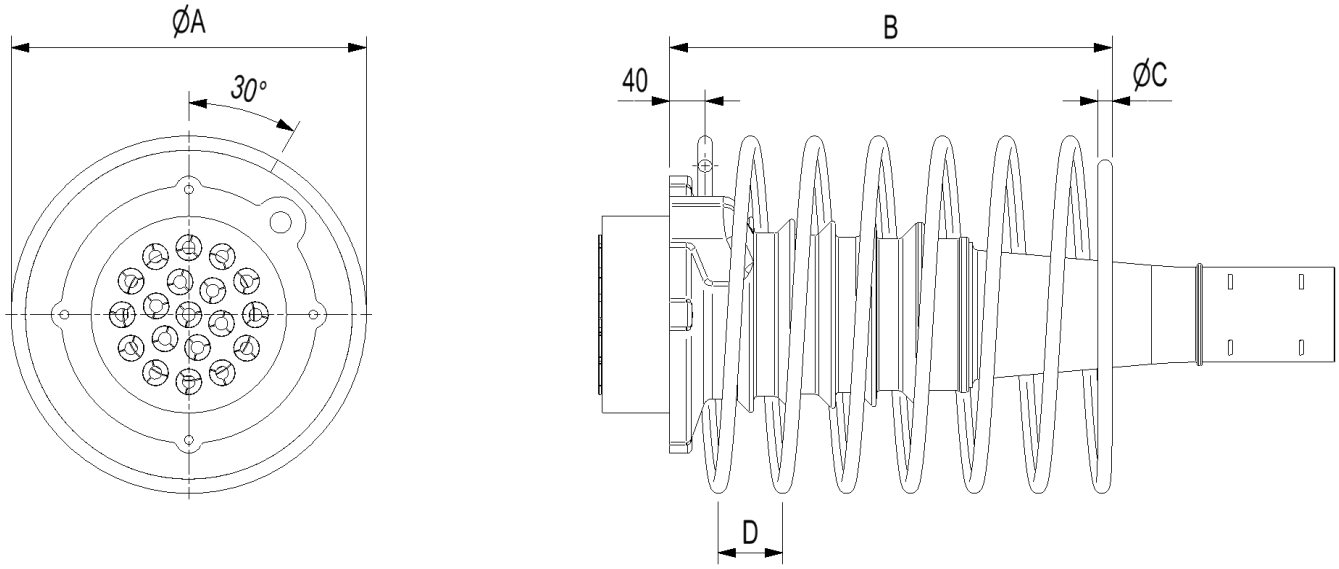

N = No. of turns in Helix

	$f_{cm,0}$ on cube				
	46MPa				
Anchorage	**ØA**	**B**	**ØC**	**D**	**N**
XM/XMC-10	160	200	8	55	3
XM/XMC-20	170	220	10	50	4
XM/XMC-30	230	260	10	40	5.5
XM/XMC-35	250	300	12	45	6
XM/XMC-40	290	320	12	45	6.5
XM/XMC-45	300	340	16	50	6
XM/XMC-50	315	360	16	50	6.5
XM/XMC-55	340	380	16	50	7
XM/XMC-60	365	400	16	60	6
XM/XMC-70	385	430	16	60	6.5
XM/XMC-75	415	460	16	60	7
XM/XMC-80	445	480	16	65	7

*f_{yk} = 500MPa (Deformed/Ribbed Rebar)

J

Dimensioning of reinforced concrete specimen

The appendix provides calculations for the dimensioning of the reinforced concrete specimen, following design codes and recommendations provided by European Committee for Standardization (2004), European Committee for Standardization (2005) and Engström (2015).

Material

Reinforcement

$f_{yk} := 500\ \boldsymbol{MPa}$

Concrete

$f_{cm} := 38\ \boldsymbol{MPa}$

$\gamma_c := 1$

$f_{ck} := f_{cm} - 8\ \boldsymbol{MPa} = 30\ \boldsymbol{MPa}$

$f_{ctm} := 0.3 \cdot \left(\frac{f_{ck}}{\boldsymbol{MPa}} \right)^{\frac{2}{3}}\ \boldsymbol{MPa} = 2.9\ \boldsymbol{MPa}$

Force

$P := 1116\ \boldsymbol{kN}$ — Characteristic tendon force for anchorage system

Geometry

$h := 450\ \boldsymbol{mm}$ — Height of concrete specimen

$b_2 := 300\ \boldsymbol{mm}$ — Width of concrete specimen

$d_1 := 140\ \boldsymbol{mm}$ — Diameter of load transfer unit

$A_1 := \pi \cdot \left(\frac{d_1}{2} \right)^2 = \left(1.5 \cdot 10^{-2} \right)\ \boldsymbol{m}^2$ — Area of load transfer unit

$b_1 := \sqrt{A_1} = 124.1\ \boldsymbol{mm}$ — Side length of load transfer unit for equivalent squared shape

Design of ties

$\phi := 10\ \boldsymbol{mm}$ Diameter of rebar

$A_{si} := \pi \cdot \left(\frac{\phi}{2}\right)^2 = 78.5\ \boldsymbol{mm^2}$

$z := \sqrt{3} \cdot \left(\frac{\sqrt{2} \cdot b_2}{4} - \frac{\sqrt{2} \cdot b_1}{4}\right) = 107.7\ \boldsymbol{mm}$

$T_{diagonal} := \frac{\frac{P}{4}}{\tan(60\ \boldsymbol{deg})} = 161.1\ \boldsymbol{kN}$

$T := \frac{T_{diagonal}}{\sqrt{2}} = 113.9\ \boldsymbol{kN}$

$n_{t.1} := \text{ceil}\left(\frac{T}{f_{yk} \cdot A_{si}}\right) = 3$ $A_{s.t.1} := n_{t.1} \cdot A_{si} = \left(2.4 \cdot 10^{-4}\right)\ \boldsymbol{m^2}$

$A_{s.1} := \frac{T}{f_{yk}} = 227.8\ \boldsymbol{mm^2}$ $\frac{A_{s.1}}{A_{s.t.1}} = 96.7\%$

Check of struts

$v_{part} := 3$ Recommended value for concentrically loaded areas

$\sigma_{Rk} := v_{part} \cdot f_{ck} = 90$ ***MPa***

Plate

$\sigma_{plate} := \frac{P}{A_1} = 72.5$ ***MPa*** $\frac{\sigma_{plate}}{\sigma_{Rk}} = 80.6\%$

Underneath plate

$C_0 := T = 113.9$ ***kN***

$$a_0 := \frac{\frac{C_0}{\sqrt{2}}}{\sigma_{Rk} \cdot \frac{b_1}{2}} = 14.4 \text{ mm}$$

$a_c := \frac{a_0}{2} = 7.2$ ***mm*** Choose 10 mm

Minimum reinforcement according to Annex J in 1992-2-2

Check is valid for Node 1

$a_j := d_1 = 140\ \textbf{mm}$

$a'_j := d_1 = 140\ \textbf{mm}$

$c_j := b_2 = 300\ \textbf{mm}$

$c'_j := b_2 = 300\ \textbf{mm}$

Controll of concrete prism

$$\begin{array}{l}\text{if } \max\left(\frac{c_j}{a_j}, \frac{c'_j}{a'_j}\right) \le 1.25 \cdot \sqrt{\frac{c_j \cdot c'_j}{a_j \cdot a'_j}} \\ \quad \text{“OK”} \\ \text{else} \\ \quad \text{“NOT OK”}\end{array} = \text{“OK”}$$

$\sigma_{pr} := \frac{P}{c_j \cdot c'_j} = 12.4\ \textbf{MPa}$ $\qquad 0.6\, f_{ck} = 18\ \textbf{MPa}$

$$\begin{array}{l}\text{if } \sigma_{pr} \le 0.6\, f_{ck} \\ \quad \text{“OK”} \\ \text{else} \\ \quad \text{“NOT OK”}\end{array} = \text{“OK”}$$

Minimum reinforcement

$l_{pr} := 1.2 \cdot \max\left(c_j, c'_j\right) = 360\ \textbf{mm}$ Length of which reinforcment should be placed within

$A_{s.j} := 0.15 \cdot \frac{P}{f_{yk}} = \left(3.3 \cdot 10^{-4}\right)\ \textbf{m}^2$ Minimum spalling reinforcement

$n_{s.j} := \text{ceil}\left(\frac{A_{s.j}}{2\ A_{si}}\right) = 3$ Number of bars in each direction

$A_{s.j.s} := 0.03 \cdot \frac{P}{f_{yk}} = \left(6.7 \cdot 10^{-5}\right)\ \textbf{m}^2$ Minimum surface reinforcement around anchor

$n_{s.j.s} := \text{ceil}\left(\frac{A_{s.j.s}}{2\ \pi \cdot \left(\frac{8\ \textbf{mm}}{2}\right)^2}\right) = 1$ Number of bars in each direction

Concrete cover and minimum spacing between bars

$\Delta c_{dev} := 10\ mm$

$c_{nom} := \phi + \Delta c_{dev} = 20\ mm$ Minimum concrete cover

$k_{1.\phi} := 1 \quad k_{2.\phi} := 5\ mm$

$d_g := 16\ mm$

$s_{min} := \max\left(k_{1.\phi} \cdot \phi, d_g + k_{2.\phi}, 20\ mm\right) = 21\ mm$ Minimum spacing between bars

Minimum edge distance for anchorage system according to ETA 07/0035

The minimum edge distance is based on required distance between multiple anchorage systems. Only one anchorage system is considered in this thesis, therefore only the concrete cover is limiting. If several post-tension systems were used the minimum edge distance would be x_1, which is assmued for this case.

$a := 220\ mm$ Prescribed value for XM-20

$x_{2.a} := 1.15 \cdot a$

$x_{2.b} := \frac{a}{1.15}$

$x_2 := \begin{bmatrix} x_{2.a} \\ x_{2.b} \end{bmatrix} = \begin{bmatrix} 253 \\ 191.3 \end{bmatrix} mm$ Spacing range of multiple anchorage systems

$x_1 := \frac{x_2}{2} + c_{nom} - 10\ mm = \begin{bmatrix} 136.5 \\ 105.7 \end{bmatrix} mm$ Minimum edge distance for anchorage system (measured from centrum of anchorage system to edge of specimen)

$\frac{b_2}{2} = 150\ mm$ Edge distance

$$\begin{array}{l} \text{if } \frac{b_2}{2} > \max\left(x_1\right) \\ \quad \text{“OK”} \\ \text{else} \\ \quad \text{“NOT OK”} \end{array} = \text{“OK”}$$

DEPARTMENT OF ARCHITECTURE AND CIVIL ENGINEERING
CHALMERS UNIVERSITY OF TECHNOLOGY
Gothenburg, Sweden
www.chalmers.se

CHALMERS
UNIVERSITY OF TECHNOLOGY